Fakultät für Maschinenwesen
Lehrstuhl für Aerodynamik und Strömungsmechanik

Large-eddy simulations of supersonic mixing with application to scramjets

Sebastian M. Eberhardt

Vollständiger Abdruck der von der Fakultät für Maschinenwesen der Technischen Universität München zur Erlangung des akademischen Grades eines

Doktor-Ingenieurs

genehmigten Dissertation.

Vorsitzender:		Univ.-Prof. Dr.-Ing. Oskar J. Haidn
Prüfer der Dissertation:	1.	Univ.-Prof. Dr.-Ing. Nikolaus A. Adams
	2.	Prof. Dr.-Ing. Stefan Hickel, Technische Universiteit Delft, Niederlande

Die Dissertation wurde am 07.12.2015 bei der Technischen Universität München eingereicht und durch die Fakultät für Maschinenwesen am 01.02.2017 angenommen.

Acknowledgements

I would like to thank my supervisor Professor Nikolaus Adams for his support, both financially and technically, over the time at his institute. I would also like to thank Professor Stefan Hickel for access to the INCA code and for the many technical discussions. From both I have learned alot during the last few years.

My PhD has been funded by the German Research Foundation DFG within the Research Training Group GRK 1092/2. I would like to thank Professor Bernard Weigand for accepting me into the reasearch group. The possibility to exchange experiences and ideas with international scramjet researchers at the annual summer schools and winter meetings was invaluable.

I am very gratefull to my collegues at the institute for flight propulsion and the institute of thermodynamics at Technische Universität München for providing important experimental data and for all the valuable and insightful discussions.

I also greatly acknowledge the computing time on the supercomputer SuperMUC provided by the Leibniz Supercomputing Centre in Garching, as well as the computing time on the HERMIT supercomputer at the High Performance Computing Center in Stuttgart.

My collegues at the institute of Aerodynamics and Fluidmechanics are greatly appreaciated for great discussions, motivational and inspirational conversations throughout my time there.

Last but not least, I would like to thank my family for their constant support and encouragement.

Abstract

In supersonic combustion-chamber flows the penetration depth of fuel injection perpendicular to the main flow direction is very small. That means, fuel injected from the walls of large combustion chambers will not penetrate into the core flow. This challenge can be solved through geometric modifications and additions to the flow duct. A common way of adding fuel to the core flow is by using strut injectors. The geometry of struts can vary and is mostly used to increase the fuel mixing rate, e.g., by generation of streamwise vortices. In this work the injection and mixing behavior of a generic strut injector is investigated using high fidelity large-eddy simulations.

Before the injector is analyzed, a generic, well documented, injection configuration is simulated for validation of the flow solver for supersonic jet flows. Besides the validation, a subset of parameters will be varied in an effort to explain common differences in simulations from this work and from literature to the experiments.

In order to perform the subsequent simulations of the strut injector, the capability of simulating multiple species is implemented into the flow solver. Additionally a graphical tool is developed for grid generation.

The remainder of the work presents results from simulations of a strut injector. The injector has two types of injections. The first type is the main injection of fuel. The fuel is substituted by carbon dioxide in the simulation and is injected perpendicular on the strut surface. The second type is a pilot injection which, in the experiment, is lit first and is used to ignite the main injection. It consists of several hydrogen and air jets which impinge on each other to create an efficient mixing field. The results obtained in this work are compared to the available results of a recent experiment.

Contents

Nomenclature

Roman symbols

A	=	cross sectional area
c	=	speed of sound
c_f	=	friction coefficient
c_p	=	specific heat capacity at const. pressure
c_v	=	specific heat capacity at const. volume
D_{nl}, n	=	species diffusion coefficient
D	=	injection hole diameter
E	=	total energy
e	=	internal energy
h	=	enthalpy
H_{12}	=	boundary-layer shape factor based on δ_1 and δ_2
I_{sp}	=	specific impulse
J	=	jet to cross-flow momentum ratio
k	=	turbulent kinetic energy
k_b	=	Boltzman constant
L	=	shock boundary-layer interaction length, domain size
L_b	=	base height of a strut injector
L_s	=	streamwise length of a strut injector
m	=	mass
$\dot{m}$	=	mass flow rate
M	=	Molar weight
Ma	=	Mach number
p	=	static pressure
q_c	=	heat diffusion through temperature gradient
q_d	=	heat diffusion through enthalpy diffusion
R	=	specific gas constant
$\Re$	=	universal gas constant
Re	=	Reynolds number
Re_δ	=	Reynolds number based on free-stream velocity and boundary-layer thickness
Re_τ	=	Reynolds number based on friction velocity and boundary-layer thickness

Re_Θ	=	Reynolds number based on free-stream velocity and momentum thickness
s	=	entropy
t	=	time
T	=	static temperature
$u \equiv u_1$	=	streamwise velocity component
$v \equiv u_2$	=	vertical velocity component
$w \equiv u_3$	=	spanwise velocity component
$x \equiv x_1$	=	streamwise coordinate
x_n	=	mole / volume fraction of species n
$y \equiv x_2$	=	vertical coordinate
y_n	=	massfraction of species n
$z \equiv x_3$	=	spanwise coordinate

Greek symbols

δ_{ij}	=	unit tensor
δ_0	=	boundary-layer thickness at a reference point
δ_1	=	boundary-layer displacement thickness
δ_2	=	boundary-layer momentum thickness
ε	=	Lennard Jones potential
η	=	payload mass ratio
γ	=	ratio of specific heats
λ	=	thermal diffusivity
μ	=	dynamic viscosity
Ω	=	collision integral
Φ	=	arbitrary transported quantity
φ	=	structural mass ratio
σ	=	characteristic molecular length scale
τ	=	shear stress
θ	=	wedge angle of the strut injector
ρ	=	density

Subscripts

0	=	total or reference state
cc	=	quantity at combustion chamber entry
CF	=	cross-flow or free-stream quantity
δ	=	at boundary-layer edge
∞	=	free-stream quantity
i, j, k	=	directional indices

jet	=	injection or jet quantity
n	=	species index
pl	=	payload
τ	=	based on wall friction
$stoich$	=	stoichiometric
H_2	=	quantity relating to Hydrogen
O_2	=	quantity relating to Oxygen
N_2	=	quantity relating to Nitrogen
CO_2	=	quantity relating to Carbon Dioxide
x, y	=	mole parts in a Hydro Carbon fluid
x, y, z	=	direction
w	=	wall quantity

Symbols

$\cdot'$	=	fluctuation of a quantity
$\hat{\cdot}$	=	quantity after a normal shockwave
$\langle\cdot\rangle$	=	time averaged quantity

Superscripts

$+$	=	quantity normalized to wall scaling

List of Figures

List of Tables

1 Introduction to scramjets

1.1 Scramjets in civil aviation

A scramjet is an airbreathing propulsion system for hypersonic flight. The concept of a scramjet is based on a ramjet with the difference that the combustion in the combustion chamber takes place at supersonic speed in a scramjet, hence supersonic combustion ramjet. Ramjets and scramjets are described in Section 1.2 in detail.

In civil aviation, the application of vehicles that are powered by airbreathing engines designed for hypersonic flight aims towards two usage scenarios. The first is intercontinental flight for transportation of payloads and passengers over large distances in a short time. The second is the transport of payloads into orbit, namely to the low earth orbit (LEO) or geo transfer orbit (GTO). In this second scenario, usage of the scramjet engine is limited to the time during which the spacecraft is still in an atmosphere that is dens enough to provide the required amount of oxygen for combustion. This restricts the use of scramjets to the lower stages of space flight.

An example of how hypersonic intercontinental flight carrying passengers may be possible is described in the LAPCAT (Long-Term Advanced Propulsion Concepts and Technologies) program by Steelant [40] run by the European Space Agency (ESA). The biggest advantage is much shorter travelling times than with subsonic flight. A flight between Los Angeles and Sydney, e.g., could last around 2.6 hours instead of 13.4 hours when considering a cruise speed of Mach 5 [40].

The economically more promising application, however, is the usage of hypersonic engines in space flight. An early concept of applying hypersonic, airbreathing engines to a two-stage-to-orbit system is the Sänger Space Transportation System, which was part of the German Hypersonics Technology Program. The ongoing demand for space access is visualized in Fig. 1.1 by the numbers of launches since the first launch of a satellite in 1957. While the total number of launches has stagnated, the composition of launch types has shifted. Mainly the number of commercial and non US and Russian governmental launches has increased since the mid 90s, while Russian military launches have strongly declined.

The maximum payload that can be transported to orbit is only a fraction of the takeoff weight of any vehicle launching from earth. A large contributor to this is the requirement for rocket engines to carry fuel and oxidizer along, in contrast to airbreathing engines

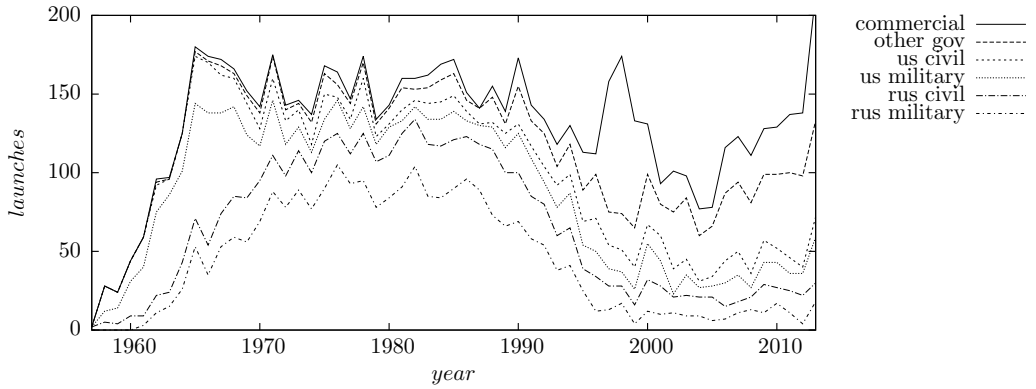

Figure 1.1: Plot of past spacecraft launches divided into commercial, military and civil types, plot based on data taken from [17].

which only carry the fuel. This hence states a potential gain when using scramjets for lower stage flight of space vehicles. No oxidizer has to be carried in this case and so the maximum payload mass can be increased. Concepts like the Sänger have the additional benefit of aerodynamic lift, which further reduces the mass of fuel and oxidizer. Besides larger payloads, aerodynamic flight capabilities reduce the risk of vehicle loss in case of a failure compared to conventional rockets. Additional advantages are horizontal take off and landing capabilities through greater reusability and the possibility of using existing starting and landing strips. The described advantages become more evident the longer the airbreathing engine can be used and the faster the vehicle flies.
The problem of the low maximum possible payload ratio can be visualized by employing the classical Ziolkovski equation

$$\frac{m}{m_0} = exp\left(-\frac{\Delta v}{I_{sp} g_0}\right) \tag{1.1}$$

for a single stage to orbit configuration. In this m is the current mass, m_0 the takeoff mass, Δv is the required velocity budget (e.g. $9.2 km/s$ for LEO), I_{sp} the specific impulse of the engine and g_0 the gravitational constant. Following [44], equation (1.1) can be rewritten with the use of specific mass ratios for the final velocity budget to determine maximum payload capabilities. Therefore the payload mass ratio

$$\eta = \frac{m_{pl}}{m_0 - m_{pl}} \tag{1.2}$$

and the structural mass ratio

$$\varphi = \frac{m_s}{m_0 - m_s} \tag{1.3}$$

are defined, with m_{pl} being the payload mass and m_s the mass of the vehicles support structure. The m/m_0 for the final orbit can be written as $(m_s + m_{pl})/m_0$. Now when

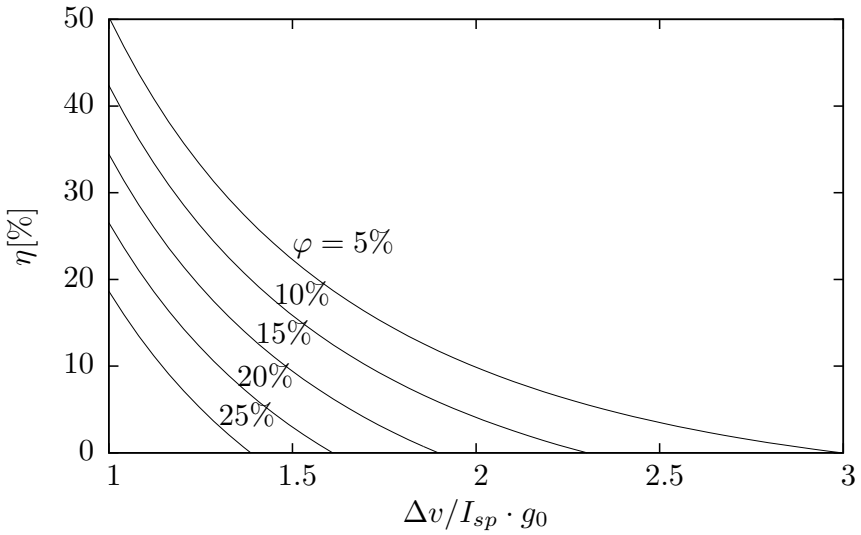

Figure 1.2: Available payload capabilities dependent on engine performance and velocity demand.

inserting the mass ratios and reforming eq. (1.1) the form

$$\eta = \frac{exp\left(-\frac{\Delta v}{I_{sp} g_0}\right) - \varphi}{1 - exp\left(-\frac{\Delta v}{I_{sp} g_0}\right)} \tag{1.4}$$

of the Ziolkovski equation is obtained, which can be plotted to show payload capabilities dependent on structure mass ratio, engine performance and velocity demand. This is shown in Fig. 1.2 for five structural mass ratios. The x-axis shows the influence of the engine performance and the velocity demand. This shows the expected behavior that only with increasing the engine performance the payload ratio can be increased for a given velocity demand. For high structural ratios even low orbit missions quickly become impossible. To demonstrate the low payload capability for a SSTO even for a LEO the following example is employed: A vehicle with a structural mass ratio of 5%, which is a very light structure and an engine that has the specific impulse of the space shuttles main engine of $I_{sp} = 409s$ (average from sea level and vacuum values, values taken from [35]) has a payload mass ratio of $\eta = 10.1\%$ if it needs to reach a LEO. For applications this restriction is lowered by staging the vehicle which gets rid of large portions of structural mass during flight.

This discussion shows that the reduction of takeoff and structural mass like oxidizer tanks has the potential of yielding large benefits to the payload capabilities of spacecraft. For this fact, scramjets are an important future technology for space vehicles.

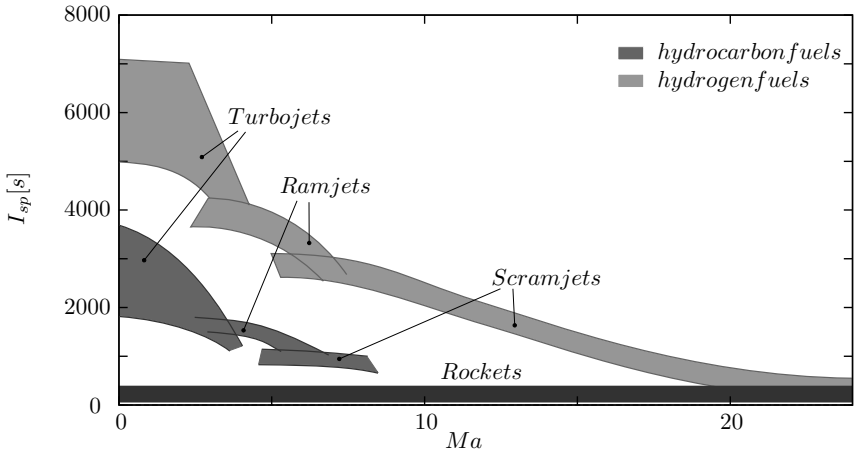

Figure 1.3: Performance over Mach number of airbreathing H_2 and C_xH_y propelled engines versus rocket engines, based on data taken from [3] and [46].

1.2 Working principle of a scramjet

In general, airbreathing propulsion concepts are defined by the maximum flight Mach number they are required to achieve. The switch from one concept to another is driven by temperature limits at high flight speeds. The regimes in which certain types of engines can operate are summarized in Fig. 1.3. From low speed to high speed the engine types turbojet, ramjet and then scramjet are used. Rockets cover all speeds, but have low efficiency and high thrust which is necessary for initial liftoff. Turbojets can reach speeds between Mach 3 and 4 before the turbine entry temperature becomes too high and turbo components are at risk of thermal failure. For higher speeds ramjets are used which do not have rotating parts and therefore do not suffer from heating of turbo components. In ramjets the incoming airflow is slowed down and compressed to subsonic speed in the combustion chamber. After the combustion, the hot gas is expanded in a thrust nozzle back to supersonic speed. This principle is pictured in Fig. 1.4. The described compression - combustion - expansion mechanism resembles the Brayton cycle which is self sustaining at high Mach number flight. Ramjets can be used for speeds up to Mach 6, before the heating through compression upstream of the combustion chamber is too large. The initially high compression temperature leads to oxygen disassociation during the combustion. This process directly lowers the available thermodynamic energy. This leads to the fact that for higher flight Mach numbers the flow through the combustion chamber has to remain supersonic to reduce the heating. This type of engine is called a supersonic combustion ramjet (scramjet), the principle of which is shown in Fig. 1.5. The air enters the engine over a sloped ramp inlet where a first compression takes place. In the isolator the fluid is further compressed by a series ob oblique shocks but remains supersonic. A second purpose of the isolator is the ability to adjust the engine to different Mach numbers. This is necessary as the shock angles and the compression changes with the flight

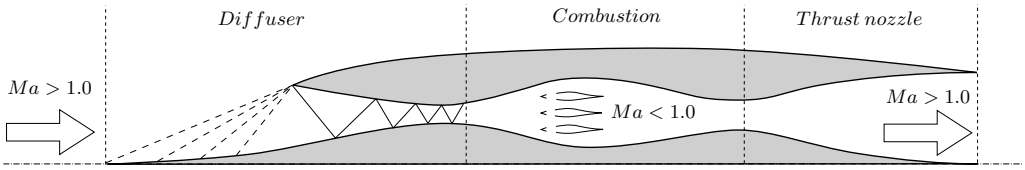

Figure 1.4: Schematic of a ramjet engine.

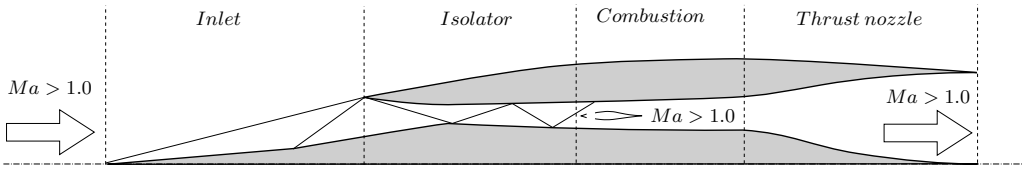

Figure 1.5: Schematic of a supersonic combustion ramjet (scramjet) engine.

Mach number. Following the supersonic combustion is a thrust nozzle, which expands and accelerates the flow to a speed above the flight Mach number to produce thrust. The thrust nozzle is often implemented as a single expansion ramp nozzle (SERN).

There are two temperature limits for ram- and scramjet engines to keep the thermodynamic cycle self sustaining. The first is the lower limit, which means that the air entering the combustion chamber has to have a minimum temperature to trigger auto-ignition of the fuel. For hydrogen this is at a static temperature of approx. $1000K$. The second limit is the already mentioned upper limit, which triggers oxygen disassociation and reduces the usable energy from the combustion. This upper limit is at approx. $1500K$. The basic concept seems rather simple as there are no moving mechanical parts, the geometry can easily be designed with gasdynamics tools and equations with heat addition. However reality is of course different from these idealized methods. There is a range of difficulties flight versions of a scramjet have to face. Some are very hard to predict or to handle. These are mainly:

- Large thermal loads on the structure of the vehicle at its leading edges, nose and in the combustion chamber.
- The transition from laminar to turbulent state in hypersonic boundary layers, which occur, e. g., on the inlet ramps, is difficult to predict.
- Separation regions where shock waves interact with the wall boundary layers.
- The fuel has to be injected with as little losses as possible and in such a way that the combustion takes place at supersonic speed.
- Mixing and combustion has to be very efficient because of short residence times inside the combustion chamber.

- Consideration of flight condition off-design through, e.g., adjustable flow duct geometry with movable parts.

Even this short list is evidence why there are only experimental flights of scramjets so far, and a lot of research has to go into assessing these issues until the technology is ready for regular use in spaceflight.

1.3 Hypersonics research in Germany and the current project GRK 1095

This work is part of the German Research Training Group (german: Graduierten Kolleg, GRK) GRK 1095. The GRK is the formal successor of previous projects and various collaborative research centers (german: Sonderforschungsbereiche, SFB) by the German Research Foundation (german: Deutsche Forschungsgemeinschaft, DFG).

In general there are three types of large scale programs working in hypersonic and scramjet research. The first category does not contain own experimental work, but is centered around purely theoretical work. Experiments done by other groups are necessary to validate theories and simulated results. The second kind includes experimental work on ground based tests. Here, supersonic wind tunnels, shock- or expansion-tubes are used to reproduce in-flight conditions as closely possible. Compressor driven supersonic wind tunnels provide continuous flow at low Mach numbers, while shock- and expansion-tubes are able to create very high Mach numbers but only for very short time spans. The third kind additionally include flight tests. There have only been few projects so far which included any flight tests. The amount of simulation work in experimental projects can vary, but some amount of simulation work is always done for designing ground experiments or test vehicles for flight.

The German programs do not include flight testing, but many projects included ground experiments and extensive simulation work. In post-war Germany, research in hypersonic technologies was started by the company Messerschmitt-Bölkow-Blohm GmbH (MBB) during the nineteen eighties with the Sänger project. The idea was to develop a two-stage-to-orbit system for satellites based on a turbo-ramjet lower stage and an upper stage with rocket engines. At an altitude of 30km stage separation should occur at a flight Mach number of 6.5. This study was divided amongst the companies MTU, Linde, MAN and MBB. Additional work was done by the German Aerospace Center DLR. In 1989 three DFG funded collaborative research centers (SFB) where added (253, 255 and 259). Most of the work in the SFBs was conducted at universities, e.g. the Rheinisch-Westfälischen Technischen Hochschule (RWTH) Aachen, Technischen Universität München (TUM) and the Universität Stuttgart. During the nineteen nineties industry recoiled from all hypersonic

research and only university projects remained. In 2004 the SFBs ended and as a successor the Research Training group (GRK) 1095 was founded in 2005, which lasted for nine years until 2014.

Unlike the SFBs the GRK focused only on scramjet technology, while in the previous projects combined cycle engines were considered. The reason for this is the higher flight Mach number of the GRK concept compared to the previous concepts. Therefore all research in the GRK was based on hypersonic technologies. The main objective of the GRK was to fully design a technology demonstrator for a single operation point using simulations and ground testing. Since the smaller size of a GRK compared to a SFB in terms of man-power, GRK 1095 only focused on the engine and did not consider a lift producing body or wings, internal system parts like tanks, pumps, guidance control, etc., or specific mission designs. The demonstrator will consist, however, of a complete engine, featuring an inlet, isolator, combustion chamber and thrust nozzle. As all parts in a scramjet engine strongly depend on each other, the GRK sub-projects are connected with each other and collaborated closely. To better define interfaces between groups of sub-projects, the GRK was divided into three main areas:

- A: Aero-thermodynamic problems
- B: Combustion
- C: Nozzle flow and system analysis

The application for which an engine is designed determines the mission profiles, and with that the required size of the overall engine and combustion chamber. Typically, unmanned small vehicles also use small combustion chambers. In these small chambers injecting fuel from the walls produces sufficient mixing of fuel and air in the core flow. In civil applications like spaceflight or intercontinental flight with passengers, larger engines and combustion chambers are required. A problem arises in large chambers, because the penetration depth of wall injectants is very low, even for high injection pressures. The GRK demonstrator uses hydrogen (H_2) as fuel which has a low mass density. This results in a lower penetration depth of wall injectors as compared to heavier fuels or liquid fuels, which penetrate deeper into the core flow. The characteristics of injection normal to the main flow direction through the combustion chamber will be discussed in the results presented in Chapter 4 of this thesis in more detail. Because of this low penetration depth, other injector designs are used in large chambers. The GRK demonstrator uses a strut injector with a lobed base geometry with supersonic H_2 injection from the injector base in streamwise direction.

The GRK demonstrator is designed for a flight Mach number of $M_\infty = 8$ and a flight altitude of $h = 30km$. With the temperature limits discussed in Sec. 1.2, Fig. 1.6 can be drawn to characterize the operational envelope of the demonstrator's inlet compression.

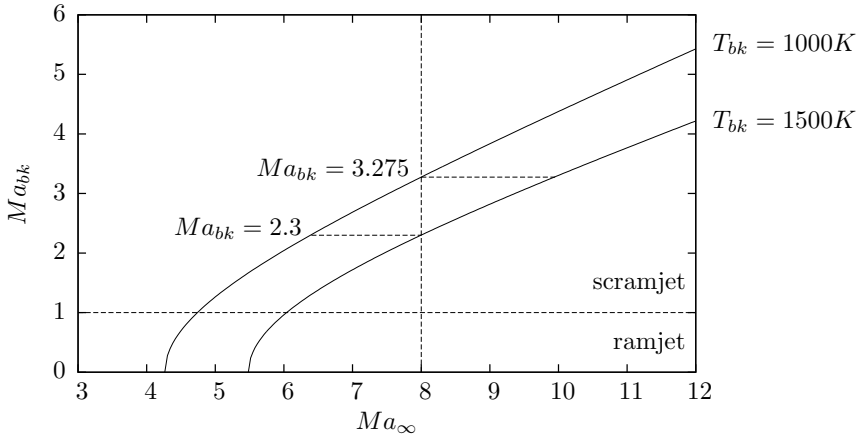

Figure 1.6: Mach number regime based on the temperature limits.

The equation plotted here results from the gasdynamic relations between Mach number and temperature:

$$Ma_{cc} = \sqrt{\frac{2}{\gamma-1} \cdot \left(\frac{T_\infty}{T_{cc}} \cdot \left(1.0 + \frac{\gamma-1}{2} \cdot Ma_\infty^2 \right) - 1 \right)}, \tag{1.5}$$

where Ma_{cc} is the combustion chamber entry Mach number, Ma_∞ the flight Mach number, T_∞ the atmospheric temperature, T_cc the combustion chamber inlet temperature and γ is the isotropic exponent for air. This directly yields a temperature and Mach number range at the combustion chamber inlet. The temperature in $30km$ altitude, $T_\infty = 234.1K$, which is needed to plot the functions for the two limiting entry temperatures T_{cc} is taken from the atmosphere model called NRLMSISE-00 [1]. The plot shows, that for the desired flight Mach number of 8, the combustion chamber entry Mach number can range from 2.3 to 3.275 to stay within the required combustion chamber entry temperature window.

The combination of theoretical or simulation based and experimental sub-projects allows for validation of theories and simulation codes by comparing these results to experiments. This allows for the simulation of operating points outside the experimental capabilities of the GRKs sub-projects.

1.4 The objective of this work

This work was conducted during the third and final funding period of the GRK 1095 as part of the combustion chamber group (B).

The objective of this work is to use high fidelity Large-eddy simulations (LES) to analyze the mixing which takes place inside a supersonic combustor. The mixing process is essential to enable supersonic combustion. Because the residence times are very short in a supersonic combustion chamber the mixing has to be efficient to allow reactions to take

place before the flow exits the combustion chamber. This work focuses on the injection of fuel vertical into a stream of air.

During the first part of the work (Chapter 4), a generic well documented case of jet injection into a supersonic cross-flow is investigated. This case consist of a single air jet injected from a wall into a supersonic cross-flow. This case is used to validate our numerical tool for supersonic mixing.

In the second part of the work (Chapter 5 and Chapter 6), this setup is extended to a flow with several species and a channel geometry with a strut injector. The setup is based on an experiment of a different GRK sub-project. It is less documented than the first case, but because of the prior validation we are confident of the results. For these simulations multispecies capabilities were implemented into the code. The numerics and single and multispecies thermodynamics are described in detail in Chapter 2.

During the course of running simulations, a tool for creating simulation meshes was required. A graphical program for creating grids was developed, implemented and extended during the entire work on the project and is presented in Chapter 3.

2 Physical and numerical modeling

2.1 Governing equations

For all simulations in this thesis the compressible Navier Stokes equations are solved. For multi species simulations the species massfraction transport is included in form of scalar transport equations. The full equations can be written as

$$\frac{\partial \rho}{\partial t} + \frac{\partial (\rho u_i)}{\partial x_i} = 0 \,, \tag{2.1}$$

$$\frac{\partial (\rho u_i)}{\partial t} + \frac{\partial \left(\rho u_i u_j\right)}{\partial x_j} + \frac{\partial p}{\partial x_i} - \frac{\partial \tau_{ij}}{\partial x_j} = 0 \,, \tag{2.2}$$

$$\frac{\partial (\rho E)}{\partial t} + \frac{\partial \left(u_i(\rho E + p)\right)}{\partial x_i} + \frac{\partial}{\partial x_i}\left(q_{c,i} + q_{d,i} - u_i \tau_{ij}\right) = 0 \,, \tag{2.3}$$

$$\frac{\partial (\rho y_n)}{\partial t} + \frac{\partial (u_i \rho y_n)}{\partial x_i} - \frac{\partial}{\partial x_i}\rho \left(D_n \frac{\partial y_n}{\partial x_i} - y_n \sum_{j=1}^{N} D_j \frac{\partial y_j}{\partial x_i} \right) = 0 \,, \tag{2.4}$$

where x_i are the Cartesian coordinates, t is the time, ρ the fluid density, u_i the velocity component in direction i and j, p the thermodynamic pressure and y_n the mass fraction of species n. The total energy E is defined as

$$E = e + \frac{1}{2} u_i^2 \tag{2.5}$$

with e representing the internal energy. The fluid is assumed to have Newtonian viscous behavior with the viscous-stress tensor

$$\tau_{ij} = \mu \left(\frac{\partial u_i}{x_j} + \frac{\partial u_j}{x_i} - \frac{2}{3} \frac{\partial u_k}{\partial x_k} \delta_{ij} \right). \tag{2.6}$$

Here μ is the dynamic viscosity and δ the unit tensor. Equations 2.1-2.4 are closed by providing expressions for the pressure p, temperature T, viscosity μ and thermal diffusivity λ. The conductive heat flux

$$q_{c,i} = -\lambda \frac{\partial T}{\partial x_i} \tag{2.7}$$

is modeled by Fourier's law for direction i, where λ is the thermal conductivity and T the temperature. An additional diffusive term appears in the multi species energy equation.

If different species diffuse into each other, they carry their energy as well as their mass. This changes the internal energy e of the mixture, and hence the term

$$q_{d,i} = -\rho \sum_{n=1}^{N} h_n \left(D_n \frac{\partial y_n}{\partial x_i} - y_n \sum_{j=1}^{N} D_j \frac{\partial y_j}{\partial x_i} \right) \tag{2.8}$$

is added to equation 2.3, with the species enthalpies $h_n = e_n + p_n/\rho_n$ described by Cook [4]. If enthalpy diffusion is neglected, large errors in the temperature field may occur.

All gases in this thesis are treated as perfect gases, with internal energy and enthalpy being

$$e_n = c_{v,n}T, h_n = c_{p,n}T. \tag{2.9}$$

The pressure is calculated from the equation of state for ideal gases

$$p = \rho RT \tag{2.10}$$

with the gas constant of the mixture.

2.2 Single species thermodynamic model

In the single species simulations jet and cross-flow fluids are modeled as perfect gas with the properties of air. The viscosity is modeled by Sutherland's law

$$\mu = \mu_{ref} \cdot \left(\frac{T}{T_{ref}} \right)^{\frac{3}{2}} \cdot \left(\frac{T_{ref} + S}{T + S} \right), \tag{2.11}$$

with S being the Sutherland's constant, T the temperature and μ the dynamic viscosity. The subscript ref marks a reference state of $T_{ref} = 195.1K$ and $\mu_{ref} = 9.95 \cdot 10^{-5} Ps \cdot s$ with a Sutherland constant of $S = 0.564475$. All quantities in the computed single spezies equations are normalized by their free-stream counter parts. The thermal conductivity is computed from a constant Prandtl number which is fixed to $Pr = 0.7$. A passive scalar with a Schmidt number of $Sc = 1.0$ is added at the jets inflow boundary condition to track the massfraction of the jet-fluid as it mixes with the cross-flow.

2.3 Multi species thermodynamic model

As for the single species simulations, jet and cross-flow fluids are modeled as perfect gases, this time with air consisting of oxygen (O_2) and nitrogen (N_2). For reproducing the experiment of Gurtner et al. [20], the jet fluid is now pure carbon dioxide (CO_2) at the nozzle inlet. In an additional experiment with a pilot flame injection, the injectant is

Hydrogen (H_2). The capabilities to simulate multispecies flows were implemented into the flow solver INCA during the course of this work.

As the flow is inert and gas properties do not change significantly in the temperature range of the flow, the mixture properties specific heat capacity c_p, gas constant R and the ratio of specific heats γ are calculated for a fixed reference temperature. The mixture quantities are only based on the local species mixture:

$$c_p = \sum_{n=1}^{N} y_n c_{p_n}, \tag{2.12}$$

$$R = \sum_{n=1}^{N} y_n R_n, \tag{2.13}$$

$$\gamma = 1 + \frac{1}{\sum_{n=1}^{N} \frac{x_n}{\gamma_n - 1}}, \tag{2.14}$$

with the specific gas constant $R_n = \Re / M_n$, molar weight M_n, and heat capacity at constant pressure c_{p_n} for the pure species $n \in \{1 \dots N\}$, with N representing the total number of species in the simulation. The local thermal conductivity coefficient λ and viscosity μ of the mixture are calculated using the simplified Wilke [47] mixing rule

$$\lambda = \frac{\sum_{n=1}^{N} (\lambda_n y_n / \sqrt{M_n})}{\sum_{n=1}^{N} (y_n / \sqrt{M_n})}, \tag{2.15}$$

$$\mu = \frac{\sum_{n=1}^{N} (\mu_n y_n / \sqrt{M_n})}{\sum_{n=1}^{N} (y_n / \sqrt{M_n})}, \tag{2.16}$$

with μ_n denoting the viscosity for species n, λ its thermal conductivity coefficient, and y_n its mass fraction.

The species viscosities μ_n are determined by

$$\mu_n = 2.6693 \cdot 10^{-6} \frac{\sqrt{M_n T}}{\Omega_{\eta,n} \sigma_n^2}, \tag{2.17}$$

where $\Omega_{\mu,n}$ is the collision integral, σ_n a characteristic molecular length and T the mixture temperature. The collision integral can be derived from kinetic theory of dilute gases. As this leads to a very complex expression, it is common practice to use an empirical approximation, see Williams [48]. For the simulations presented here the approximation proposed by Neufeld [24] is employed

$$\Omega_{\eta,n} = a \cdot (T_n^*)^b + c \cdot \exp(d \cdot T_n^*) + e \cdot \exp(f \cdot T_n^*) \,, \tag{2.18}$$

Table 2.1: Constants for collision integral $\Omega_{\eta,n}$ computation in Eq. (2.18) from Neufeld [24].

a	b	c	d	e	f
1.16145	−0.14874	0.52487	−0.7732	2.16178	−2.43787

Table 2.2: Constants for collision integral $\Omega_{D,nl}$ computation in Eq. (2.25) from Neufeld [24].

a	b	c	d	e	f	g	h
1.06035	−0.1561	0.193	−0.47635	1.03587	−1.52996	1.76474	−3.89411

Table 2.3: Molecular constants for diffusion an viscosity relations listed by Poling [29].

property	oxygen	nitrogen	carbon dioxide
$(\varepsilon/k_b)_n$	106.7	71.4	195.2
$\sigma_n[\AA]$	3.467	3.798	3.941
$M_n[g/mol]$	31.999	28.014	44.01

where the parameter

$$T_n^* = \frac{k_b T}{\varepsilon_n} \tag{2.19}$$

is calculated from the Lennard-Jones potential ε_n, the Boltzmann constant k_b and the static temperature T. The constants a through f are given in Table 2.1.

The molecular species diffusion is approximated by a diffusion coefficient for the diffusion of a single species into a mixture of all other species, c.f. [29], which leads to the diffusion coefficient

$$D_n = (1 - x_n) \left(\sum_{l=1}^{N} \frac{x_n}{D_{nl}} \right)^{-1} \quad n \neq l, \tag{2.20}$$

by Blanc's law [32] using the molefractions $x_n = y_n(M/M_n)$ of all species and the binary diffusion coefficients

$$D_{nl} = \frac{0.0266 T^{1.5}}{p\sqrt{M_{nl}}\sigma_{nl}^2 \Omega_{D,n}}. \tag{2.21}$$

between all possible combinations of species n and l. The binary molar mass M_{nl}, the characteristic length σ_{nl} and the binary Lennard Jones potential ε_{nl} are computed as follows:

$$M_{nl} = \frac{2}{1/M_n + 1/M_l}, \tag{2.22}$$

$$\sigma_{nl} = 0.5\,(\sigma_n + \sigma_l)\,, \tag{2.23}$$

$$\varepsilon_{nl} = \sqrt{\varepsilon_n \varepsilon_l}. \tag{2.24}$$

The collision integral for diffusion is modeled as

$$\Omega_{D,nl} = \frac{a}{(T_{nl}^*)^b} + \frac{c}{\exp(dT_{nl}^*)} + \frac{e}{\exp(fT_{nl}^*)} + \frac{g}{\exp(hT_{nl}^*)}, \tag{2.25}$$

with the parameter values listed in Table 2.2 and

$$T_{nl}^* = \frac{k_b T}{\varepsilon_{nl}} \,. \tag{2.26}$$

Molecular properties for the three species used in this study are taken from [29] and are summarized in Table 2.3.

2.4 Large-eddy simulation

With the ongoing increase of computation power, large-eddy simulation (LES) is becoming an increasingly popular tool for the prediction of time-accurate unsteady flows. The Kolmogorov scale is not resolved such as in direct numerical simulations (DNS), which in turn allows for computation of high-Reynolds number flows. The amount of modeling is lower, however, than in statistical approaches like the Reynolds averaged Navier Stokes (RANS) equations. This leaves LES as a compromise for numerical simulations in terms of both computational cost and accuracy.

The large energy-containing and unsteady structures are resolved in LES. For many engineering purposes this is adequate, as the large scales dominate body-forces on structures, etc., as opposed to small scale, high-frequency content. The grid resolution truncates the exact solution when length scales in the flow become smaller than the grids cell sizes. These unresolved scales and the corresponding dissipation of kinetic energy which takes place at these scales hence have to be modeled by a subgrid-scale (SGS) turbulence model.

The truncation of scales from the solution by the grid in general resembles a spatial filtering operation as one special case out of many possible ways of filtering. Usually, only spatial filtering is applied in LES, whereas timescales are resolved by sufficiently small numerical time-steps. A generic filtering operation of the form

$$\bar{\Phi}(x,t) = G * \Phi = \int G(x-x')\Phi(x',t)dx' \tag{2.27}$$

was suggested by Leonard [18] for the analysis of the LES equations. In this, G is a homogeneous normalized filter kernel and Φ a generic transported quantity. The overbar denotes a spatially resolved-scale quantity. The unresolved scales, subscribed with SGS

since the grid serves as an example filter in this case, are obtained from

$$\Phi_{SGS}(x,t) = \Phi(x,t) - \bar{\Phi}(x,t). \tag{2.28}$$

Here common model closures come into place. Applying this to the set of equations to be solved for a simulation Eqs. 2.1-2.4 one obtains the filtered Navier Stokes equations.

2.5 Numerical model

For time-integration the explicit 3rd order accurate Runge-Kutta scheme of Gottlieb and Shu [9] and a finite-volume spatial discretization are used. The SGS model is provided by the Adaptive Local Deconvolution Method (ALDM), see Hickel et al. [13, 12], which follows an implicit LES (ILES) approach. The basic idea of ILES is to merge turbulence modeling and numerical discretization of the conservation equations. ALDM is a nonlinear finite volume method and incorporates free parameters that are used to control the implicit SGS model. A physically motivated turbulence model that is consistent with turbulence theory is obtained through parameter calibration, see Hickel et al. [13, 12] for details. ALDM is implemented for Cartesian collocated grids and is used to discretize the convective terms of the Navier-Stokes equations. The diffusive terms are discretized by 2^{nd} order central differences.

A fully conservative immersed boundary technique, based on a cutcell approach described by Meyer et al. [22, 23] and extended by Örley et al. [25], is employed to represent the circular geometry of the jet injection nozzle on the Cartesian grid.

All LES in this study were performed using our in-house code INCA, which is written in Fortran 2003 language. It uses a classical block-structured grid topology for parallelization. Three ghost-layers need to be exchanged as INCA uses discretization schemes that operate on six-point stencils. For blocks which are not part of the same process non-blocking communication according to the MPI-2.2 standard is employed, otherwise values are copied directly.

2.6 Validation of multi species implementation

As a test case for assuring the correct implementation of the multi species thermodynamics and functionalities in INCA, the interaction of a shockwave with a material interface has been chosen. This scenario involves multiple species in a highly compressible flow with shock waves and is possible to occur in supersonic combustion as stated by Yang et al. [49]. These properties make it a feasible choice for validating the simulation code's functionality for scramjet relevant simulations. The Richtmyer-Meshkov Instability (RMI) that occurs at the material interface was first theoretically described by Richt-

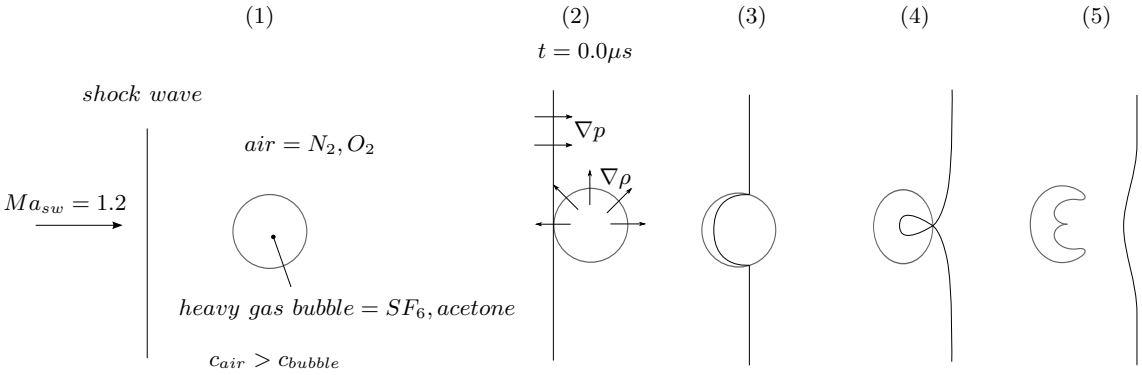

Figure 2.1: Principle of a Richtmyer-Meshkov Instability flow detailed by a shock passing through a two-dimensional heavy gas bubble.

myer [34] and later qualitatively confirmed with experiments by Meshkov [21]. It occurs when a shock wave passes by an interface between two fluids with different properties, most important density. Due to the misalignment of the density gradient and pressure gradient vectors baroclinic generation of vorticity is triggered. This vorticity is the driving force for the primary instability. Later secondary instabilities develop on the stretched interface.

For the RMI in this work a planar circular bubble of heavy gas in an air environment which is accelerated by a shock wave is chosen. The principle of this unsteady flow is pictured as a time series in Fig. 2.1. Panel (1) displays the initial condition with a circular, two-dimensional bubble of heavy gas and a shock wave traveling towards it. Step (2) shows the instance in time when the shock wave hits the bubble. The direction of the density gradient at the bubble interface and the pressure gradient across the shock are only aligned at two points on the bubble surface, namely tip and tail of the bubble. At the remaining interface baroclinic vortex production takes place due to the misalignment of the gradients. The speed of sound is lower in the heavy gas than it is in the surrounding gas, therefore the shock wave moves slower inside the bubble as pictured in (3). This results in a shock focusing on the downstream side of the bubble in (4). Finally the shock wave moves past the bubble and the bubble continues its roll up (5). This motion is only slowed by friction through viscosity in the gases.

The specific example used here is based on an experiment performed by Tomkins et al. [41] and consists of a heavy gas quasi two-dimensional bubble made up of SF_6 and acetone as an optical tracer. The bubble is placed in an air surrounding. The diameter of the bubble is $D = 6mm$ and the shock has a speed of $Ma_{sw} = 1.2$. The computational grid employed for the simulations is two dimensional and has a uniform distribution of cells in $x-$ and $y-$directions. The resolution amounts to 240 cells across the initial bubble diameter. Time measuring begins at the instance when the shock hits the bubble. The initial SF_6 distribution inside the bubble is calculated by a functional fitted to the experimental distribution.

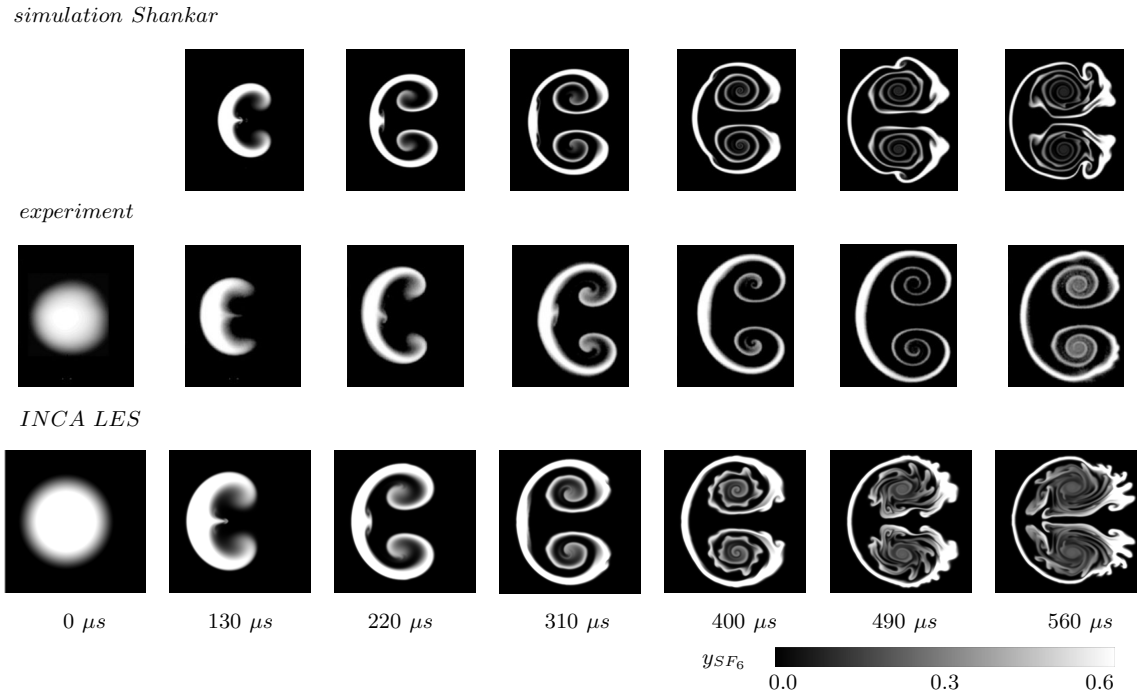

Figure 2.2: Comparison of the SF_6 heavy gas massfraction in the simulation by Shankar et al. [38] (top row), experiment by Tomkins et al. [41] (middle row) and INCA LES (bottom row) at selected times.

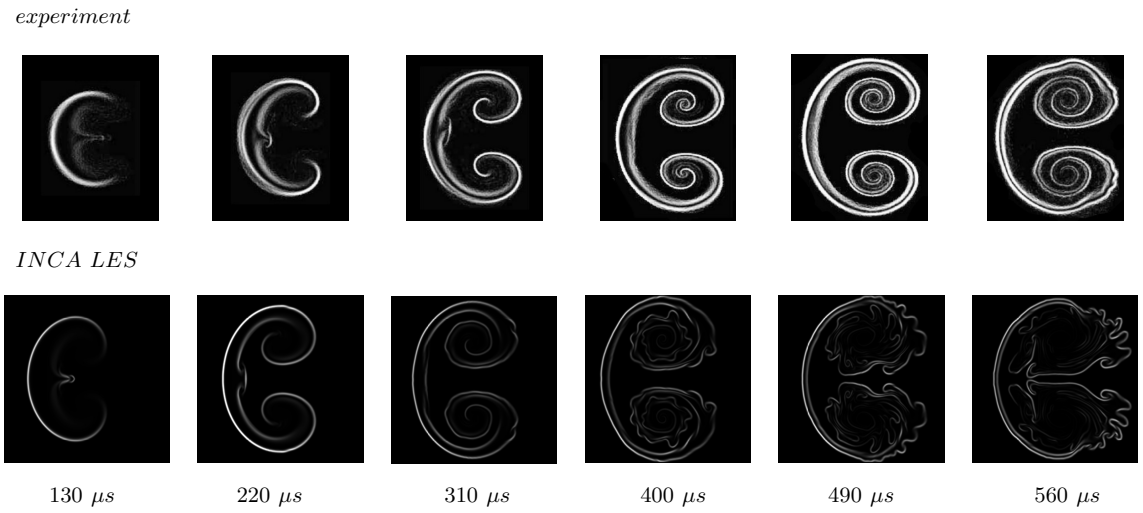

Figure 2.3: Comparison of the mixing rate between heavy gas and air in the experiment by Tomkins et al. [41] (top row) and INCA LES (bottom row) at selected times.

First, is an analysis of the SF_6 massfraction in the bubble as it develops after the passing of the shock wave. A time series at discrete times taken from Tomkins' et al. experiment [41] is plotted in Fig. 2.2 alongside two simulated sets of data, one taken from Shankar et al. [38], the other one shows simulation results computed with INCA. At time $0\mu s$ the initial circular bubble is pictured, in the remaining plots the shock has completely passed through the bubble and the roll up is visible. The simulations show a faster roll up rate and earlier development of secondary instabilities. This behavior however has been

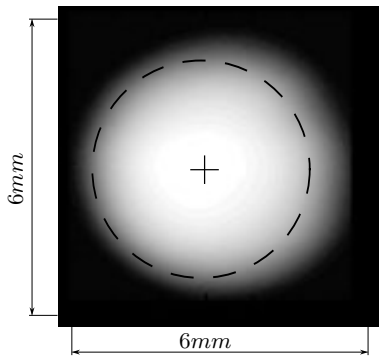

Figure 2.4: Detail of the initial ($t = 0\mu s$) conditions in the experiment displaying its non-circularity (the circle's center is marked by a cross at the concentration maximum of the heavy gas).

observed in other numerical studies as well, e.g., by Shankar et al. [38] and Tritschler et al. [42].

A second quantity important to the mixing of species is the mixing rate. Figure 2.3 shows a qualitative comparison of the mixing rate between the experiment [41] (top row) and the INCA LES (bottom row). Due to unclear normalization of the experimental data, the color values in the figure can not be compared directly. However the zones of maximum mixing rate on the downstream side of the bubble's "bridge", and the reduced mixing rate in the vortex cores and the upstream side of the bubble's "bridge" are clearly identified. The thickness of the mixing zones is smaller in the simulation. This may be due to initialization differences in the massfraction distributions. The experiment has imperfections in the initialization; the bubble is not completely circular, the concentration maximum is not at the exact center. Figure 2.4 shows the $t = 0\mu s$ snapshot of the experiment with a circle and a cross added at the concentration contour maximum. This shows the non-circularity. A study by Tritschler et al. [42] revealed that the degree of excentricity at initialization affects the time dependent development of the bubble. A second influence was investigated by Shankar et al. [38], who varied the amount of additional acetone in the SF_6. It was shown that both parameters can slow down the roll up of the bubble. Since accurate experimental investigation of the RMI is still challenging, but the different simulation results presented here show similar trends, the newly implemented features in INCA can be considered to work correctly.

3 Mesh generation for INCA

3.1 Automatic mesh generation by INCA

As mentioned in Section 2.5, INCA is implemented to work on Cartesian grids with hanging nodes refinement capabilities at block interfaces. This makes the implementation of automated refinement algorithms very convenient. Because of this, INCA provides a tool which automatically generates and refines grids, called automatic mesh refinement (AMR). This procedure starts out with a very coarse initial grid, consisting only of a few blocks, and subsequently increases the resolution. Simultaneously large blocks are split to keep the cell count of all blocks as evenly distributed as possible. Numerous refinement criteria are available, e.g., refinement to a certain minimum cell size near walls, or refinement of user specified zones. While this automation is convenient and works well for very large and complicated grids, it has drawbacks, which make it non optimal for small and medium sized grids. First, the grid generation process can be time consuming, as some parts of the process can not be done in parallel. Additionally, a large amount of memory is required on a single computer even for small grids. This is due to the operation on the solution data to be able to do refinements during runtime. During simulations the memory demand is distributed among compute nodes on a super computer. This is not possible during AMR operation when using it for initial grid generation. Additionally the user has only limited control over the final shape of the grid and only homogeneous cell distribution is possible.

For these reasons an additional tool has been developed during the work of this thesis.

3.2 INCA-BLOXX

The new tool is called INCA-BLOXX and gives the user full control over the blocking by providing a classical graphical user interface (GUI) for manual grid generation. Its core features include the import of existing INCA grids, which may be manually generated or AMR generated, the definition of data collection probes and geometry files for the immersed boundary, the modification of such and re-saving of the new data sets. This enables the program to check and fine-tune complex, large AMR generated grids.

Furthermore, currently supported features provide the following operations:

- Add / delete / modify / split single or multiple blocks simultaneously.
- Display of grid statistics: total block and cell counts, minimum and maximum cell sizes in a block, etc.
- Display a list with sorting functionality showing all blocks with their cell count.
- Functions to simultaneously modify the entire grid: Split / mirror the grid at a specified location, double / halve the cells in all blocks in a certain direction.
- Support of all meshing laws currently implemented in INCA.
- Several display options for easier editing, e.g. show / hide entire blocks, cell lines, block lines, STL solid / wireframe, cutplanes, etc.
- Color coded display of boundary conditions.
- Generate simple STL geometries to be used as immersed boundaries.
- Place / delete / modify data collection point probes and planes.
- Custom built history function for user actions with undo / redo capabilities and a user specified number of remembered actions[1]

A sample of the INCA-BLOXX GUI is shown in Fig. 3.1. In the figure example files for a grid with probes and geometry (that are included with the program) are loaded and displayed. On the left of the screen, below the menu- and tool-bars, a table displays the properties of the selected block(s). At the bottom left is a table of all blocks, which can be resorted by various criteria and used to (de-)select blocks.

3.3 INCA-BLOXX selected implementation details

The program is entirely written in C++ with multi-platform support in mind. For this reason the Qt libraries [31] are used for the graphical part of the software. Qt also provides wrappers for the OpenGL [10] environment to create an OpenGL context, which, when written natively, differs greatly between platforms. This make INCA-BLOXX compatible with Linux, Mac-OS and Windows. To further enhance compatibility, especially to notebooks with integrated graphics chips, OpenGL version 1.0 and 2.0 are employed. Starting with OpenGL 3.0 versions of OpenGL are no longer backwards compatible because of new features required from the hardware to run OpenGL 3.0. INCA-BLOXX compiles with all versions of Qt starting with 4.8.x up to current 5.3.x releases. Version control of the source code is done by a Git [39] repository.

[1] The number specified by the user is not absolutely accurate, see Section 3.3 for an explanation.

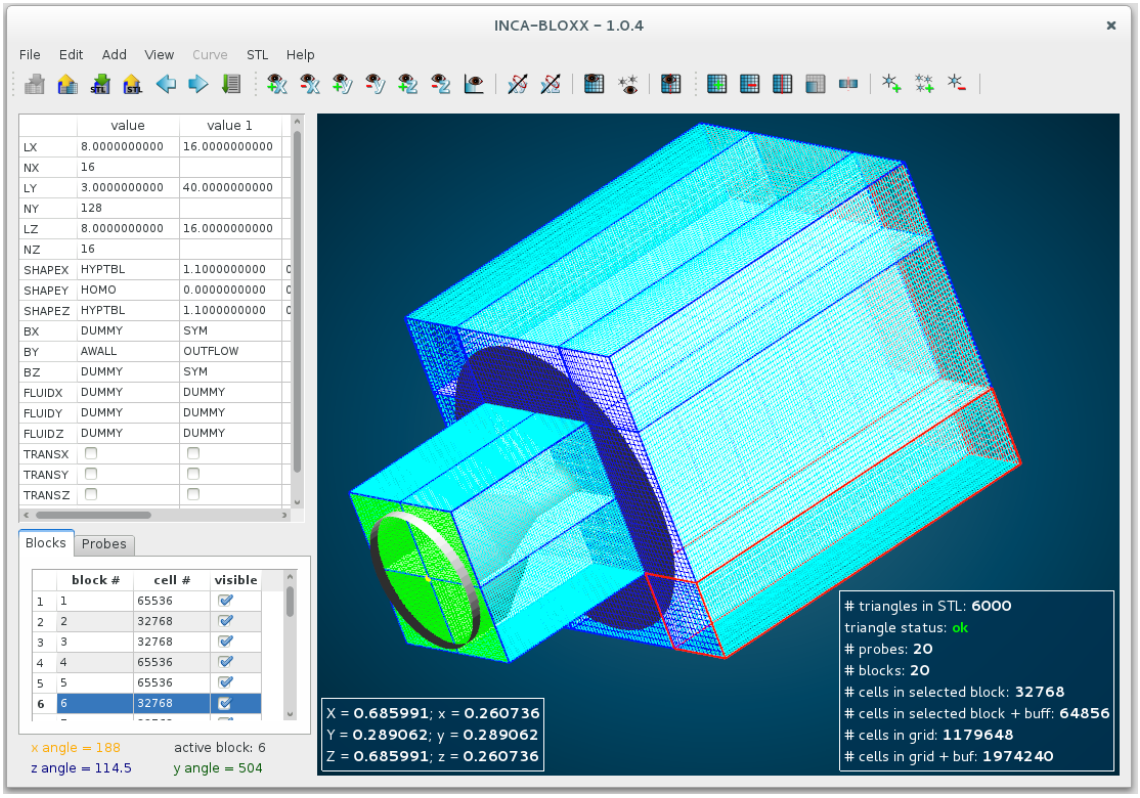

Figure 3.1: INCA-BLOXX with the loaded example grid, probes and geometry files.

Versioning: At the time of this writing INCA-BLOXX is at version number 1.1.1. The switch of the first digit from 0 to 1 marks the milestone where all features required for this thesis were included and without known severe bugs. The middle digit marks new large features, the 1 here originates from the addition of data collection planes. The last digit marks small added features and bugfixes.

Layered program architecture: The over all structure of INCA-BLOXX is built in two layers which separate different parts of the program from each other. Figure 3.2 gives an overview of the layers in INCA-BLOXX. The layers are indicated by colored boxes on the left and detailed by grey boxes on the right, which also contain connections that show directed data flow through the individual parts of the program. The top layer contains the display and user input. In a program with a graphical user interface, display and input are naturally combined and can not be separated from each other as the user always interacts with the graphical interface. This layer contains all input forms, tables and the three dimensional viewing area. No operations that directly modify the data are permitted here. The second layer is the data handling layer. This layer consists of three parts: file handling, data storage and manipulation, and the history. The file handling is where data is either read from or written to files. The data classes either provide or receive data, and contain in their instance objects all information needed for the operation of the program. This means that all functions that modify the data in any way are implemented inside the data classes. The data classes also contain the largest part of the history function. Each

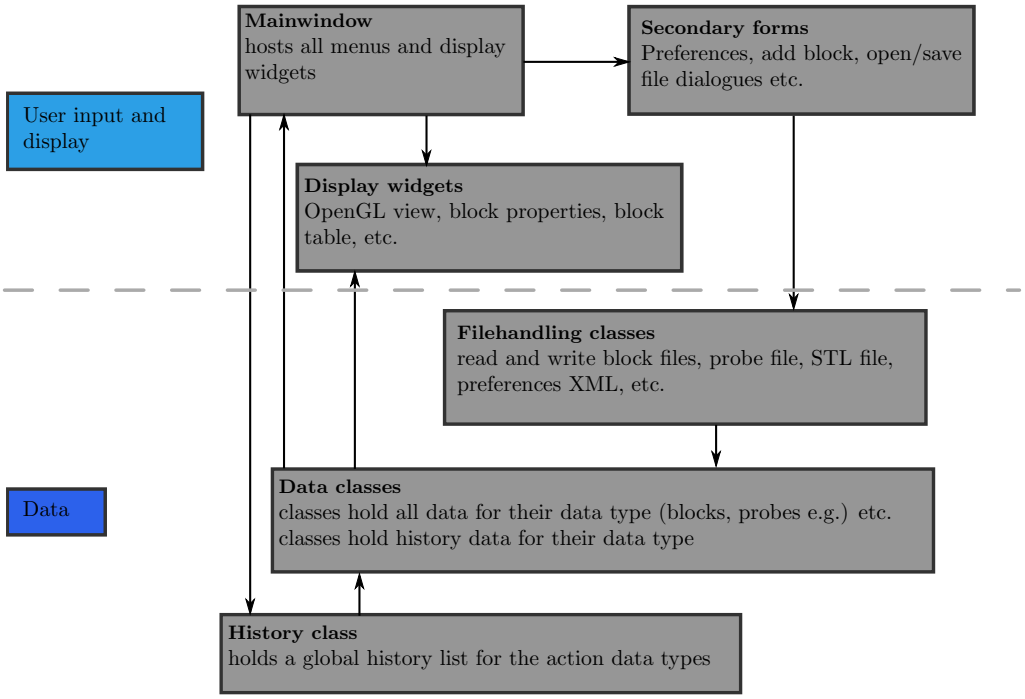

Figure 3.2: Overview of the main classes, their relations and organization in layers in the INCA-BLOXX implementation.

data class contains the history of their data type. For example, the blocks data class stores all previous steps for the blocks. The probes class does the same for probes and so on. The ability to reconstruct the correct order of actions across all data types, a timeline class exists. It is small and consists of a list of all actions, containing only the type of the last action. As a result, the program is always aware of the corresponding data class that has to reverse or reapply an action.

History function: The history lists of data classes distinguish two types of elements: Complex and simple ones. The simple entries only save the old and new state of a single data object (e.g. a single block) after an action. The complex elements save the entire list of data objects (e.g. all blocks) after actions that involve more than a single data object. The list is implemented with a last in first out approach with respect to the complex elements in a way, that the list will not grow larger as soon as a certain maximum number of complex elements is stored in the list. From the point on where the maximum length is reached, every time a new complex element is added, the oldest complex and all simple elements between the deleted complex and the second oldest complex element are deleted. This is done because the data in complex elements is used to display the data in the three dimensional view and all simple element changes are applied to that complex elements data. The maximum number of complex elements to be saved is user adjustable. To know which data type holds the next action when undoing a step, an additional list is saved, which keeps an element for actions of all data types but only saves the data type. This additional list hence acts as a lookup list to identify the data class, which has to undo

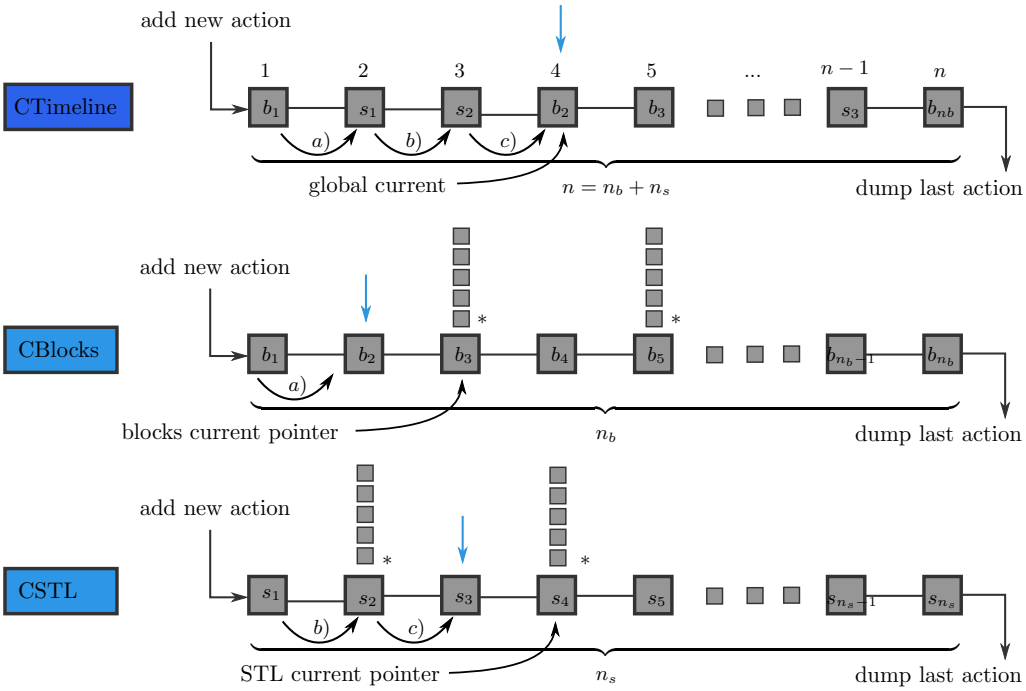

Figure 3.3: Principle of the implementation of the history function, using the block and STL classes as examples.

a step. Figure 3.3 pictures the overall timeline list (top) together with two exemplary data type lists (here blocks and stl). The elements are marked by $b_1, b_2, \ldots$ for blocks and $s_1, s_2, \ldots$ for stl which count the number of actions. The timeline contains both actions, whereas the data lists only keep their own. Elements marked by $*$ are complex elements, the boxes above them indicating the complete saved data. The current pointers always point to the newest complex element for displaying and modifying purposes. The arrows marked by $a), b)$ and $c)$ indicate undo steps to show which undo step applies to which data list. The blue arrows mark the current element in all lists.

All of the dynamic data lists described previously have to make sure they properly manage memory. To achieve this all simple elements have to be deleted between complex elements if a complex element is deleted. Additionally a dead end in the lists is created after undoing some steps and than adding a completely new action. Here the dead end has to be properly cleaned, since otherwise a memory leak is present.

4 Air jet in supersonic crossflow (JISC)

4.1 Case description JISC study

In a scramjet combustor, efficient and fast mixing of injected fuel with the surrounding airflow is essential to enable supersonic combustion because of the very short residence time of the reactants in the combustion chamber. The fuel is usually in its gas phase, since liquid injection would prohibitively increase the ignition delay time. Even for fast reacting fuels like hydrogen, the ignition delay time typically is of the same order of magnitude as the flow through time. A state of the art and widely studied (see e.g. Watanabe et al. [45], Kim et al. [15], Rana et al.[33]) way of injecting fuel into a scramjet combustor is a sonic jet of gaseous fuel that is injected perpendicularly into the supersonic main stream.

A schematic of the jet in supersonic cross-flow (JISC), showing the flow from the side a) and top b), is provided in Fig. 4.1. The flow configuration consists of a wall with a circular nozzle through which the jet enters the supersonic cross-flow. Along the wall a fully turbulent supersonic boundary-layer (1) has developed upstream of the injection location. The jet that exits the hole penetrates through the boundary-layer into the free stream where it blocks and displaces the supersonic part of the flow. This blockage causes a bow shock (2) in front of the injection, which interacts with the boundary-layer. The shock induced pressure gradient decelerates the boundary-layer flow and eventually leads to boundary-layer separation. The recirculation region thickens the boundary-layer and acts like a compression corner with a separation shock (3). Around the jet's base a horse shoe vortex is created (4) close to the wall. A second large counter-rotating vortex pair (5) rolls around the jet and is transported downstream by the free stream. An additional recirculation forms at the downstream side of the jet. The separated flow regions around the jet exit play an important role with respect to the mixing of the jet and cross-flow fluids. The turbulent mixing and shear layer (6) on the upper side of the jet carries disturbances that originate from the upstream recirculation.

Shear stress due to different velocities in the two streams dominates the near-field mixing-layer development [37]. In this case the vertical velocity of the jet at the exit is very large when compared to the vertical velocity of the free stream, which only has an instantaneous fluctuating component and is close to zero in its mean. Kelvin-Helmholtz instability, triggered by upstream perturbations in the recirculation, leads to periodic vortex formation. The roll up has several effects; it pulls in fluid from both streams and

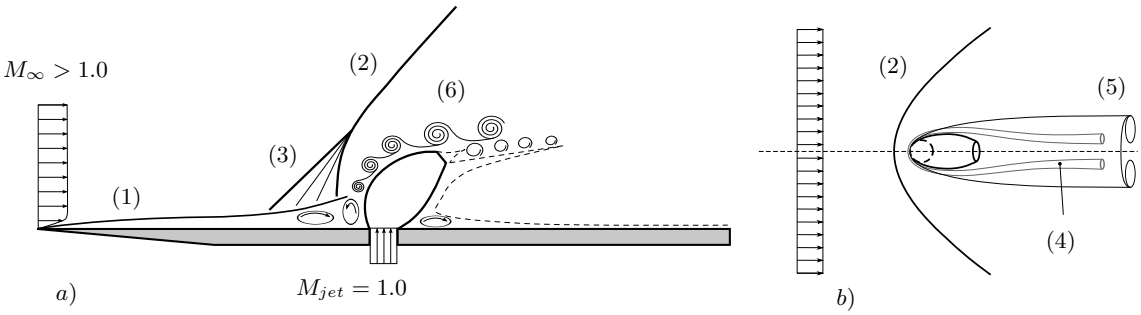

Figure 4.1: Sketch of a jet in supersonic cross-flow from the side $a)$ and top $b)$.

thereby increases the area of the interface between the two fluids. The mixing finally occurs due to molecular diffusion, which is enhanced by the enlarged interface and concentration gradients. The shear rate between the two fluids increases with a rising convective velocity. In general this leads to a faster roll up and entrainment, and consequently to faster mixing. In a free shear layer this also causes an increase in viscous dissipation of kinetic energy to thermal energy, irreversible entropy production and total-pressure loss. In compressible flows the effect of strong roll ups and the associated faster growth rate of shear layers is counteracted by compressibility effects, which decrease the growth rate significantly as the convective Mach number rises. This is described in detail by Pantano and Sarkar in [26]. Near-field mixing is dominated by the macroscopic stirring of the fluids, while the far-field mixing depends on the small scale turbulence and molecular diffusion. For jet in supersonic cross-flow configurations the transition from near-field to far-field mixing occurs at a downstream position of 10 to 20 jet diameters [37]. The simulations in this study put a focus only on the near-field mixing.

The objective of this chapter is (i) the validation of a recently published model [13] for implicit Large Eddy simulation (LES) of supersonic turbulent mixing, and (ii) the comparative evaluation of uncertainties in numerical simulations and experimental data for jet injection into a supersonic cross-flow. As test case an underexpanded sonic air jet that is injected into a supersonic turbulent boundary-layer is considered. The cross-flow Mach number is $M_\infty = 1.6$ and the jet-to-cross-flow momentum ratio is $J = 1.7$. This particular configuration is based on the experimental work of Santiago and Dutton [36], Everett et al. [6] and Lerberghe et al. [43]. Implicit LES (ILES) where subgrid-scale (SGS) turbulence is accounted for by the Adaptive Local Deconvolution Method (ALDM) where conducted. The initial setup (baseline) follows a numerical study of Kawai and Lele [14], who, for computational feasibility reasons, simulated a six times lower Reynolds number as compared to the experiments. Numerical results of Chai and Mahesh [2] are also included in the analysis.

4.2 Flow conditions

A sonic jet entering a supersonic cross-flow of Mach number $M_\infty = 1.6$ is considered. All flow parameters are based on the experimental studies of Santiago and Dutton [36], Everett et al. [6] and VanLerberghe et al. [43]. The jet-to-cross-flow momentum ratio is

$$J = \frac{\rho_{jet} u_{jet}^2}{\rho_{CF} u_{CF}^2} = \frac{p_{jet}}{p_{CF}} \tag{4.1}$$

with ρ being the density, u the velocity and p the dynamic pressure. The subscripts *jet* and *CF* denote quantities in the jet and in the cross-flow, respectively. The cross-flow has a stagnation temperature of $T_{CF,0} = 295K$ and a stagnation pressure of $p_{CF,0} = 241kPa$ as described by VanLerberghe et al. [43]. With the given Mach number this yields a static temperature and pressure of $T_\infty = 195.1K$ and $p_\infty = 56.7kPa$. The jet is defined by its stagnation temperature $T_{jet,0} = 300K$ and pressure $p_{jet,0} = 476kPa$. The jet exit orifice diameter measures $D = 4mm$. The boundary-layer of the cross-flow is fully turbulent and has a thickness of approx. $\delta = 3.1mm$ and a Reynolds number based on its thickness of roughly $Re_\delta = 1.1 \cdot 10^5$ at a position five diameters upstream of the injection. As mentioned before, this Reynolds number is lowered in the baseline simulation to $Re_\delta = 18611$.

4.3 Numerical setup

The Cartesian computational grid, sketched in Fig. 4.2, is locally refined to adapt the different resolution requirements demanded by the flow configuration. Additionally, a hyperbolic point distribution is applied towards the wall to sufficiently resolve the boundary-layer. The grid consist of 4.8 million cells in the boundary-layer region upstream of the injection and of 11.8 million cells for the resolved volume around the jet. Layers of coarse buffer cells surround the resolved part of the grid in order to avoid spurious effects of the boundary conditions. The resolved area measures $10.4D$ in x-direction, $3.9D$ in y-direction and $4D$ in z-direction. The resolution is based on the medium grid size of Kawai and Lele's grid convergence study [14]. In the boundary-layer region it satisfies the $y^+ < 1.0$ condition, the x and z directions are resolved with $x^+ < 25.0$ and $z^+ < 12.5$. The bottom plate with the jet nozzle is modeled as an adiabatic wall in all simulations. The nozzle geometry is included in the computational domain and the nozzle contour is modeled using the immersed boundary technique [22, 23, 25].

The experiment has been conducted in a test section that is large compared to the jet diameter (with a width of $19D$ and a height of $8D$, Everett et al. [6]), which means that the tunnel walls can be neglected in the numerical setup, if only the small volume around the jet is of interest. Therefore a characteristic farfield condition for the top boundary is used

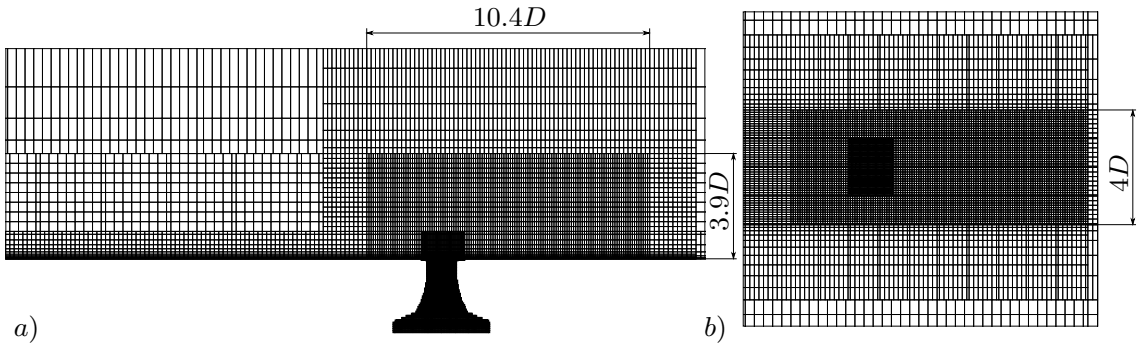

Figure 4.2: Section of the computational grid used for all simulations, displaying every 4th cell. The measures display the resolved part. a) $z/D = 0.0$, b) $y/D = 0.0$ (at the wall).

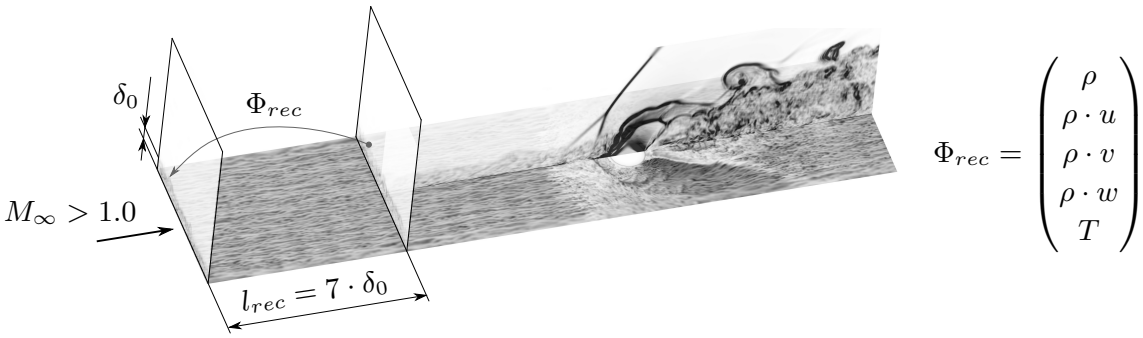

Figure 4.3: Sketch of the recycling mechanism. The density gradient magnitude is displayed on the wall normal slice and the shear on a slice very close to the wall at $y/D = 0.005$.

and the side boundary conditions are symmetries. The distance of the symmetries to the resolved part of the grid is sufficiently large to ensure that shock reflections do not reenter the domain of interest. At the supersonic outlet all gradients are set to zero. A constant total temperature and pressure is applied at the jet nozzle inlet. Transient turbulent inflow data for the supersonic, turbulent boundary-layer is generated by a recycling-rescaling technique as described by Petrache et al. [27]. The basic mechanism of the recycling-rescaling for the JISC simulation is displayed in Fig. 4.3. The flow quantities are recycled in the order: static density, momentums in x, y and z directions and static temperature. A generic quantity Φ_{inflow} at the inflow is computed from

$$\Phi_{inflow} = \langle \Phi_{inflow} \rangle + \sqrt{\frac{\langle \Phi' \Phi'_{inflow} \rangle}{\langle \Phi' \Phi'_{rec} \rangle}} \cdot (\Phi_{rec} - \langle \Phi_{rec} \rangle), \tag{4.2}$$

where $\langle \Phi_{inflow} \rangle$ is the target mean profile and $\langle \Phi' \Phi'_{inflow} \rangle$ are target fluctuation profiles. Φ_{rec} denotes the instantaneous solution at the recycling plane, where the turbulent fluctuations are extracted. $\langle \Phi_{rec} \rangle$ and $\langle \Phi' \Phi'_{rec} \rangle$ are running averages of the mean and variance values at the recycling plane. We note that this method does not distinguish between inner

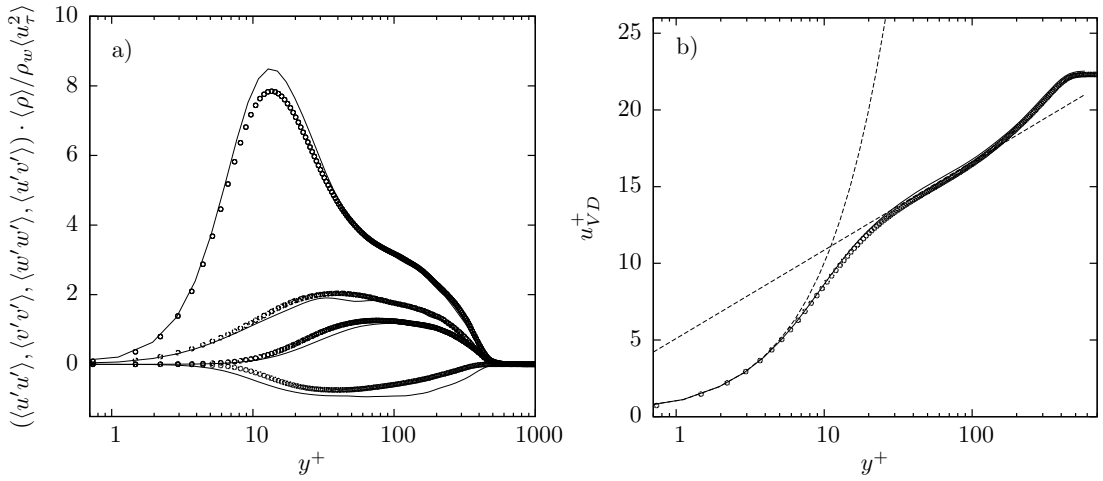

Figure 4.4: a) Reynold stresses with velocity components: $\langle u'u'\rangle$, $\langle v'v'\rangle$, $\langle w'w'\rangle$ and $\langle u'v'\rangle$, b) streamwise velocity profile. ∘ DNS data with $Re_\tau = 450$ by Pirozzoli and Bernardini [28], − present LES with $Re_\tau = 452$.

Table 4.1: Characteristic quantities of the boundary-layer five jet diameters upstream of the injection location.

Re_δ	Re_Θ	Re_τ	δ_1	δ_2	u_τ	c_f	H_{12}
18611	1817	452	0.232	0.0976	0.0468	0.003082	2.377

and outer layers of the boundary-layer, as it underlies the assumption that the growth of the boundary-layer over the recycling length l_{rec} is small when compared to the LES grid resolution at the boundary-layer edge.

4.4 Baseline case

4.4.1 Supersonic turbulent boundary-layer

The baseline case follows the numerical study of Kawai and Lele [14] at a Reynolds number reduced to $Re_\delta = 18611$. To ensure the correctness of the boundary-layer parameters at the experimental reference position (five nozzle diameters upstream of the injection), a separate simulation of the boundary-layer has been conducted. The nozzle has been removed in this simulation to exclude any upstream influence of the injection. The exact same grid as in all JISC simulations is used to ensure comparability. Reynolds stresses and mean velocity profiles for the boundary-layer simulation are presented in Fig. 4.4 with proper density scaling to account for different flow conditions. Good agreement with the reference data from Priozzoli's and Bernardini's DNS [28] for a Reynolds number of $Re_\tau = 450$ and at a different Mach number of $M_\infty = 2.0$ is observed. An overview of the boundary-layer's characteristic non-dimensionalized quantities at a position five diameters upstream of the injection nozzle is given in Table 4.1.

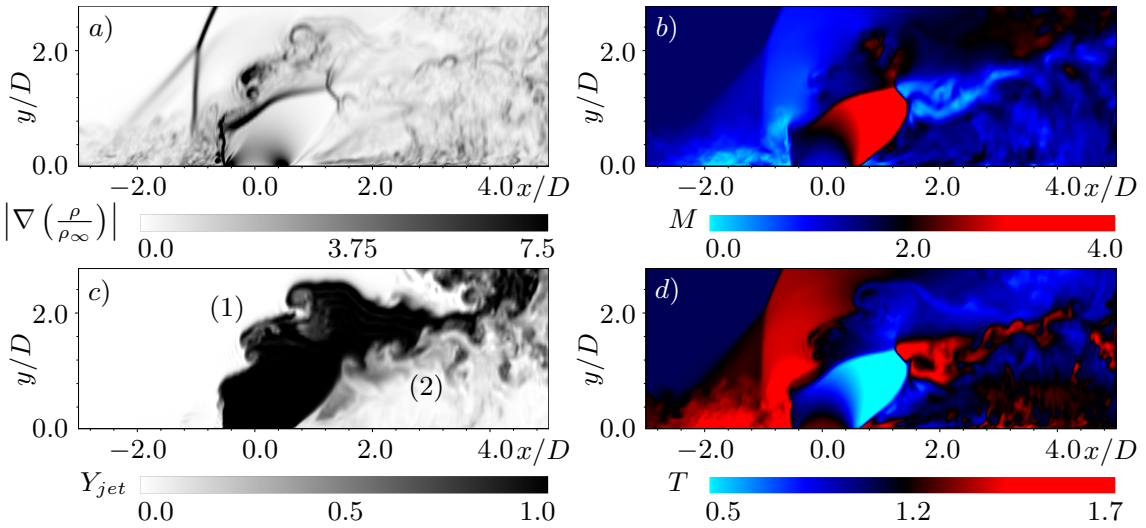

Figure 4.5: 2-D slice at $z/D = 0.0$ showing instantaneous density gradient magnitude a), Mach number b), jet fluid mass fraction c) and static temperature d) of a JISC.

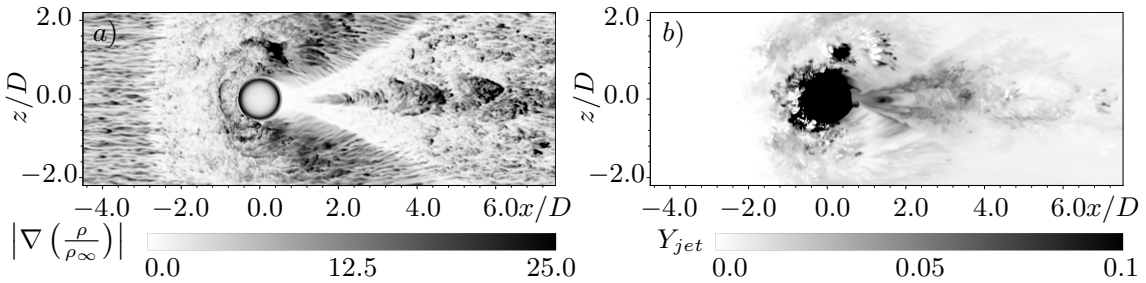

Figure 4.6: 2-D slice at $y/D = 0.005$ showing instantaneous density gradient magnitude a) and jet fluid massfraction b) of a JISC.

4.4.2 Flow visualization

Results for the baseline jet in cross-flow LES are compared to experimental [36, 6, 43] and computational [14, 2] data. Here and in the following all quantities are non-dimensionalized by their free stream counterparts and the jet exit diameter D. Figures 4.5 and 4.6 give an overview of the instantaneous flow field on a wall normal slice ($z/D = 0.0$) and a wall parallel slice ($y/D = 0.005$). The four plots in Fig. 4.5 display the density gradient magnitude a), the Mach number b), the jet fluid massfraction c) and the static temperature d). In Fig. 4.6 the density gradient magnitude is displayed in a) and the jet fluid massfraction in b). The characteristic compressible flow features, such as the primary bow shock and barrel shock with Mach disk are clearly visible. Turbulent structures of different length scales are resolved, e.g., large scales in the jets upstream side mixing layer ((1) in Fig. 4.5 c)), and small scales in the wake at the downstream side ((2) in Fig. 4.5 c)). The upstream recirculation and the signature of the horse shoe vortex are visible in the density gradient top view of Fig. 4.6.

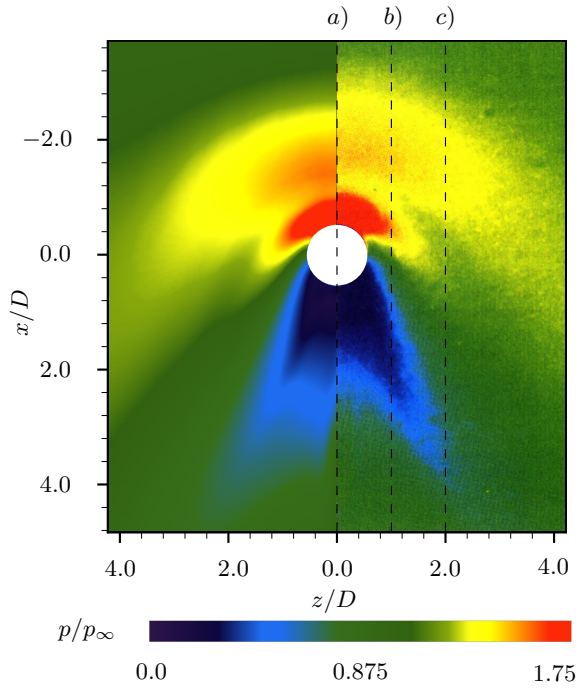

Figure 4.7: Wall pressure distribution, non-dimensionalized by its free-stream value p_∞. Left: LES simulation of this study, right: experimental, obtained from pressure sensitive paint by Everett et al. [6].

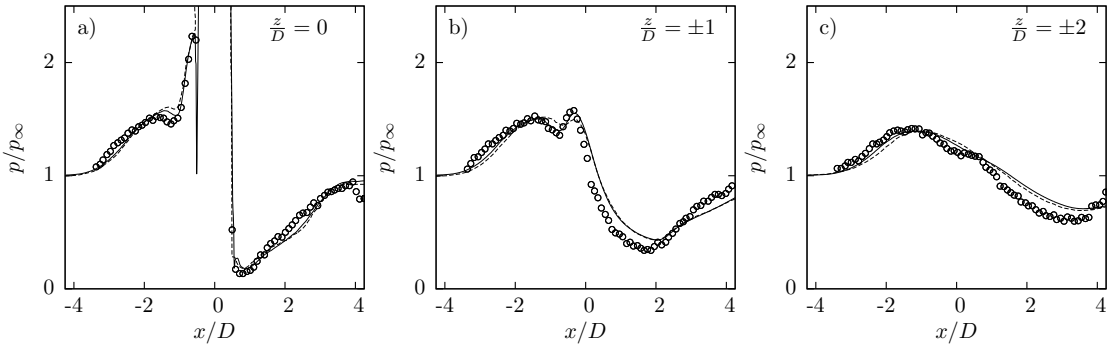

Figure 4.8: Non-dimensionalized wall pressure p/p_∞ at three positions. ∘ experimental Everett et al. [6], − implicit LES with ALDM, - - LES of Kawai and Lele [14].

4.4.3 Mean wall pressure

A quantity that can be accurately measured in supersonic flows is the time averaged wall pressure. Samples for a statistical analysis have been collected for approx. $150D/u_\infty$ in our simulations (jet diameter overflow times). Everett et al. [6] conducted pressure measurements with both pressure taps and pressure sensitive paint. The pressure sensitive paint yields two-dimensional time-averaged data of the wall pressure. A qualitative comparison of this two-dimensional field is displayed in Fig. 4.7. Upstream of the nozzle exit two high pressure regions are visible. The most upstream high pressure region, which has a lower pressure value and is more spread out, originates from the separation bubble and the pressure rise across the separation shock. The second high pressure region is created

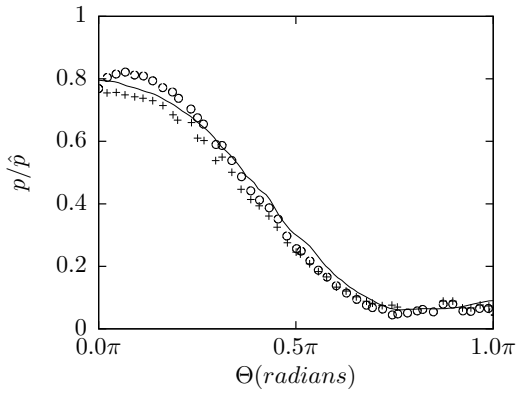

Figure 4.9: Circumferential pressure $p/\hat{p}$ at the wall on a circle $0.34mm$ offset from the nozzle exit. $\circ$ experimental $J = 1.7$ Everett et al.. [6], $+$ experimental $J = 1.2$ Ref. [6], $-$ implicit LES with ALDM.

by the primary bow shock. Its maximum is limited by the theoretical pressure rise across a normal shock at M_∞. The upstream extension of the high pressure region of the simulation seems smaller than that of the experiment. This may be accredited to an inaccuracy of the color scale of the paint measurement. This argument is strengthened by one-dimensional profiles extracted from the pressure-paint data. In Fig. 4.8 three stations are compared: the center line, and lines one and two diameters off the center line. The locations of these profiles are are marked by dashed lines in Fig. 4.7. Upstream of the injection our results for all three stations are in very good agreement with the measurements ($\circ$ symbols) and the reference simulation of Kawai and Lele. [14] (dashed line; Chai and Mahesh. [2] do not provide pressure data). On the centerline the maximum of p/p_∞ reaches a value of 2.25, which is $\approx 80\%$ of the theoretical pressure rise across a normal shock at $M_\infty = 1.6$ and is in very good agreement with the reference data. The two-dimensional low pressure region of our simulation is in excellent agreement with LES data of Kawai and Lele [14] (c.f. Fig. 10a of Ref. [14]). Both simulations, however, show almost identical small deviations from the experimental data in the low pressure region on the downstream side.

In addition the pressure around the jet orifice has been investigated. Our LES results together with two experimental datasets are plotted in Fig. 4.9. It is non-dimensionalized with the pressure $\hat{p}$ behind a normal shock for the free-stream Mach number $M_\infty = 1.6$. The two experimental plots are from JISCs with momentum ratios of $J = 1.2$ ($+$ symbols) and $J = 1.7$ ($\circ$ symbols). The highest values are found in the stagnation region, followed by a drop and a plateau, starting at around $3/4\pi$. The data agrees very well except in the stagnation region, where small deviations are visible. Everett et al. [6] state, however, that there was a fault in the paint in the stagnation region, which they also use to explain the drop in pressure towards $\Theta = 0$.

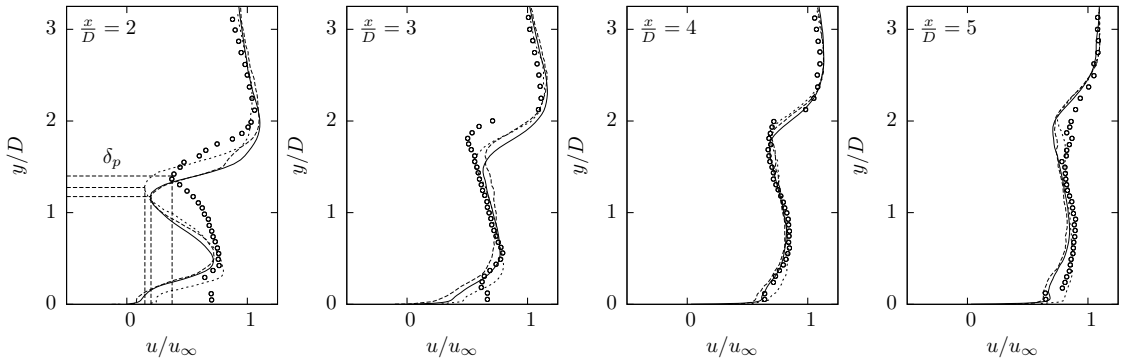

Figure 4.10: 1-D profiles of streamwise velocity u/u_∞ at several downstream stations on the center plane of the simulation. ∘ experimental Santiago and Dutton [36], - - LES Kawai and Lele [14], ⋯ LES Chai and Mahesh [2], − implicit LES with ALDM.

4.4.4 Mean velocity profiles

Wall normal profiles of the streamwise, u, and wall normal, v, velocity components were measured with Laser Doppler Velocimetry (LDV). Figures 4.10 and 4.11 show these profiles at four locations (∘ symbols [36]) together with LES results of Kawai and Lele [14] (dashed line) and Chai and Mahesh [2] (dotted line) and the results of our simulation (solid line). Profiles of streamwise velocity are in excellent agreement with the reference LES data of Kawai and Lele [14] and in good agreement with the LES results of Chai and Mahesh [2] and the experimental data of Santiago and Dutton [36]. Best agreement between all simulations and the experiment is found for the $x/D = 4$ and $x/D = 5$ stations. For the stations closer to the injection ($x/D = 2$ and $x/D = 3$) some discrepancies are observed. First, the experiment shows higher flow speeds in the direct vicinity of the wall than the simulations. Second, the location of the characteristic local minimum in the velocity profile and the value of the minimum velocity (dashed lines) differ. This indicates a lower penetration δ_p of jet fluid into the free-stream. The location of the local minimum in the velocity profiles correlates with the penetration depth since the jet fluid has to be accelerated from a pure vertical motion to follow the free-stream. As the minimum velocity is subsonic, and the subsonic speed behind a shock is determined by its strength, this would indicate a stronger barrel shock in the simulations than in the experiment. This argument is supported by comparison of the maximum Mach number reported in Santiago's and Dutton's experiment $M_{e,max} = 2.66$ [36] and the maximum Mach number of the simulations $M_{s,max} = 3.6$. However, particle lag may have biased the LDV measurements towards a lower Mach number in front of the barrel shock and a higher velocity on the downstream side of the shock, as mentioned in Ref. [36].

While the streamwise velocity is lower than expected, a higher than expected wall normal velocity is observed, see Fig. 4.11. The penetration depth initially (at $x/D = 2$ and $x/D = 3$) is lower than observed in the experiment and agrees well with the experimental

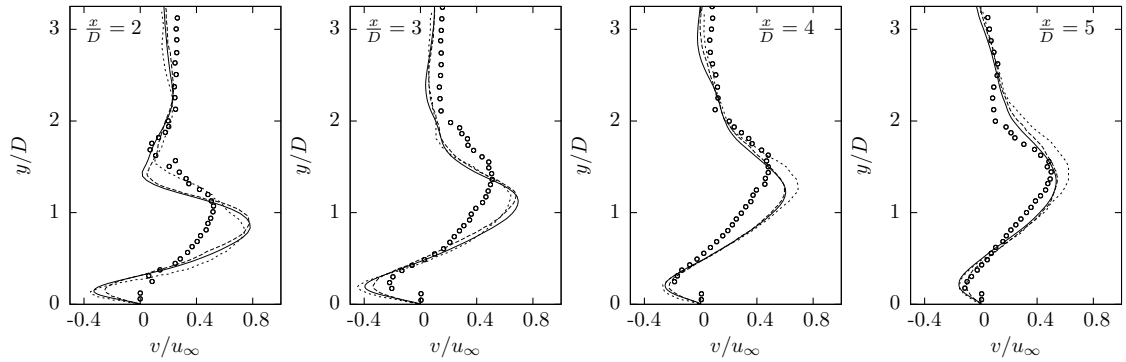

Figure 4.11: 1-D profiles of wall normal velocity v/u_∞ at several downstream stations on the center plane of the simulation. ∘ experimental Santiago an Dutton [36], - - LES Kawai and Lele [14], ⋯ LES Chai and Mahesh [2], − implicit LES with ALDM.

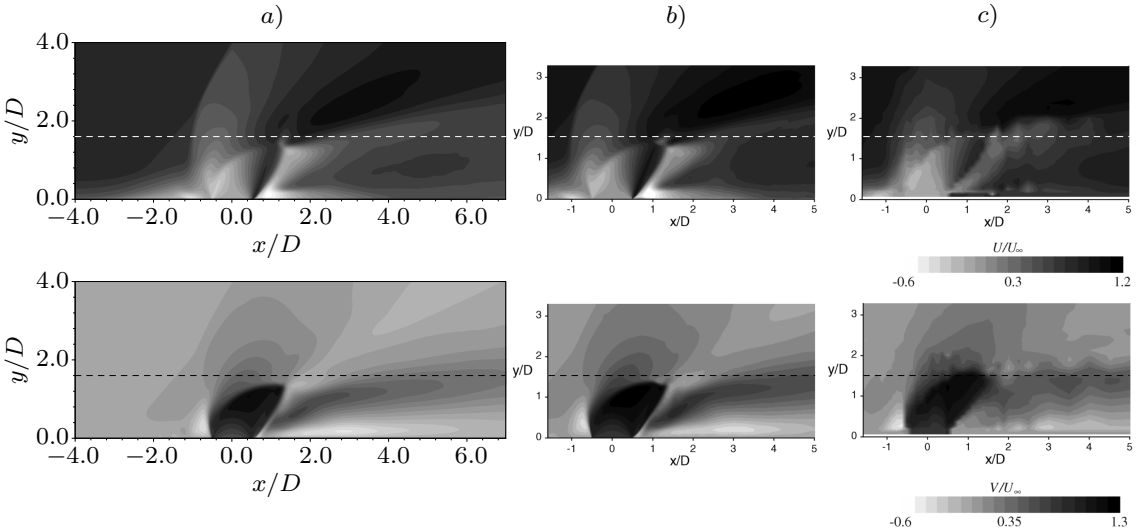

Figure 4.12: 2-D data on a $z/D = 0$ slice of u/u_∞ and v/u_∞ velocities. a) LES of this study, b) LES Kawai and Lele [14] and c) experiment Santiago and Dutton [36] with figures taken from [14].

data at the downstream stations ($x/D = 4, x/D = 5$). This is consistent with an overprediction of the normal velocity at locations of lower penetration depth than in the experiment. In general, profiles of the wall normal velocity show a similar tendency as the streamwise velocity profiles. All simulations deviate from the experiment but agree well amongst each other. The agreement with the experiment improves with increasing distance from the injection.

Besides the one-dimensional profiles, Santiago and Dutton [36] also report two-dimensional measurements which are used for a qualitative comparison of two-dimensional slices. Figure 4.12 shows a wall normal slice on the symmetry plane $z/D = 0$, displaying the streamwise velocity u/u_∞ and the wall normal velocity v/u_∞. The left panel shows our LES results, the middle panel is the LES performed by Kawai and Lele [14], and the right one is taken from experimental measurements by Santiago and Dutton [36]. The

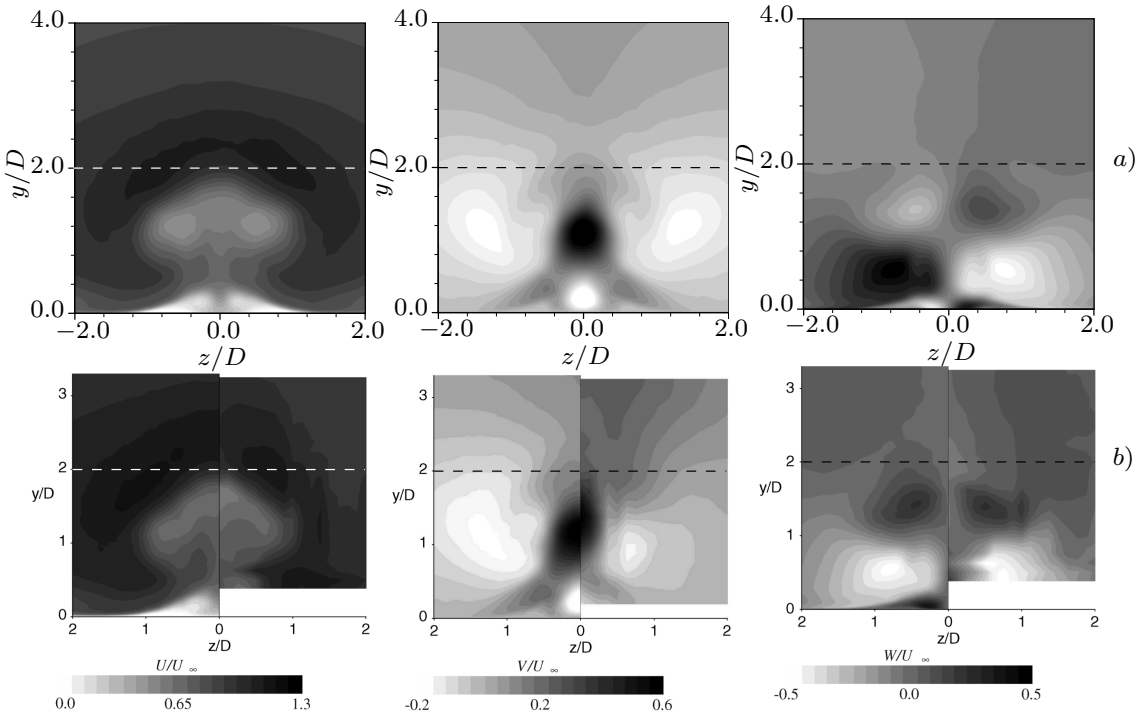

Figure 4.13: Contours for the components of the velocity vector on a 2-D slice at $x/D = 3$. a) implicit LES with ALDM, b) LES Kawai and Lele [14] and experiment by Santiago and Dutton [36] with figures taken from [14].

two LES again match very well. The experiment shows a slightly larger barrel shock. This is consistent with the higher penetration depth of the experiment, which has been observed in the one-dimensional data. A horizontal dashed line has been added to the plots to emphasize the similarity between the simulations and the small deviation from the experiment. In agreement with the discussion of the one-dimensional data, it can be seen that the minimum of the streamwise velocity is lower than in the experiment.

All three velocity components have been measured on the spanwise slice $x/D = 3$. The three velocities obtained by our LES (top row Fig. 4.13) are set side by side with data from the LES of Kawai and Lele [14] (bottom row, left side) and experimental measurements [36] (bottom row, right side). In addition to the differences discussed previously, the two primary counter rotating vortices developing around the jet and the smaller secondary vortices near the wall can clearly be observed in these plots.

The last quantities for this validation are the time averaged turbulent kinetic energy k (TKE)

$$k = (\langle u'u' \rangle + \langle v'v' \rangle + \langle w'w' \rangle)/(2u_\infty^2) \tag{4.3}$$

and the Reynolds shear stress

$$\langle u'v' \rangle / u_\infty^2. \tag{4.4}$$

In equations (4.3) and (4.4) u_∞ is the free-stream velocity and the superscript $'$ marks the fluctuations of the velocity components u, v, and w. These results are displayed in

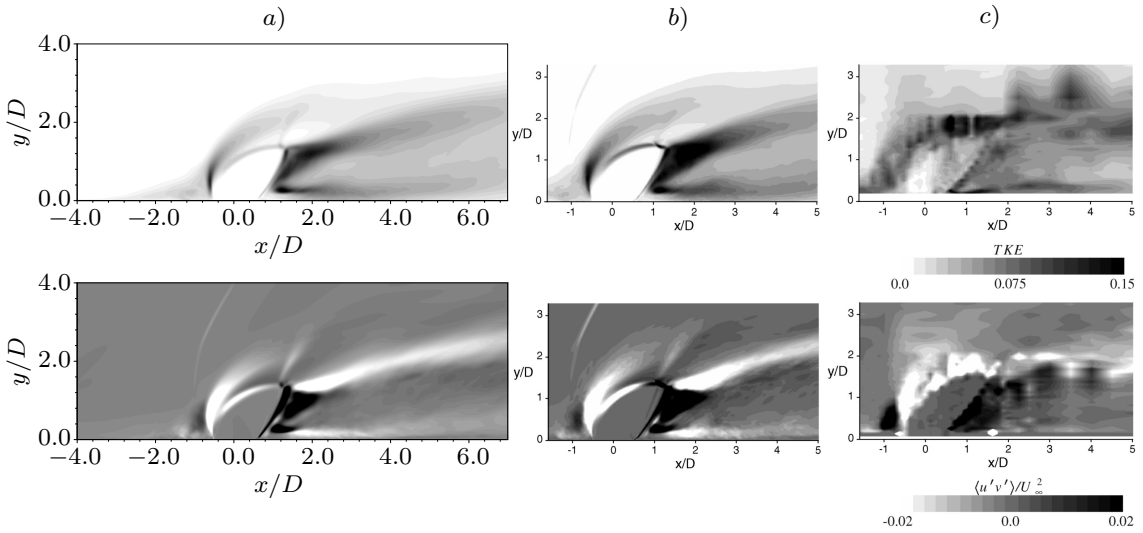

Figure 4.14: Turbulent kinetic energy calculated by Eq. (4.3) and Reynolds shear stress by Eq. (4.4). a) results for implicite LES with ALDM, b) LES by Kawai and Lele [14] and c) experiment by Santiago and Dutton [36] with figures taken from Ref. [14].

Fig. 4.14, the left column a) is again our LES, the middle column b) the LES conducted by Kawai and Lele [14] and the right column c) are experimental measurements by Santiago and Dutton [36]. As the experimental figures show a high level of noise, the comparison, although only quantitatively, is less accurate than for the mean flow. It can be noted, that the absolute values of the TKE are highest in the subsonic region behind the injection in both simulations, while the experiment indicates the highest values above the jet. Additionally, the values are higher in Kawai's and Lele's simulation than in our LES, which may be due to the difference in grid resolution and different numerical methods and SGS models employed by the two studies.

In conclusion, excellent agreement in the wall pressure comparison with the experimental measurements, as well as with other numerical investigations is obtained. Mean velocity field and turbulence statistics agree very well with previous simulations, which allows the conclusion that our numerical model is accurate in simulating a JISC. Results for all simulations, however, slightly deviate from the experimental data. The most significant discrepancy is observed in the penetration depth of the jet at the $x/D = 2$ and $x/D = 3$ stations.

4.5 Parameter variation

4.5.1 Uncertainty parameters

In order to analyze the cause of the differences between the three LES and the experiment, a parameter variation has been performed. First, the Reynolds number of the flow is

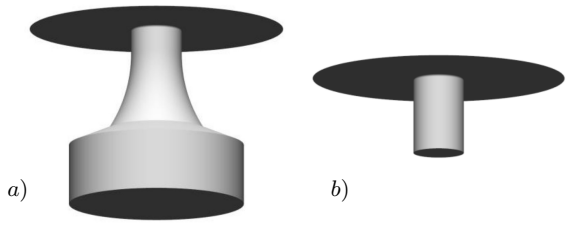

Figure 4.15: Render graphic of two different nozzle geometries. The boundary condition is applied a distance above the lower opening. a) baseline geometry, b) case (F, see Table 4.2) geometry.

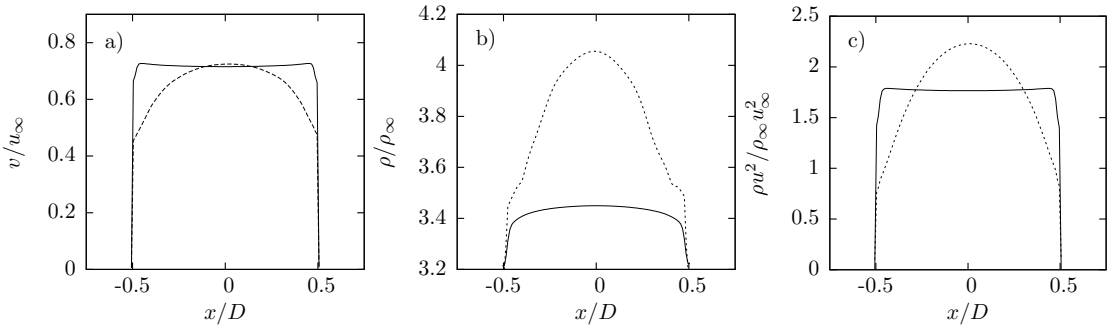

Figure 4.16: Jet nozzle exit profiles for − baseline nozzle, and ··· modified nozzle. a) vertical velocity v/u_∞, b) density ρ/ρ_∞ and c) momentum $\rho u^2/\rho_\infty u_\infty^2$.

varied. This is the obvious starting point when searching for reasons for differences since this parameter has been intentionally changed for reducing the resolution requirements in the simulations, as mentioned earlier. Therefore the Reynolds number has been adjusted to twice the baseline value, then four times and in a last step to six times the baseline value, which corresponds to the experimental value. Second, the total temperature and total pressure are changed in separate simulations to slightly increase the momentum ratio. The third influencing parameter studied is the nozzle geometry, Fig. 4.15, and, in the same simulation, the inflow profile, Fig. 4.16, at the nozzle inlet. In all other simulations of this study a constant total pressure and total temperature are prescribed at the bottom of the jet nozzle. This results in a naturally developed velocity and density profile at the jet nozzle exit, which is plotted with a solid line in Fig. 4.16 a). The dashed line is the nozzle-exit profile for the modified nozzle. This profile results from replacing the convergent nozzle with a constant area tube with a length of $l_{tube} = 1D$ and prescribing a parabolic velocity profile at the inlet located at the bottom. The density, Fig. 4.16 b), is adjusted such that the momentum, Fig. 4.16 c), integrated across the exit area is the same as in the original configuration. Table 4.2 summarizes all simulated cases with changes relative to the baseline (bl) case. The individual simulations are referred to by the capital letters given in the table, the original setup is referred to as baseline for the remainder of the document.

Table 4.2: Variation of uncertain parameters relative to the baseline (*bl*) configuration.

case	*Re*	T_0	p_0	geometry
(A)	$Re = 2Re_{bl}$	*bl*	*bl*	*bl*
(B)	$Re = 4Re_{bl}$	*bl*	*bl*	*bl*
(C)	$Re = 6Re_{bl}$	*bl*	*bl*	*bl*
(D)	$Re = 6Re_{bl}$	$T_0 = 0.9T_{0,bl}$	*bl*	*bl*
(E)	$Re = 6Re_{bl}$	*bl*	$p_0 = 1.1p_{0,bl}$	*bl*
(F)	$Re = 6Re_{bl}$	*bl*	*bl*	profile, see Fig. 4.16 geometry, see Fig. 4.16

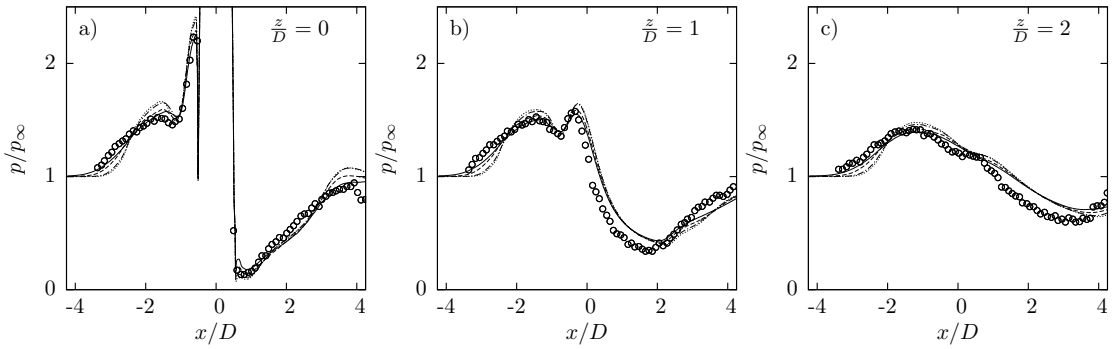

Figure 4.17: Effect of Reynolds number on non-dimensionalized wall-pressure. ∘ experimental Everett et al. [6], − baseline, −− case (A), −· case (B), ··· case (C).

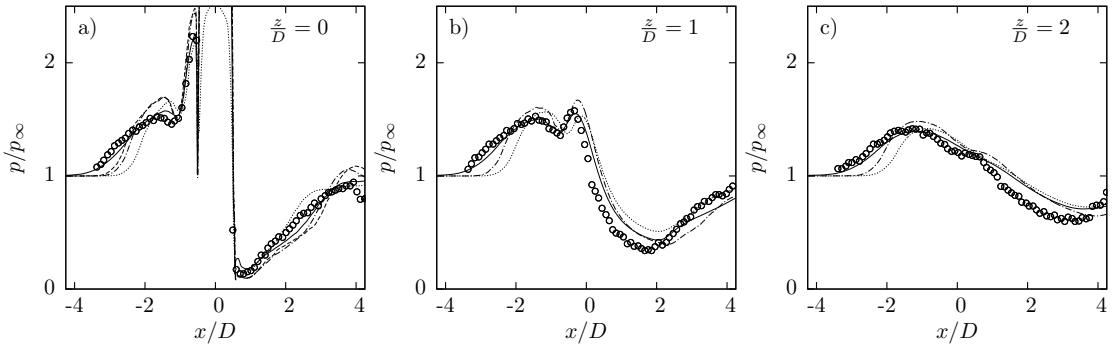

Figure 4.18: Effect of nozzle geometry and nozzle-inlet total pressure and total temperature on non-dimensionalized wall-pressure. ∘ experimental Everett et al. [6], − baseline, −− case (E), −· case (D), ··· case (F).

4.5.2 Effect on wall-pressure

Investigating the wall-pressure at the same locations as in Section 4.4.3, Fig. 4.8, it can be seen in Fig. 4.17 that the effect of the Reynolds number on the wall pressure is relatively small. It affects mainly separated flow regions, which become smaller with lower viscosity. The separation shock is steeper and thus stronger for a shorter recirculation, so the first pressure peak is slightly higher than in the baseline simulation. Surprisingly, the baseline LES which has the lowest Reynolds number, agrees better with the experimental

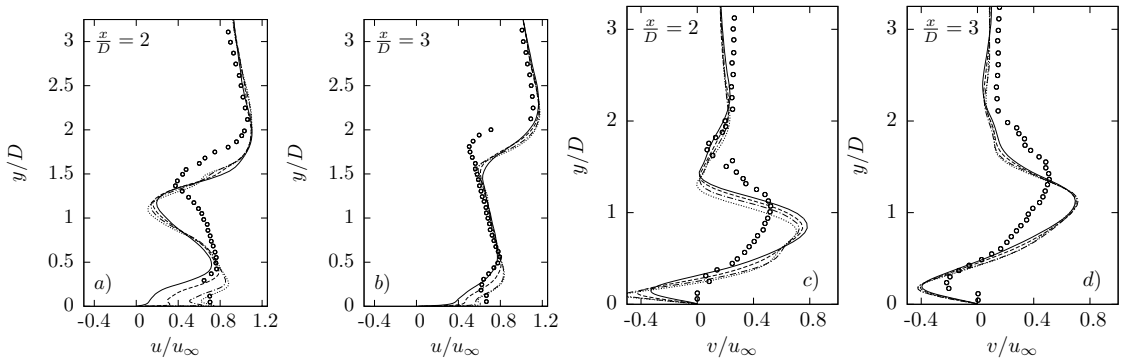

Figure 4.19: Effect of Reynolds number on profiles of streamwise u/u_∞ and vertical v/u_∞ mean velocities at two downstream stations on the center plane of the simulation. ∘ experimental Everett et al. [6], − baseline, −− case (A), −· case (B), ··· case (C).

data than case (C) with the realistic Reynolds number. The simulations with changed inflow conditions are conducted with the highest Reynolds number. In the plots of Fig. 4.18 very little influence of the change in total pressure and temperature is visible, whereas the particular choice of the nozzle geometry has a larger effect. The modified nozzle-exit profile has less momentum at the jet edges than in the jet center. As a result, there is less momentum exchange at the edges of the jet when it exits the nozzle and consequently recirculations and pressure rise are reduced.

4.5.3 Effect on velocity profiles

Figures 4.19 shows profiles of the streamwise, a) and b), and wall normal, c) and d), velocity for the simulations with changed Reynolds number. Only the two stations near the injection are plotted, since the differences diminish further downstream of the nozzle exit. The most significant influence of the Reynolds number can be seen close to the wall. Even if the trend is correct, as already stated, the grid resolution is not sufficient in the near wall region for the simulated Reynolds numbers. Therefore near wall results will not be evaluated further. Furthermore, Fig. 4.19 shows that the location and peak value of the velocity minimum is not notably affected by the Reynolds number. However, the overall shape of the profiles has the tendency to agree better with the experiment.

Changing the total pressure, temperature and inflow profile has a visible effect on the local velocity minimum, see Fig. 4.20. The location is shifted slightly upwards, as expected, because the modified boundary condition results in a slightly increased momentum ratio. The simulation with the modified nozzle geometry shows the most significant difference when compared to the rest of the simulations. The location of the local velocity minimum moves closer to the wall and the actual minimum velocity is almost identical to the experiment, see vertical dashed line in Fig. 4.20 a). At the $x/D = 3$ station the profile already recovers the general shape of the other simulations.

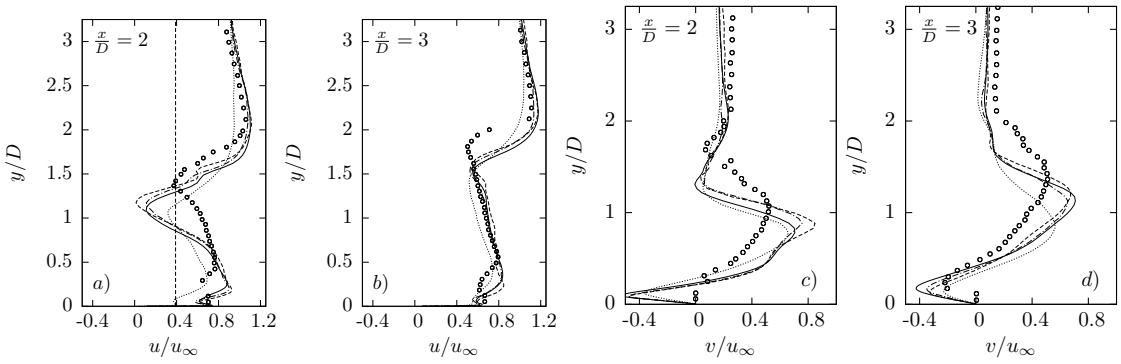

Figure 4.20: Effect of nozzle geometry and nozzle-inlet total pressure and total temperature on profiles of streamwise u/u_∞ and vertical v/u_∞ mean velocities at two downstream stations on the center plane of the simulation. ∘ experimental Everett et al. [6], − case (C), −− case (E), −· case (D), ··· case (F).

In comparison to the streamwise velocity, the vertical velocity is generally less affected by the parameters investigated here. The most prominent effect can be seen at $x/D = 3$ for the inflow profile variation (F).

4.5.4 Effect on Mach number

Figure 4.21 shows the time averaged two-dimensional Mach number statistics for all four simulated Reynolds numbers. In contrast to the one-dimensional velocity profiles, a strong influence of the Reynolds number can clearly be seen. The maximum Mach number in the jet significantly increases with rising Reynolds number from $M_{max} = 3.6$ for the baseline to $M_{max} = 4.2$ for case (C). To visualize this effect, the sonic line, a $M = 3.5$ and a $M = 4.0$ isoline have been added to the plots in Fig. 4.21. The recirculation regions for the high Reynolds number cases shrink, which results in a larger expansion angle α at the downstream side of the nozzle exit, see Fig. 4.22. The larger downstream expansion together with the unchanged penetration depth also increases the size of the Mach disk, which is clearly visible in Fig. 4.21. As the Mach disk is a normal shock in the jet flow, this also affects the subsonic region following the jet: a larger Mach disk leads to a larger subsonic region. The lowest maximum Mach number, which is also smaller than the one of the baseline simulation, yields the modified nozzle (F), see Fig. 4.23. Results for case (F) resemble the experimental value closest of all simulations. However, the value measured in the experiment is still lower.

4.5.5 Effect on jet penetration depth

The penetration depth δ_p of the jet is visualized in Fig. 4.22 with isolines of jet-fluid massfractions for the baseline and cases (a), (B) and (C). The inner line corresponds to 95% jet-fluid and indicates the core of the jet. The outer boundary of the jet is visualized

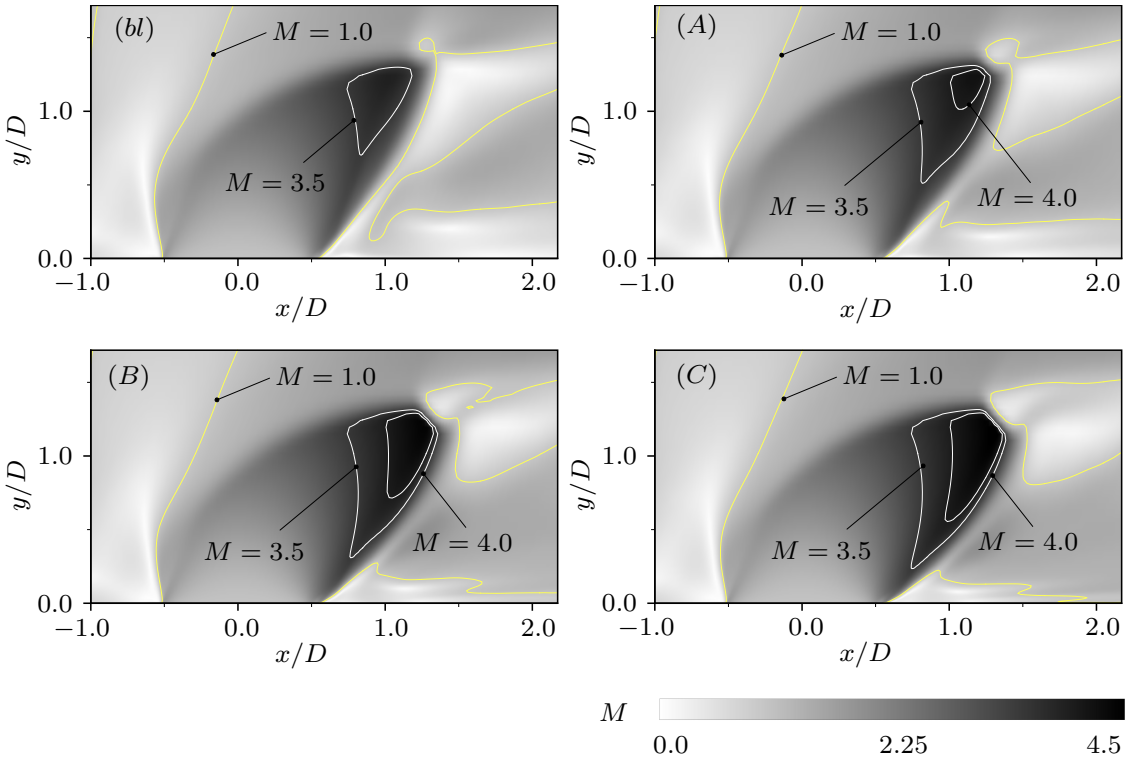

Figure 4.21: Contour plot for time averaged Mach number comparison of the baseline simulation with cases (A)-(C), the yellow solid line marks the sonic line.

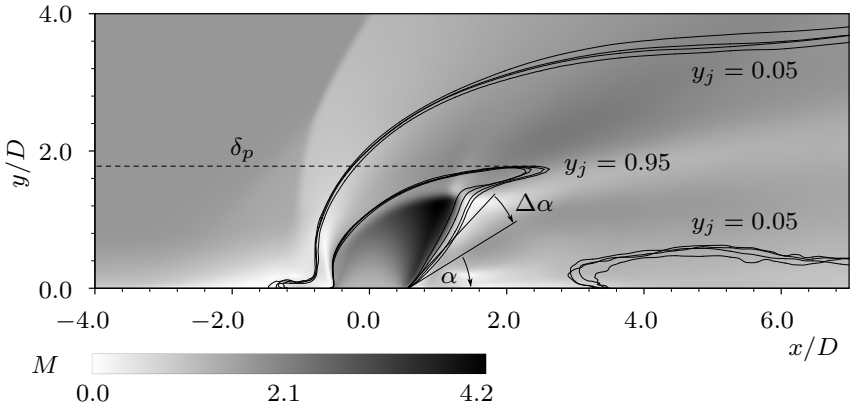

Figure 4.22: Contour plot of the Mach number with added isolines of 5% and 95% jet fluid mass fraction of the baseline simulation and cases (A)-(C). Angle α depicts the expansion angle, $\Delta\alpha$ is the change from weakest to strongest expansion.

by isolines of 5% massfraction.

There are empirical correlations for the jet penetration depth with fitted constants for specific flow conditions. For these fits, typically the penetration depth is defined as the 1% or 0.5% massfraction line of jet-fluid, which is the outer boundary of the jet. The functional

$$\frac{y}{D} = A \cdot J^B \cdot \left(\frac{x}{D} + C\right)^E \cdot \left(\frac{\delta}{D}\right)^F \cdot \left(\frac{M_j}{M_{cf}}\right)^G \tag{4.5}$$

described by Segal [37] is employed to calculate a theoretical penetration depth for the

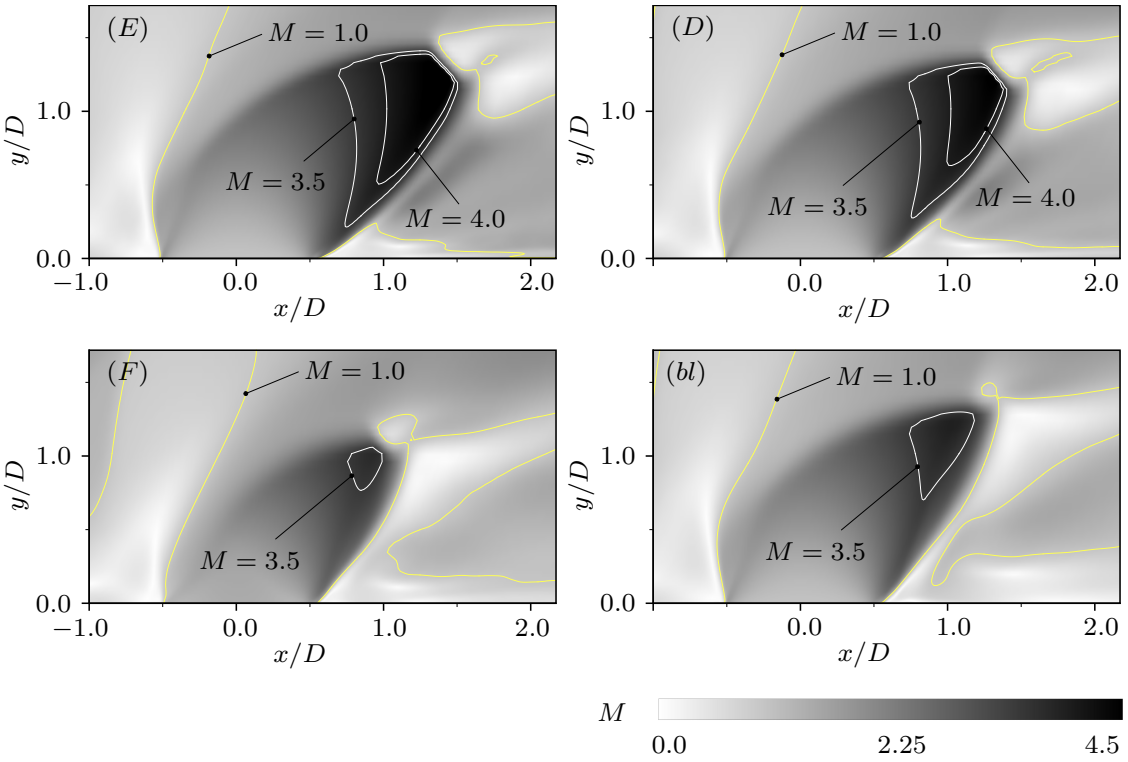

Figure 4.23: Contour plot for time averaged Mach number comparison of the baseline simulation with cases (D)-(F), the yellow solid line marks the sonic line.

JISC. In this equation A,B,C,E,F and G are empirical constants. D is the jet exit diameter, x and y spatial coordinates, δ the boundary-layer thickness in front of the jet, J the jet to cross-flow momentum ratio and M_j and M_{cf} the mole mass of jet and cross-flow fluids respectively. Two sets of constants are evaluated in this study, one for a $M_\infty = 1.5$ JISC and one for $M_\infty = 2.0$, see Table 4.3. The two curves together with our simulated 1%

Table 4.3: Constants used in Eq. (4.5), taken from Falempin [7] and Hersch et al. [19].

constant	A	B	C	E	F	G
$M_\infty = 1.5$, Ref. [7]	1.45	0.5	0.5	0.35	0	0
$M_\infty = 2.0$, Ref. [19]	1.92	0.35	0.5	0.277	0	0

jet-fluid lines have been plotted in Fig. 4.24. The green dotted line corresponds to the $M_\infty = 2.0$ parameter set of Hersch et al. [19], the red dashed line represents the parameter set calibrated for $M_\infty = 1.5$ by Falempin [7]. It is interesting to note that for a constant momentum ratio, a higher free-stream Mach number yields a deeper penetration into the cross-flow close to the nozzle exit. The figure also shows that for $x/D > 6$ all our simulations fit into the range between these two curves except simulation (E), which is the one with higher jet pressure and larger momentum ratio. While the empirical constants lock the correlation to a specific Mach number, Portz and Segal [30] proposed to replace the constants by Mach number dependent expressions. These expressions lead to a curve that yields a too low penetration depth compared to all data gathered here and hence will not

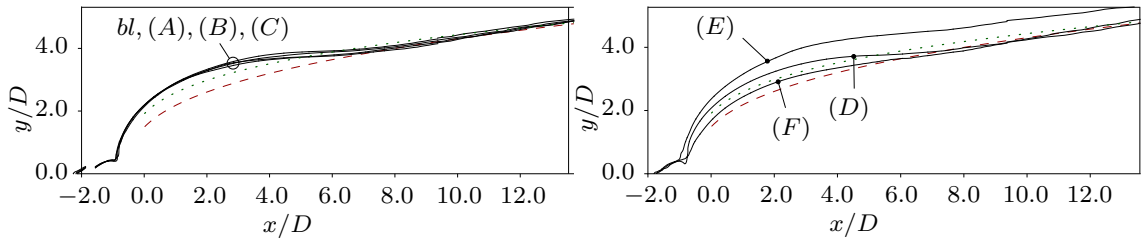

Figure 4.24: Jet penetration depth of all simulations compared with analytical solutions. Left: baseline and simulations A-C, right: simulations D-F. Green dotted line: analytical $M_\infty = 2.0$ from Hersch et al. [19], red dashed line: analytical $M_\infty = 1.5$ from Falempin [7].

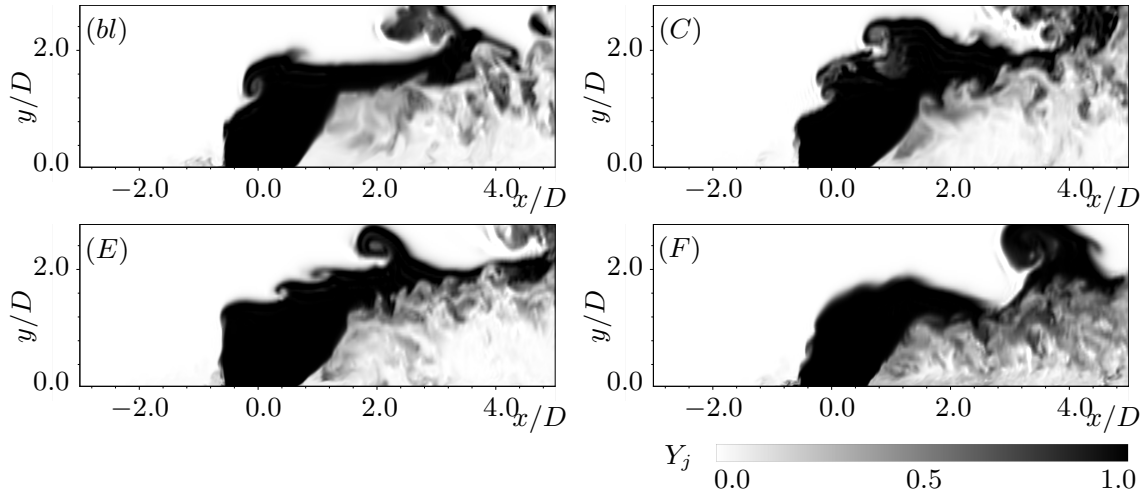

Figure 4.25: Contours of the instantaneous jet-fluid massfraction. (bl) baseline case, (C) highest Reynolds number case, (E) increased injection pressure, (F) inflow profile variation.

be considered. Equation (4.5) is laid out in a way that individual influencing parameters can be switched off by setting their exponent to zero. For the chosen sets of constants the terms for the boundary-layer thickness and mole masses are unity. Consequently the momentum ratio dominates the result. A discussion in Ref. [11] concludes that even with all terms active in Eq. (4.5), the momentum ratio still has the largest influence. Our simulations yield the same penetration depth for all cases as long as the momentum ratio is not changed, which confirms the main influence of the momentum ratio in Eq. (4.5).

4.5.6 Effect on turbulent structures

While the time averaged mass fraction of the jet-fluid does not reveal large deviations across the parameter study, see Fig. 4.22, instantaneous visualizations, Fig. 4.25, show a strong influence of the flow conditions. As a consequence of the lower viscosity in the cases (A), (B) and (C), more small turbulence structures are visible than in the high viscosity baseline case. Case (F) shows completely different characteristics. The upper side develops larger single vortices and the jet plume is much closer to the wall and more

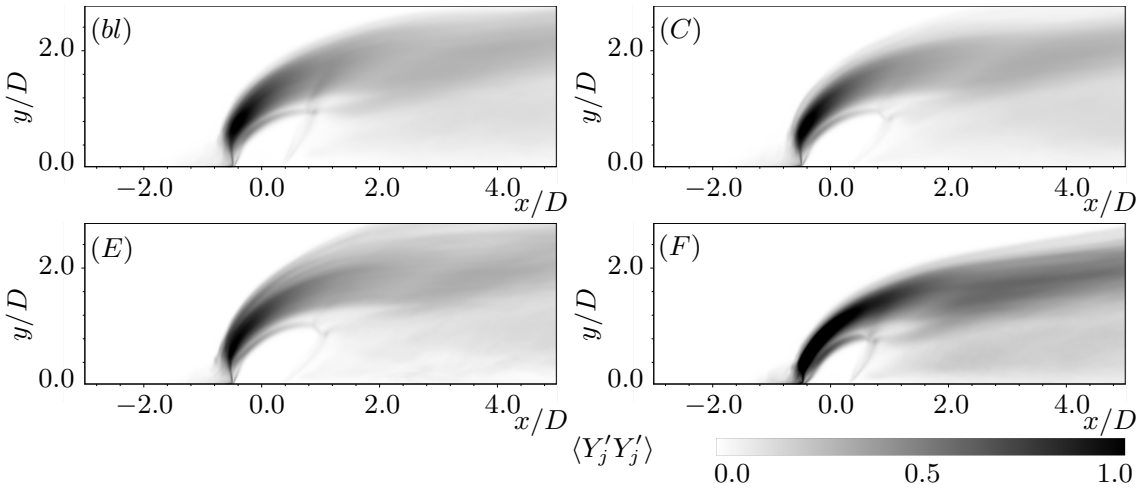

Figure 4.26: Variance of the jet fluid massfraction on the symmetry slice $z/D = 0.0$. (bl) baseline case, (C) highest Reynolds number case, (E) increased injection pressure, (F) inflow profile variation.

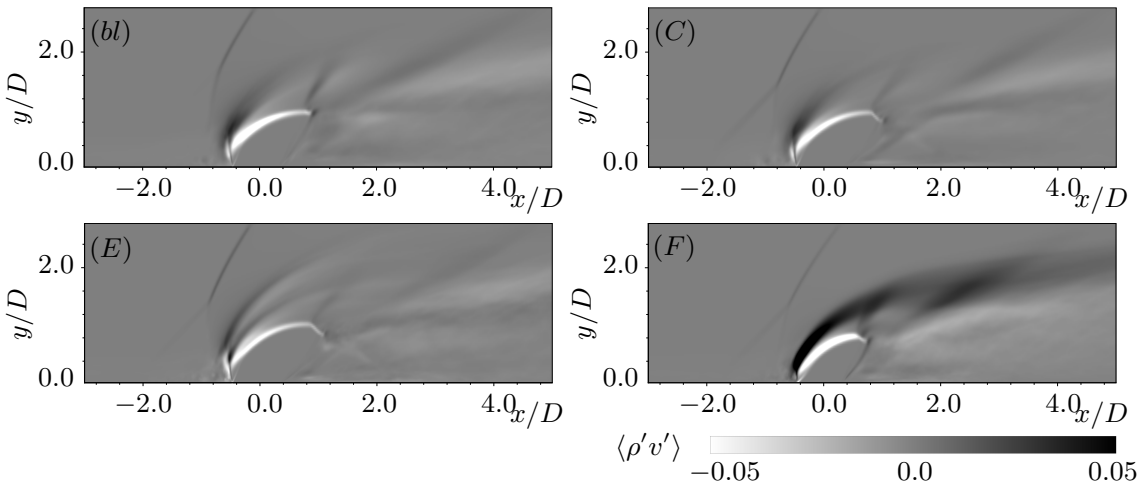

Figure 4.27: Turbulent transport in wall normal direction on the symmetry slice $z/D = 0.0$. (bl) baseline case, (C) highest Reynolds number case, (E) increased injection pressure, (F) inflow profile variation.

turbulent in its center. Additionally the jet fluid is transported quicker to regions near the wall. In a reacting scenario this might promote boundary-layer burning and significant wall heating.

The intensified turbulence in simulation (F) is also clearly visible in the variance of jet-fluids massfraction, Fig. 4.26, and the time averaged wall normal turbulent transport, Fig. 4.27. Both plots show the maximum values for the case with modified profile (F). The simulation with increased injection pressure, case (F), shows improved mixing and a larger vertical extend of the jet-fluid distribution in Fig. 4.26. A pronounced band of higher variance values is visible on the upstream side of the jet. This band is less visible in case (C) and merged with the outer borders for the baseline case and case (F). The same quantities (variance of the massfraction and wall normal turbulent transport) are

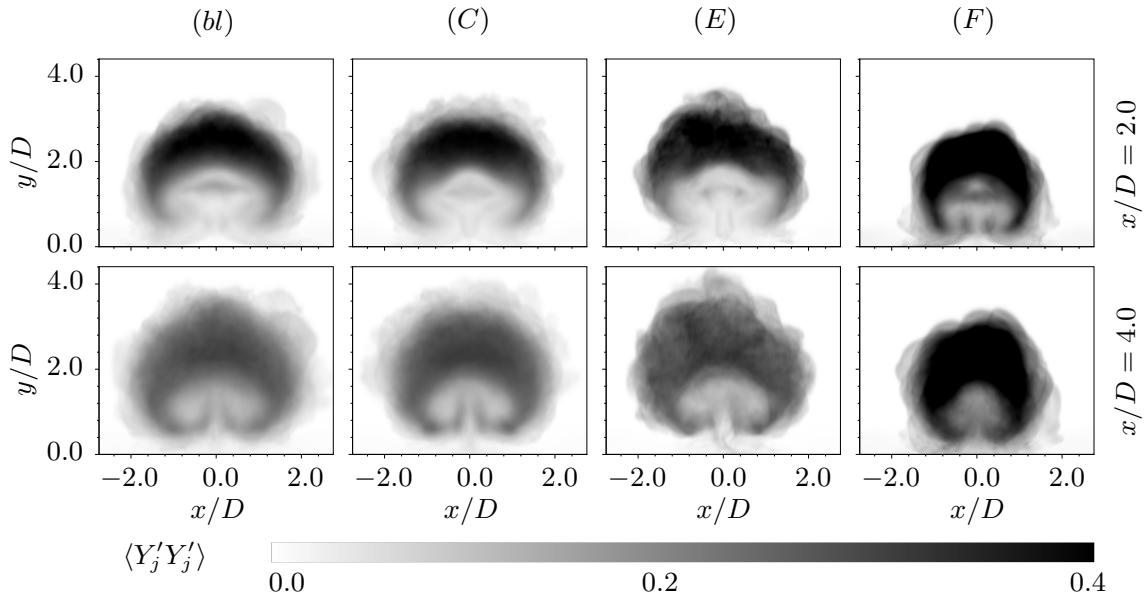

Figure 4.28: Variance of the jet fluid massfraction at the stations $x/D = 2.0$ and $x/D = 4.0$. Displayed are the baseline case, highest Reynolds number case (C), increased injection pressure (E) and the inflow profile variation (F).

displayed in Figs. 4.28 and 4.29 on two slices with constant x coordinate at $x/D = 2.0$ and $x/D = 4.0$. Especially in the variance plots the large, counter rotating vortice pair is visible at both positions. As the mixing progresses, the variance and the turbulent transport intensities are smaller at the location further downstream ($x/D = 4.0$). The figures show, that case (E) leads to the widest jet-fluid distribution in wall normal direction. The horizontal extend of the mixing zone is equal in all simulations except case (F). This case shows a smaller wall normal and horizontal extend of the mixing zone than the other cases. In turn the mixing intensity is much higher for this simulation as previously shown in Figs. 4.26 and 4.27.

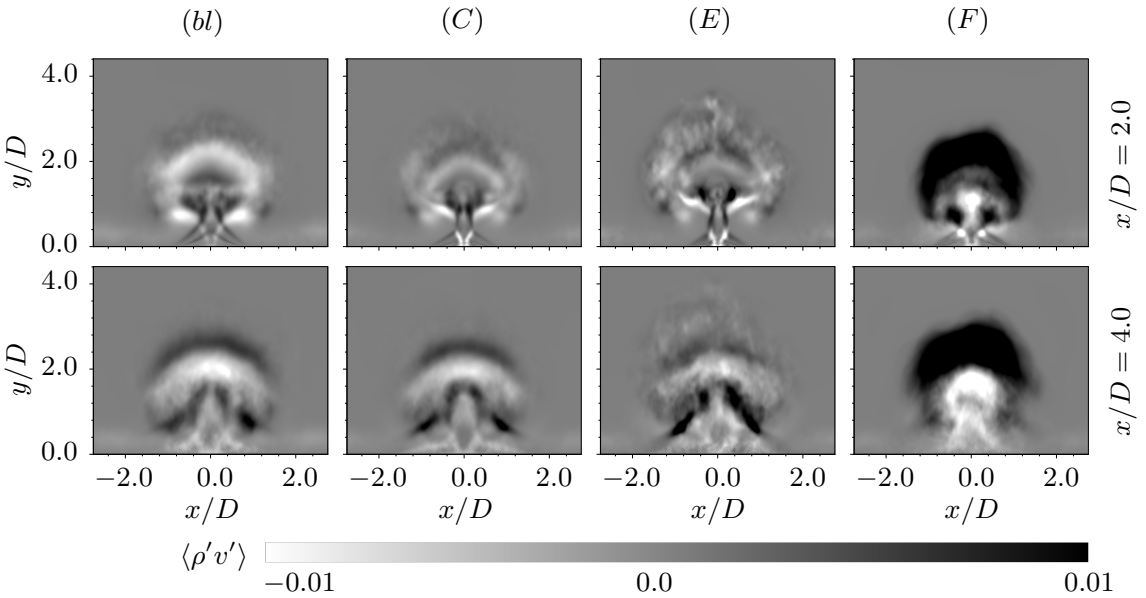

Figure 4.29: Wall normal turbulent transport at the stations $x/D = 2.0$ and $x/D = 4.0$. Displayed are the baseline case, highest Reynolds number case (C), increased injection pressure (E) and the inflow profile variation (F).

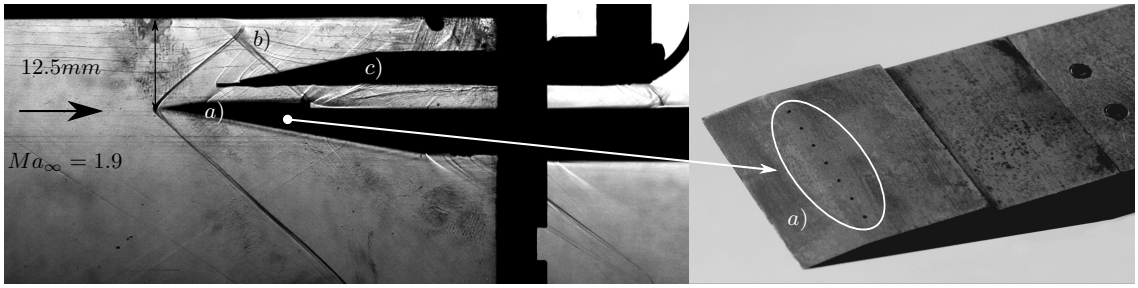

Figure 5.1: Experimental Schlieren image of the investigated injector half-model. Clearly visible primary shockwave from the strut a) with reflection from the channel wall b). Additionally a CO_2 measurement probe c) can be seen.

5 Extension to a strut injector with CO_2 test gas injection

5.1 Case description strut injector study

In large scramjet combustors it is challenging to inject fuel from the walls into the core of the air flow. This is mainly due to the high momentum of the crossflow compared to the momentum in the fuel jet. Injection from the combustor walls can be inefficient or even infeasible, because achieving the required large penetration depth may result in prohibitive losses. For this reason strut injectors are used in large chambers, which consist of small wedges or blades that are positioned in the core flow, for fuel injection. Several configurations of injecting fuel are possible, e.g., perpendicular injection from the upper and lower injector walls, or streamwise injection from the injector base. Besides various injection concepts there are a range of possibilities for the struts geometry. Most geometric designs aim at generating vortices that increase the mixing rate between fuel and air. The fuel is typically in its gas phase to avoid additional delay times due to jet breakup and vaporization.

The simulations conducted in this study are based on the experiment of Gurtner and Paukner [20]. This study considers a half-model of a generic wedge type strut injector with perpendicular injection on its upper wall. Carbon dioxide (CO_2) is used as an injection test gas. The left part of Fig. 5.1 shows a schlieren picture of the test-section during operation. The primary shock at the struts (a) leading edge is clearly visible as is its reflec-

tion from the channels upper wall (b). A probe (c) for measuring the CO_2 concentration is introduced in the experiment. On the right side of Fig. 5.1 a photograph of the strut half-model is shown. The struts base and seven CO_2 injection holes are marked.

5.1.1 Jet in supersonic cross-flow in a combustor model

A schematic of the flow configuration, showing the flow from the side a) and top b) is provided in Fig. 5.2. The setup consists of a channel with a wedge in the center. The upper side of the wedge is the model of a strut injector including circular injection holes on its top.

The air flow from left to right has a fully turbulent supersonic boundary layer at the top wall. The leading edge of the strut generates a shock wave (1), which reflects at the top wall in a shock-wave boundary-layer interaction (2). Hereby, the adverse pressure gradient causes separation and thus the reflected shockwaves foot is located a short distance upstream of the incident shock. This reflected shock (3) enters the mixing zone of the injection and is either reflected again on the strut surface or enters the struts wake, depending on the shock strength that determines the recirculation size. On top of the strut, injection holes are positioned through which jets exit and penetrate into the supersonic free stream. They block and displace the supersonic flow; this blockage causes bow shocks (4) in front of the injections, which interact with the upstream boundary layer. The boundary layer separates due to the induced pressure gradient. Consequently the recirculation region thickens the boundary layer and acts as a compression corner with a weak separation shock (5). The bow shocks of the injections enter the wakes of the neighboring jets and interact with their shear layer and mixing mechanisms. Around the jets, close to the wall, horse shoe vortices develop (8). A second, larger, counter-rotating vortex pair (9) rolls around each jet and is transported downstream. An additional recirculation forms at the downstream side of the jets. The separated flow regions around the nozzle exits play an important role with respect to the mixing of the jet and crossflow fluids. The turbulent mixing and shear layer (6) on the upper side of the jet carries disturbances that originate from the upstream recirculation. Small subsonic regions (7) are present behind the Mach disks and barrel shocks.

5.1.2 Supersonic mixing layer

In general, two regimes of mixing can be observed in a multi component shear layer. The first is the near-field mixing, which is dominated by the macroscopic stirring of the fluid by large scale periodic vortices. The second, the far-field mixing, takes over further downstream and works on the small scales through molecular diffusion [37]. In case of a JISC, the vertical velocity of the crossflow is very small compared to the vertical

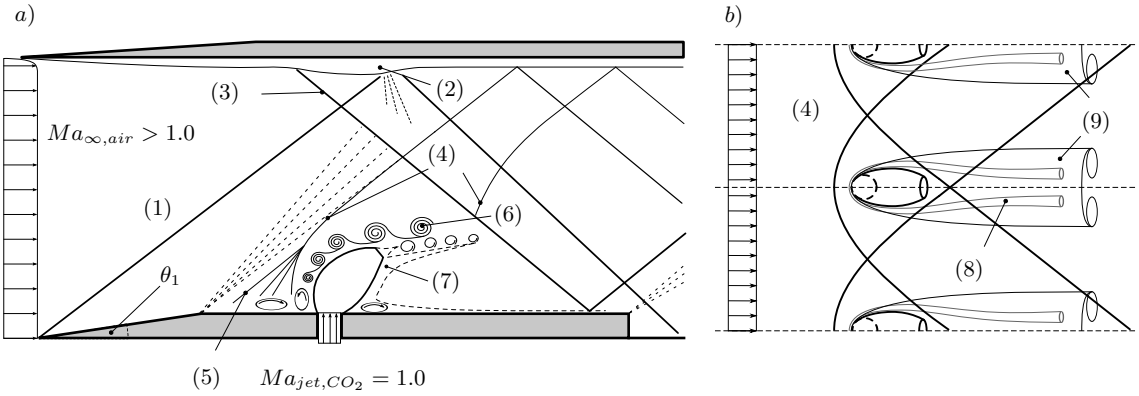

Figure 5.2: Sketch of a jet in supersonic cross-flow on the topside of a strut injector inside a channel from the side a) and top b).

exit velocity of the jet. This velocity difference and perturbations inside the upstream recirculation trigger a Kelvin-Helmholtz instability directly at the nozzle, which leads to periodic vortex formation further downstream. This roll up in the mixing layer has mainly two effects: First, it entrains fluid from both streams and through that increases the area of the interface between them. Second, it steepens the local concentration gradient. The enlarged interface and concentration gradients enhance the molecular mixing of the two fluids. With a higher convective velocity the shear rate between the two fluids increases. This generally leads to faster roll-up and fluid entrainment, and in consequence, to faster mixing. Turbulence causes an increase in viscous dissipation of kinetic energy to thermal energy and irreversible entropy increase accompanied by usually undesired total-pressure losses.

Compressibility effects counteract, to some extend, the faster mixing caused by the stronger roll up and faster shear layer growth rate. For jet in supersonic crossflow configurations the transition from near-field to far-field mixing occurs 10 to 20 jet diameters [37] downstream of the injection.

5.2 Flow conditions

The strut injector model in the experimental test rig, from which the setup of this simulation has been derived, has seven perpendicular injection holes on its upper side with a diameter of $D = 0.4mm$ each. The step at the strut base measures $L_b = 1mm$ and the struts streamwise length is $L_s = 23mm$. The wedge angle at the leading edge is $\theta_1 = 7°$. The chamber measures $H = 25mm$ in height and $B = 27mm$ in spanwise direction. The distance between two injection holes is $D_i = 3.2mm$.

The undisturbed air free-stream has a Mach number of $Ma_\infty = 1.906$, a static temperature of $T_\infty = 167.96K$ and a static pressure of $p_\infty = 100541.44Pa$. The molar concentrations of oxygen and nitrogen in the oncoming air are $x_{O2} = 0.21$ and $x_{N2} = 0.79$.

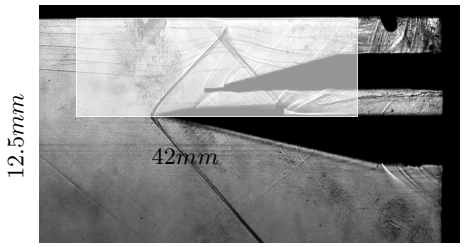

Figure 5.3: Schlieren picture taken from the side of the experiment together with a highlighted area which indicates the simulated section.

The jet gas is pure carbon dioxide. The jet has a total pressure at the nozzle inlet of $p_{jet,0} = 1.5 \cdot 10^6 Pa$ and a total temperature of $T_{jet,0} = 293K$, which yields a jet to crossflow momentum ratio of

$$J = \frac{\rho_{je} u_{jet}^2}{\rho_{CF} u_{CF}^2} = \frac{p_{jet}}{p_{CF}} \approx 2.1. \tag{5.1}$$

5.3 Numerical setup

For the numerical simulation, a periodic slice containing a single injection hole is considered. A sideview of the simulated section of the experiment is highlighted in Fig. 5.3. In spanwise direction periodic boundaries are chosen to capture effects of neighboring injections. Adiabatic no-slip wall boundary conditions are imposed at the strut injector, the injection nozzle and the channel wall at the top. At the injection nozzle inlet the total pressure and temperature are prescribed. At the channel inlet, a supersonic inflow condition is specified and at the outflow a Neumann boundary condition is used for all quantities. Turbulent inflow data for the boundary layer at the upper channel wall is generated by a digital filter technique [16]. This technique applies artificial fluctuations on the three velocity components in such a way that the velocity field reproduces prescribed first and second order one point statistics [16]. From these velocity fluctuations density and temperature fluctuations are calculated employing the strong Reynolds analogy. The thickness of the boundary layer imposed by the digital filter boundary condition is required as an input at the start of the simulation. It has to be adjusted in such a way that it creates the correct size of the separation at the impingement point of the leading-edge shock. Since it was impossible to accurately measure the boundary layer thickness in the experiment, the thickness was estimated based on diagram 7 in Dupont et al. [5]. There, the linear dependency

$$\frac{L}{\delta_0} \sim \frac{\Delta p}{2\tau_w} \tag{5.2}$$

is plotted where L is the interaction length, δ_0 the boundary layer thickness directly in front of the interaction, Δp the pressure rise across the shock system and τ_w the wall shear stress at the same location δ_0 is taken. The interaction length was determined from

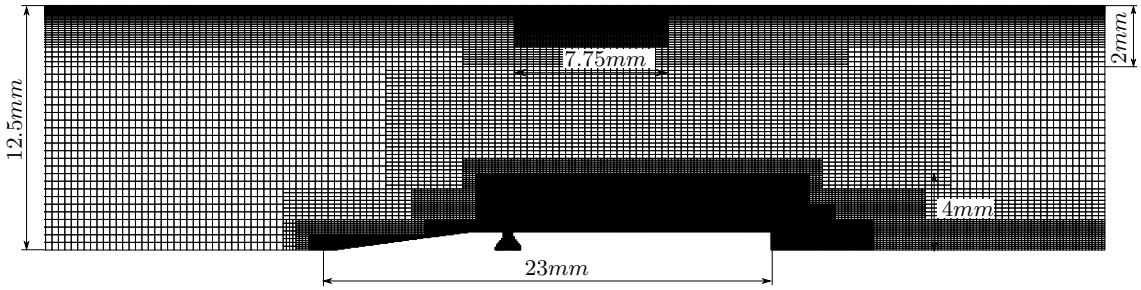

Figure 5.4: Section of the computational grid used for the simulation, showing every 5th cell on a $z/D = 0.0$ plane. The measures display the resolved parts.

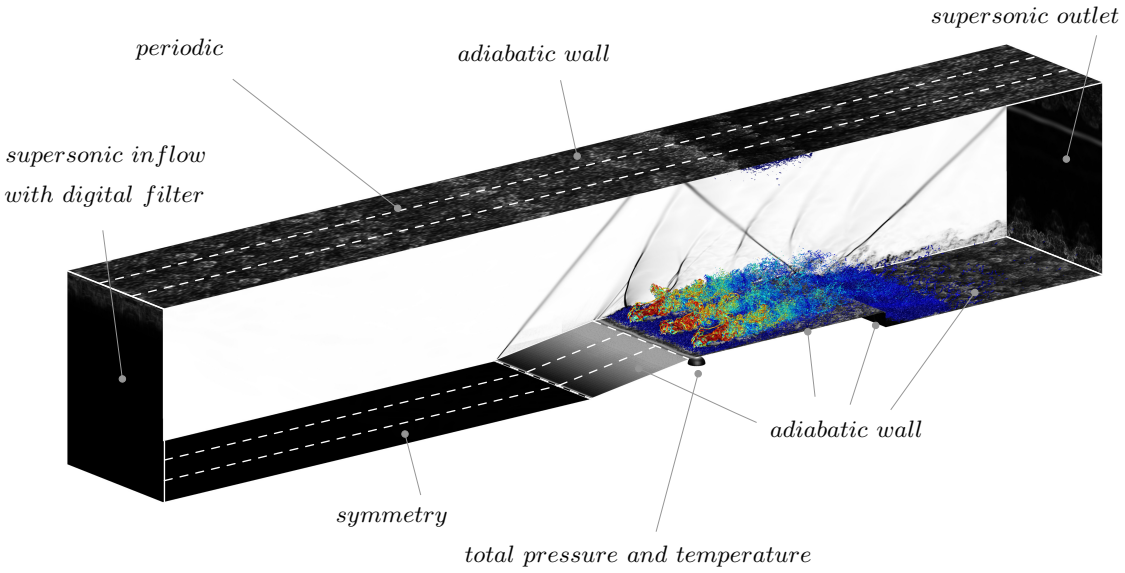

Figure 5.5: Overview of the computational domain (displayed including an exemplary result dataset) with applied boundary conditions and two mirrored domains.

the experimental schlieren picture, the pressure rise can be calculated analytically, and the wall shear stress was taken from a separate temporal boundary layer simulation. The final estimate is $\delta_0 = 1.4mm$. The computational grid, see Fig. 5.4, has a total number of 95 million cells and employs an adaptive mesh refinement (AMR) strategy with hanging nodes to accommodate the different resolution requirements of the boundary-layer flow and the jet mixing region. A fully conservative immersed boundary technique, based on a cutcell approach described by Meyer et al. [22, 23] and extended by Örley et al. [25], is employed to represent the strut injector and the jet injection nozzle on the Cartesian grid. The boundary conditions are summarized in Fig. 5.5, which displays the domain that has been simulated together with two mirrored datasets. The simulation domain measures $L_x = 42mm$ in streamwise, $L_y = 12.5mm$ in vertical and $L_z = 3.2mm$ in spanwise direction. The injection hole has a diameter of $D = 0.4mm$ and the wedge of the strut injector deflects the supersonic flow by 7 degrees.

Data for a statistical analysis has been collected for approximately three flow through

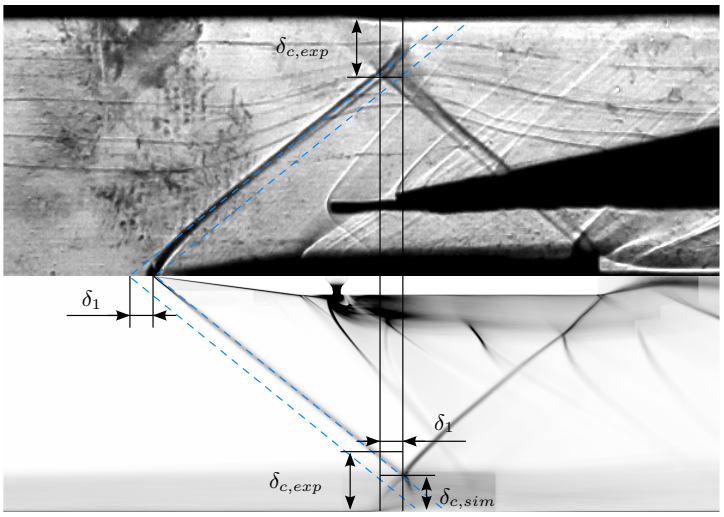

Figure 5.6: Comparison of an experimental Schlieren picture to a numerical slice displaying the time-averaged density gradient magnitude.

times, based on the freestream velocity and the full domain length.

5.4 Comparison to experimental data

Figure 5.6 shows a schlieren picture from the experiment and a density gradient magnitude plot from the simulation. This visualization demonstrates that the overall flow field and shock system are represented accurately in our simulation. The characteristic of the shock system and shock boundary layer interaction (SBLI) are captured very well. A horizontal offset δ_1 of the shock position is visible and is caused by a slightly curved shock in the experiment, while the shock in the simulation is straight. The curvature may be explained by a combination of leading edge bluntness and three dimensional effects due to the sidewall windows. The influence of the wall is nicely visualized by small droplets, which are on the window inside the channel and create a trace in the shape of surface streamlines. These lines start to bend upwards at a relatively large distance upstream of the shockwave. It is concluded that the interaction of shockwave and sidewall boundary layer leads to a certain upstream effect, similar to the SBLI at the top wall, that cannot be reproduced in the current numerical setup.

A second small difference is the distance between the wall and the location where the incoming and reflected shock intersect. This may be due to not identical boundary layer thicknesses in the simulation and the experiment. A second possible reason is that the simulation assumes a fully turbulent boundary layer, which can be neither confirmed nor denied based on the available experimental data. The assumption of a fully turbulent boundary layer (TBL) has an effect on the wall pressure as well. A TBL can sustain a larger adverse pressure gradient than a laminar one or a boundary layer that is undergoing transition. Figure 5.7 displays the simulated wall pressure together with with experimental

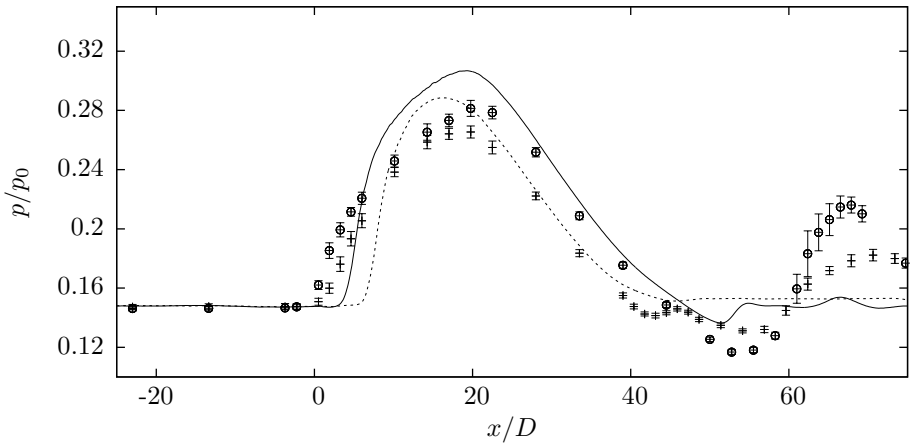

Figure 5.7: Wall pressure at the channel wall. Circles: experiment including injection; crosses: experiment without injection. Error bars indicate the standard deviation. Solid lines: Simulation including injection; dashed line: simulation without injection.

data. Simulation and experiment were conducted with and without injection, both cases are shown in the figure. For each data point in the experiments, several measurements were conducted and the average is plotted. The standard deviation of these measurements is displayed as error bars. The figure shows a slight upstream shift of the start of the pressure rise. This rise is due to the separation caused by the impinging shock wave. The pressure maximum is slightly higher in the simulation for both, with injection and without injection, but still less than the analytical value. The second peak in the experiment is caused by the second reflection of the leading edge shock. It impinges on the strut after being reflected at the top channel wall. Since the recirculation in the simulation is smaller and the shock position is slightly shifted downstream, this second reflection is not present in the simulation. Here the reflected shock misses the strut and enters the wake of the strut at its trailing edge. The experiment shows a large standard deviation in the measurements in the region of the second peak which indicates an unsteady oscillating shock. The case of no injection follows the same trend in experiment and the simulation as they both show a lower maximum of the pressure peak. The lower maximum is due to the missing shock of the injection in the case of no injection. A second similar trend is the longer region of the pressure remaining at its free-stream value in front of the pressure rise if there is no injection. A comparative schlieren image of the injection turned on and off is given in Fig. 5.8. The differences to the main shock structure are highlighted by blue circles. In addition, the periodic appearance of the injection's bowshocks is visible in the plot.

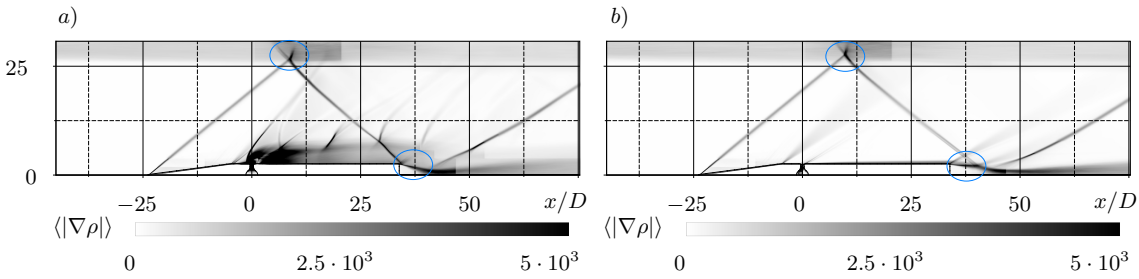

Figure 5.8: Time averaged density gradient magnitude on a $z/D = 0$ slice with injection a) and with no injection b).

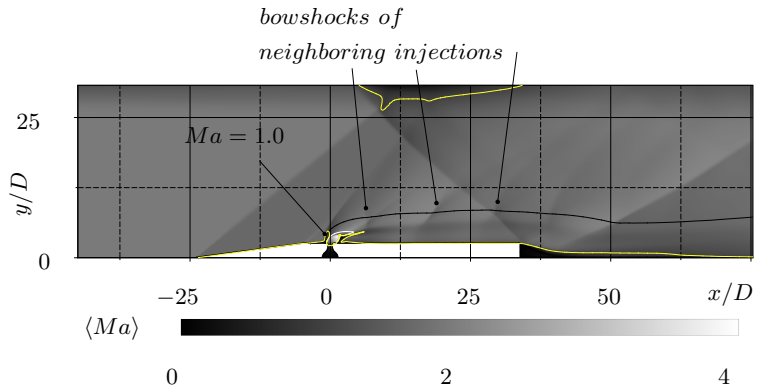

Figure 5.9: Time averaged Mach number on a 2-D slice through the center of the simulated injection.

5.5 Additional numerical investigations

5.5.1 Mach number and density gradient

In the following section numerical results without comparison to the experiment are analyzed as the considered quantities are not measurable in the given experimental setup. First the Mach number is considered. In Fig. 5.9 the time averaged Mach number and iso lines of 5% and 95% massfraction of CO_2 are shown in black and white respectively. The yellow line is the sonic line. Three main regions where the Mach number is subsonic are visible. The largest one is the recirculation on the top wall due to the impinging shock waves from the struts leading edge and injection. Both shocks cause a small spike extending into the core flow, clearly indicating the locations where the shocks impinge. The second subsonic region is located at the rear end of the strut which resembles a backward facing step configuration. The reflected shock, which enters the recirculation exactly at the struts base, causes an additional thickening of the boundary layer. The third subsonic region is located at the injector. This region is divided in two parts, one following the normal part of the bow shock and extending a short distance upstream in the separated boundary layer, and a second one at the downstream side of the injected jet including a small region caused by the Mach disk.

The Mach number plot, Fig. 5.9, visualizes the complex shock pattern. The leading

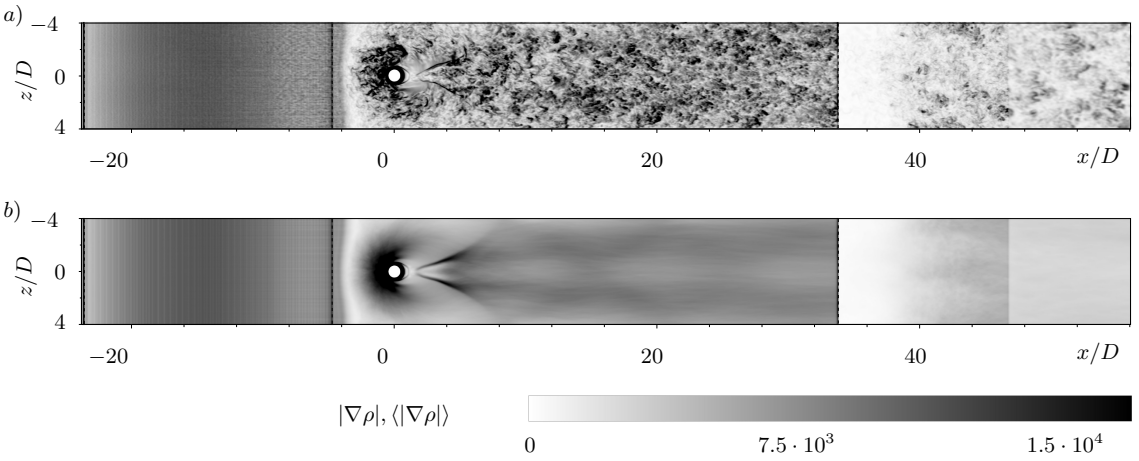

Figure 5.10: Instantaneous a) and time averaged b) density gradient magnitude on the strut's wall.

edge shock and the recompression shock following the recirculation at the struts base are most pronounced. Also visible is the bowshock in front of the jet and the bowshocks from neighboring injections, which cross the center plane. These shocks are much weaker than the ones originating from the injector itself.

Figure 5.10 shows the instantaneous (top) and time averaged (bottom) magnitude of the density gradient on the struts wall. The signature of the bowshock in front of the injection is clearly visible in both plots. The footprint of the two shocks at the downstream side resulting from a recompression after the fluid flows around the jet are clearly visible as well. In the instantaneous figure these two shocks are asymmetrical because they move left and right with a frequency depending on the Reynolds number. This wall near situation is comparable to the flow around a cylinder. The instantaneous plot reveals that turbulence starts to develop in front of the injector's shoulder on the sloped wall. The change in contour level and size of resolved structures in the figure at $\approx 46.5D$ results from a change in grid resolution.

A more detailed view on the bow shocks in the jet wake, is plotted in Fig. 5.11. The figure shows the time averaged density gradient magnitude on a slice $5D$ above the strut's surface. In the figure the three large shocks originating from the strut are present as well: The shock caused by the struts leading edge (1); its reflection from the top wall (2); the re-compression shock following the recirculation at the strut's base (3). The bowshocks caused by each injection can be seen downstream of the injection holes due to the elevated position of the slice. As they hit the domain's periodic boundary condition (dashed horizontal lines), they reenter the domain on the opposite side, creating the same shock pattern as a simulation in a domain containing several injections would. After each shock intersection, the Mach number reduces and the shock strength weakens. Because of the lowered Mach number the shock angle becomes steeper, which can be seen by comparing the length measures (a), (b) and (c). Inside the encircled area (I) an additional

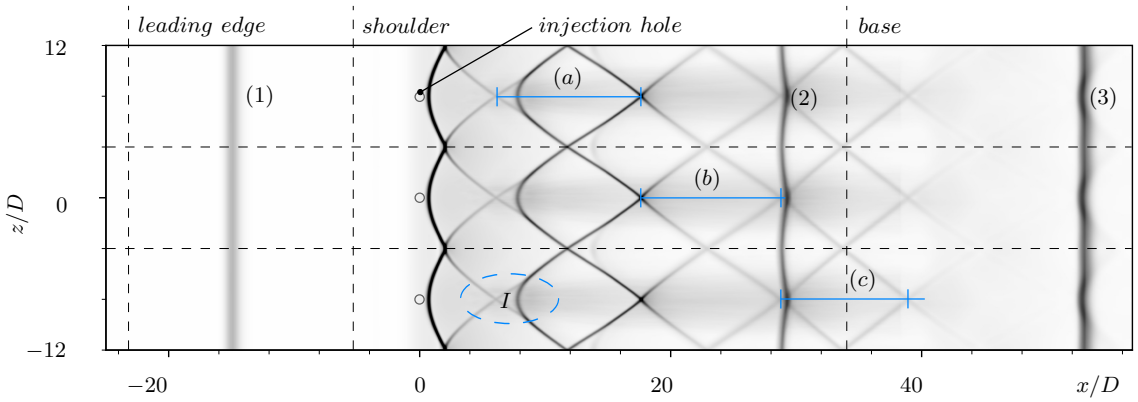

Figure 5.11: Time averaged density gradient magnitude on three domain instances to visualize the mixing zone shock pattern on a slice $5D$ above the strut's surface.

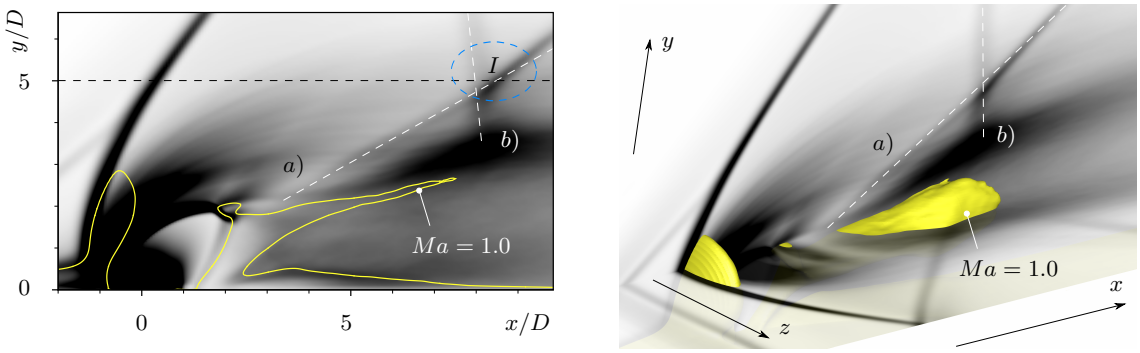

Figure 5.12: Density gradient magnitude, displaying details of the shock structure around the injection on a central plane on the left and three dimensional on the right. Shock a) originates from the subsonic region enclosed by the yellow line/isosurface and shock b) is the neighbor injection's bow shock.

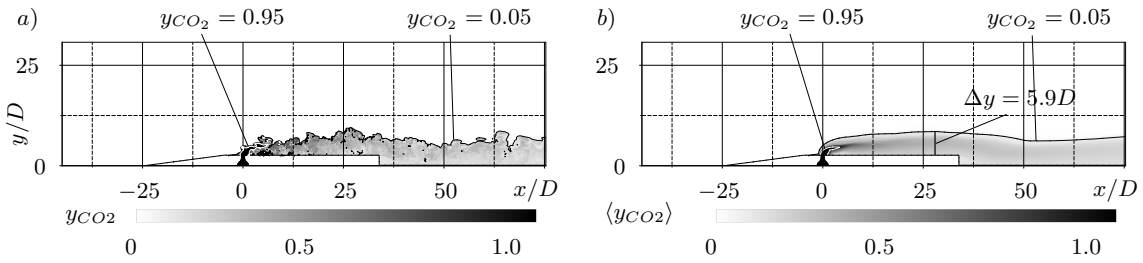

Figure 5.13: a) Instantaneous and b) time averaged CO_2 mass fraction on a 2-D slice through the center of the simulated injection.

bow shaped shock is visible. The same area is encircled in the left sketch of Fig. 5.12. It is apparent that the additional bowshock is shock (a) and shock (b) is the bowshock from the next injection. The additional bowshock originates from the subsonic region which is marked by the yellow line and isosurface in Fig. 5.12. The formation of this additional bow shock is case dependent as e.g. in the previous study of a Mach 1.6 air JISC this shock was not present. The horizontal black dashed line marks the location of the slice displayed in Fig. 5.11.

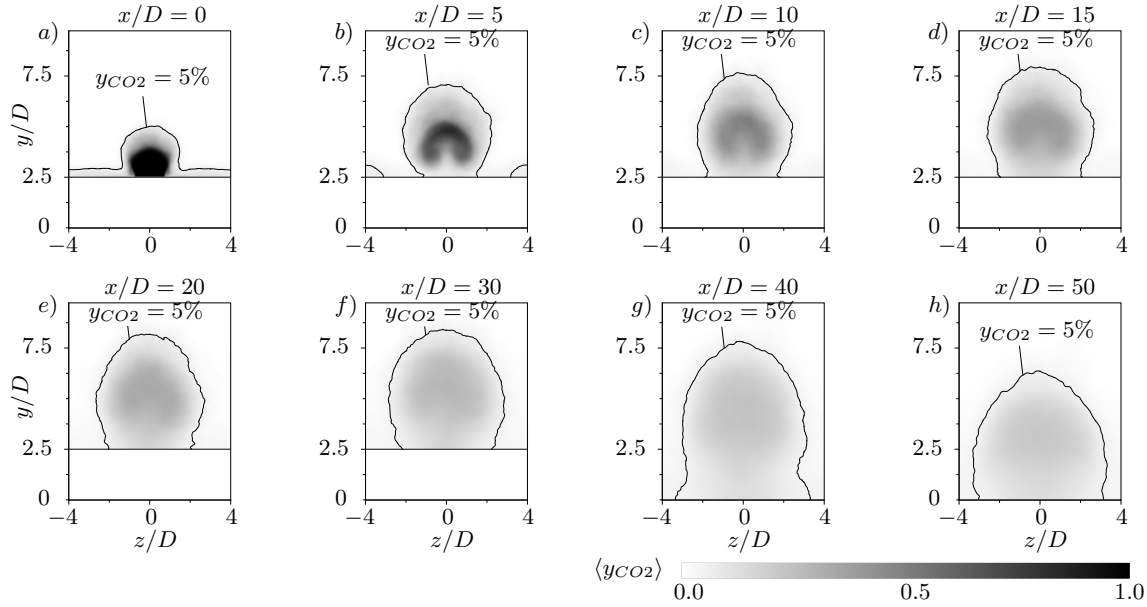

Figure 5.14: Time averaged CO_2 massfraction on x-constant slices. Stations g) and h) are located downstream of the injector.

5.5.2 Turbulent mixing

Shock waves passing through the turbulent mixing zone of the injections influence the mixing process: when turbulence is convected through a shock wave, the shock wave structure and turbulence properties are altered in a mutual process, which is termed shock-turbulence-interaction (STI). The convection entropy perturbations through a shock results in baroclinic vorticity production and generates additional acoustic waves. Velocity fluctuations are anisotropically amplified across the interaction and turbulent structures are compressed in shock-normal direction. The shock itself is wrinkled by perturbations of the incoming flow. Both processes affect the mixing of the jet fluid and surrounding air.

To evaluate the mixing of the jet fluid with the crossflow, the mass fraction of CO_2 is analyzed. Figure 5.13 shows an instantaneous (left) and a time averaged (right) plot of the CO_2 mass fraction. Highlighted are iso-lines of 5% and 95% of the CO_2 mass fraction. It can be seen that the 95% line encloses only a small region downstream of the injection. This indicates fast break up of the jet and strong turbulent mixing with the supersonic crossflow. The time average of the mass fraction indicates a penetration depth of the jet of $\approx 5.9D$ at the trailing edge of the strut if the penetration depth is defined as the 5% border of y_{CO2}. Approximately at $x = 27D$, the streamlines are turned downwards by the reflected shock from the top wall and by the expansion fan originating from the trailing edge of the strut. This downward deflection is clearly visible in the CO_2 massfraction contour plot, Fig 5.13. The re-compression shock originating from the end of the recirculation region behind the strut stops the downward motion of the CO_2.

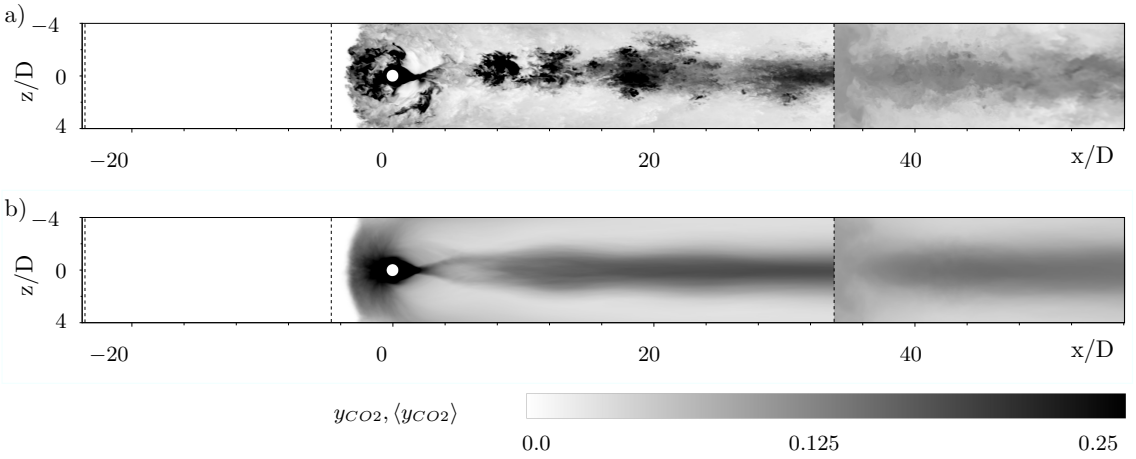

Figure 5.15: Instantaneous a) and time averaged b) CO_2 massfraction on the strut's wall.

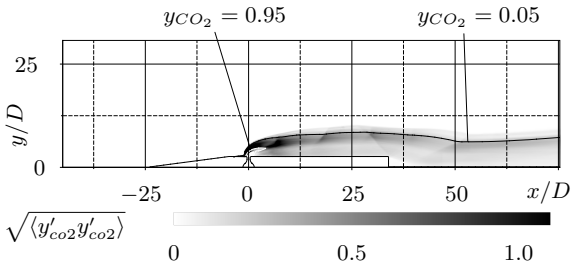

Figure 5.16: Root mean square of the CO_2 massfraction on a slice through the center of the simulated injection.

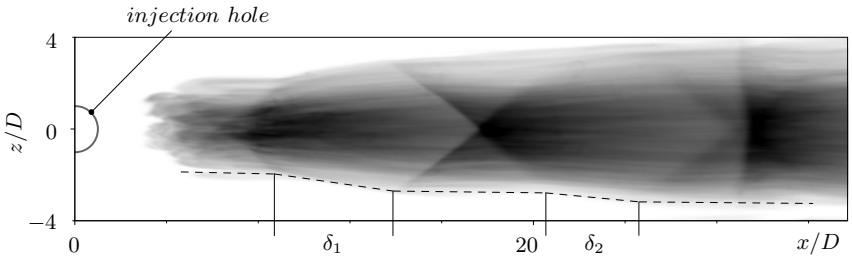

Figure 5.17: Root mean square of the CO_2 massfraction on a slice $5D$ above the strut's surface.

The vertical and horizontal distribution of CO_2 is further evaluated in Fig. 5.14. Most of the CO_2 is located inside the barrel shock of the jet directly at the injection a). A short distance further downstream the injected gas leaves the barrel shock area and is entrapped in the large vortex pair that has formed around the jet, see b), c) and d) in Fig. 5.14. This resembles the near-field mixing zone explained previously. All stations further downstream (e) and following exhibit far field mixing properties, where the vortices disappear and the CO_2 is distributed increasingly homogeneous across the cross section of the jet. Nevertheless the horizontal mixing between neighboring jets is not sufficient to evenly distribute the injected gas across the domain. Even at $x/D = 50$ the 5% isoline has not reached the center between two injections.

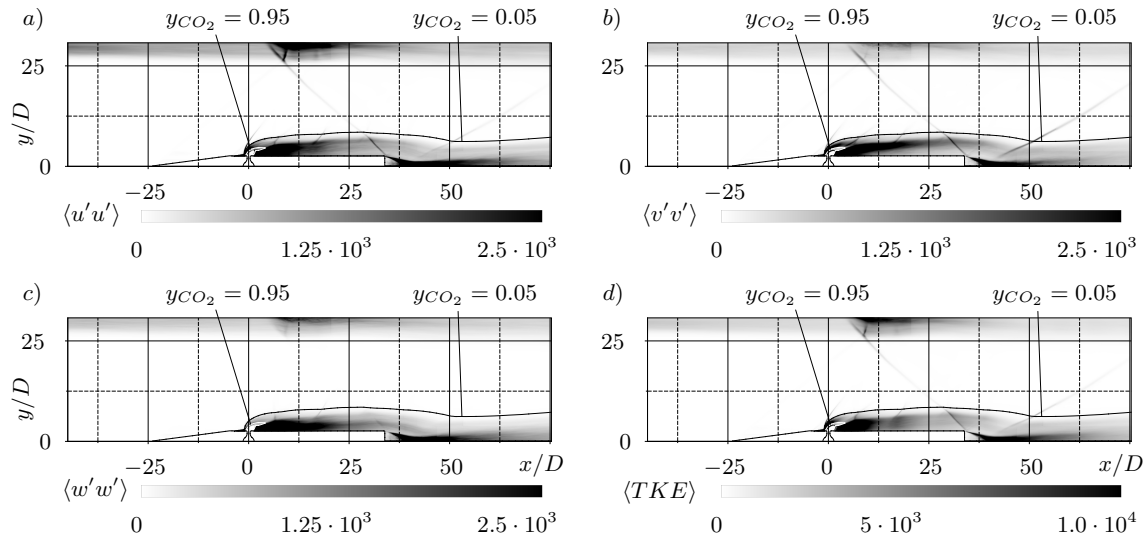

Figure 5.18: Time averaged turbulent transport in all three directions on a 2-D slice through the center of the simulated injection.

The time averaged and instantaneous distribution of the CO_2 concentration at the wall is shown in Fig. 5.15. It can be seen that the jet fluid quickly spreads in spanwise direction over the entire domain. Further downstream, the time average shows a clear trace of the injected gas in the middle of the domain.

At $x \approx 6D$ a slight upwards bend is recognized in the 5% isoline. This is the influence of the bow shock of the neighboring injection, which causes an upward motion of the CO_2. Additionally, the bow shocks of neighboring injections amplify the root mean square (RMS) of the CO_2 mass-fraction fluctuations, which can be seen in Fig. 5.16. The amplification factor across the shock for the first neighbor injection is ≈ 1.4. With every subsequent injection bow shock this factor is decreased by ≈ 0.1. In a similar fashion as on the wall normal slice, a great influence of the shocks on the turbulent mixing can be seen in wall parallel direction. Figure 5.17 shows a slice of the CO_2 mass-fraction at the identical $y/D = 5$ position as Fig. 5.11, in which the shock structure was discussed without taking the mixing into account. In spanwise direction however, the shocks either diverge or converge the mixing zone and the overall extension of the mixing zone is greatly increased by the shocks passing through. Each repetition of the shocks appearing in the mixing zone, or the further away the injection to which a shock "belongs" is, the smaller the effect becomes due to the already thickened mixing zone and weaker shock. This is indicated by the sloped distances at the mixing zone edge marked by δ_1 and δ_2.

Figure 5.18 shows contours of the Reynolds normal stresses and the turbulence kinetic energy. In agreement with the previous results of the RMS, the bow shocks of neighboring injections and the reflected shock from the strut's leading edge amplify the turbulence. This is especially visible in the $\langle u'u' \rangle$ and $\langle v'v' \rangle$ plots and consequently in the turbulent kinetic energy as well.

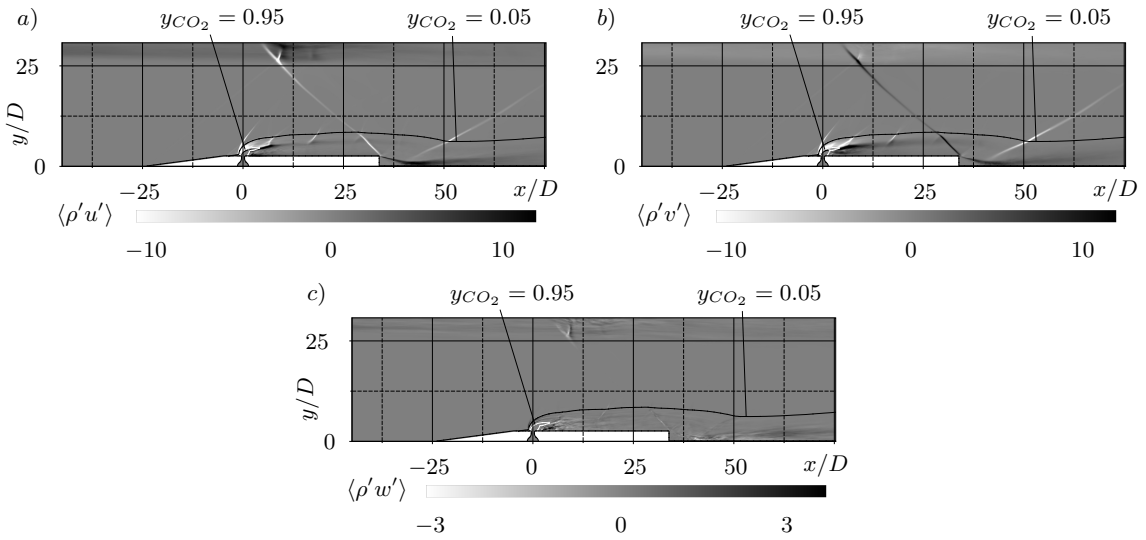

Figure 5.19: Time averaged turbulent transport in all three directions on a 2-D slice through the center of the simulated injection.

The amplification and modulation of velocity fluctuations also affect the turbulent mass transport of CO_2. The contour plots, Fig. 5.19, show the foot prints of the shock waves and the turbulent mixing zone in the wake of the jets. The turbulent mass transport of CO_2 is substantially amplified at the bow shocks of neighboring injections and the reflected leading edge shock.

Analyzing the turbulent statistics related to mass transport clearly show that the configuration of several jets in a row creates stronger turbulent mixing than a single jet.

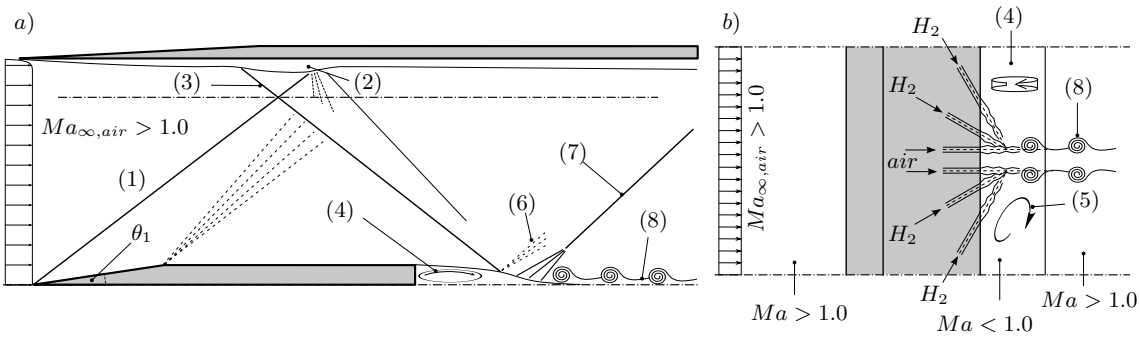

Figure 6.1: Sketch of the strut injector pilot injection flow from the side a) and top b).

6 Strut injector with pilot injection

6.1 Case description pilot injection

Depending on the flight Mach number the conditions in a supersonic combustion chamber allow for autoignition of the fuel. The governing quantity for this process is the static temperature of the gas in the mixing region. If the flight Mach number is small, the temperature in the combustion chamber is also low, and not sufficient to ignite the fuel. Another scenario where autoignition may not be possible, depending on the setup, are ground experiments. The test bench with the investigated strut injector, Chapter 5, is a cold flow replica of a larger experiment including hydrogen combustion. The experimental setup uses preheated air to enable supersonic combustion, however the achieved temperature is still not sufficient for autoignition. To ignite the fuel, a pilot flame is used, which is ignited with a laser pulse. Fuel and oxidizer for the pilot flame are provided by several injections from the injector base. Figure 6.1 provides an overview of the flow field. The main injection investigated in Chapter 5 is not considered here to isolate effects belonging to the two injection types. Similarly to the former investigated strut injector, a primary shock (1) is generated by the sharp leading edge of the injector. This shock causes separation of the boundary-layer (2) and a reflected shock (3) at the top wall. The reflected shock enters the recirculation region (4) following the strut's base where the shock is reflected as an expansion (6). Hydrogen and air is injected through six injectors at the base of the strut, which are oriented in a way that the three jets of one side impinge on a single point. A second, horizontal, recirculation is created by the injection jets. Following the expansion the recirculation collapses, creating a compression corner and a

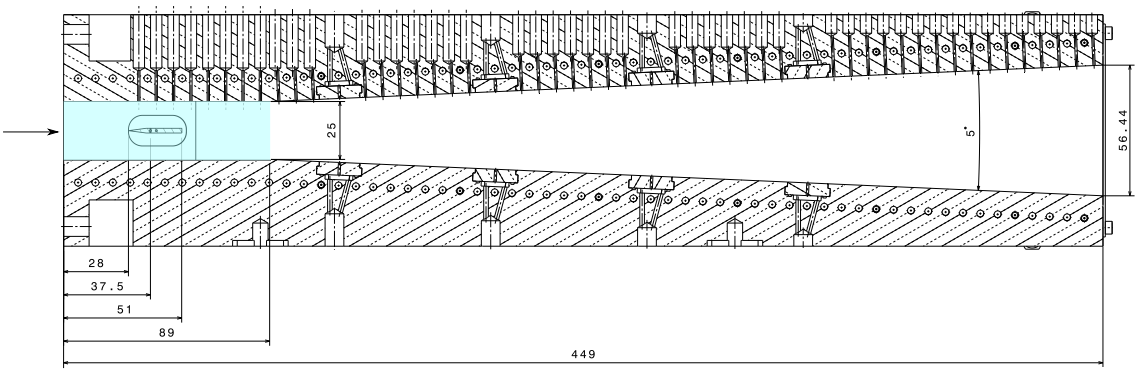

Figure 6.2: Technical sketch as provided by Fuhrmann [8] of the experimental combustion chamber downstream from the laval nozzle. Highlighted in blue is the simulated section.

re-compression shock (7). In the wake of the injector a shear- and mixing-zone is formed.

6.2 Flow conditions

The combustion chamber used in the experiment was described by Fuhrmann [8] and is sketched in Fig. 6.2. It consists of a short section with parallel walls and a strut injector located in the middle of the channel. The strut injector has identical dimensions as the one investigated in Chapter 5. Following the segment with the constant cross section, the geometry is diverging with a opening angle of 5 degrees. Fuel is injected through perpendicular nozzles on the strut injector's top and bottom. Optionally, hydrogen wall injectors in the divergent part of the chamber can be activated during operation. For the pilot injection a total of six bores at the base of the strut are used. The two middle ones are parallel to the main flow direction and inject air, the other four are sloped and impinge on the air jets to enable efficient mixing. All pilot injectors have a diameter of $D = 0.5mm$. Holes on the top wall of the chambers are use to mount sensors in order to record the wall pressure. The walls are made of copper with active water cooling to enable continuous operation without overheating of the walls. The section with parallel walls measures $L_x = 89mm$ in x-direction, $L_y = 25mm$ in y-direction and $L_z = 27mm$ z-direction.

The air flow through the combustion chamber has a Mach number of $Ma_\infty = 2.15$ with a static temperature of $T_\infty = 509.2K$. The injections have a total temperature of $T_0 = 300K$. The total pressure is calculated to match the mass flow rate measured in the experiment. These mass flows are $0.25g/s$ at both air injections and $22.5mg/s$ hydrogen through each of the four hydrogen injectors. The resulting pressure values are $p_{0,inj,air} = 5.456 \cdot 10^5 Pa$ for the air injectors and $p_{0,inj,H_2} = 1.857 \cdot 10^5 Pa$ for the hydrogen.

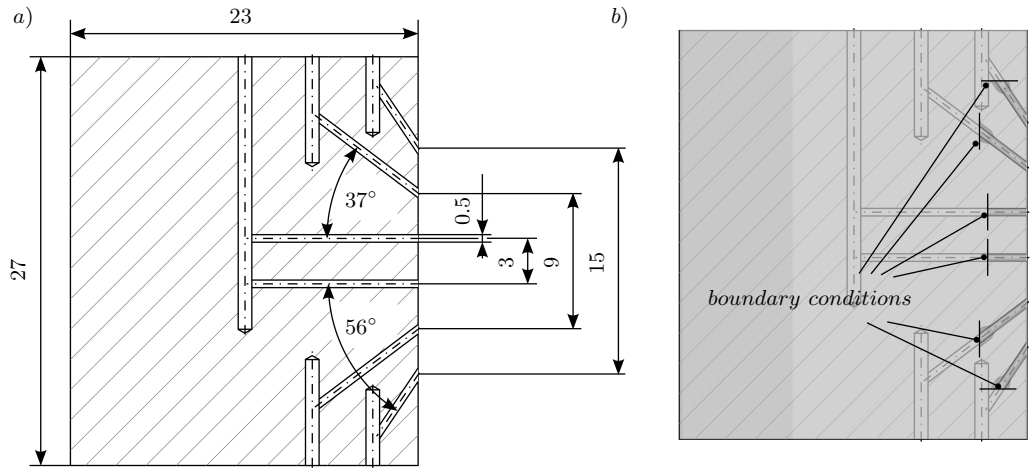

Figure 6.3: a) Technical drawing [8] of the experiments injector. b) Representation of the injector geometry for the simulation, displayed by the immersed boundary wall as an overlay over the technical drawing.

6.3 Numerical setup

The domain for the simulations in this work is highlighted in Fig. 6.2 of the combustion chamber, which is the section with parallel walls and the strut injector. The inlet and outlet boundary conditions are supersonic boundary conditions. The four side walls are modeled as symmetries, which corresponds to frictionless walls. These outer walls are not resolved to reduce computational costs and because the main focus of the study is the mixing zone in the wake of the strut. The top and bottom symmetries are placed at the shock crossing position determined in the simulations in Chapter 5 (which include a boundary layer). This is done to create a flow field with the same shock reflection location as if the simulation included the boundary-layer. The location of these symmetries have an offset of $2mm$ from the channel walls. The injector surface and injection tubes are modeled as adiabatic walls by the immersed boundary technique. Figure 6.3 displays a technical drawing of the experimental strut interior, a) as given by Fuhrmann [8], and the wall created with the immersed boundary, b), used in the simulations. The positions where injection boundary conditions are applied are pointed out as well. The boundary conditions applied for the injections is a total temperature and total pressure boundary condition.

For the calculation of the total pressure, the assumption is made, based on the Fanno flow, that the flow at the injection tube exit is critical. With this assumption and the fact that the mass flow rate has a maximum at the point of critical flow, the total pressure for the boundary condition can be calculated.

The Fanno tube flow is a one-dimensional description of a compressible adiabatic flow through a pipe with constant cross section including friction. To achieve $Ma = 1.0$ flow

at the tube exit, the first law of thermodynamics can be used in the form

$$h + \frac{1}{2}u^2 = const. \tag{6.1}$$

With the mass flow rate $\dot{m} = \rho A u$, Equation 6.1 can be written from a starting point (index 1) to an arbitrary location further downstream (no index):

$$h_1 + \frac{1}{2}\frac{1}{\rho_1^2}\left(\frac{\dot{m}_1}{A}\right)^2 = h + \frac{1}{2}\frac{1}{\rho^2}\left(\frac{\dot{m}}{A}\right)^2 \tag{6.2}$$

The density can be eliminated and the h-s functional for the Fanno curve can be derived by using the second law of thermodynamics to obtain an expression for the density in dependence of the entropy. For a perfect gas the second law of thermodynamics reads

$$ds = c_v\frac{dh}{h} - R\frac{d\rho}{\rho} \tag{6.3}$$

and integrates to

$$s - s_1 = c_v ln\frac{h}{h_1} - Rln\frac{\rho}{\rho_1}. \tag{6.4}$$

This can be reformulated to

$$\rho(h,s) = \rho_1\left(\frac{h}{h_1}\right)^{\frac{1}{\gamma-1}} \cdot e^{-\frac{s-s_1}{R}} \tag{6.5}$$

and inserted into Eq. 6.2 to obtain

$$\frac{1}{2}\frac{1}{\rho_1^2}\left(\frac{\dot{m}_1}{A}\right)^2 + h_1 = \frac{1}{2}\frac{1}{\rho_1^2}\left(\frac{h_1}{h}\right)^{\frac{2}{\gamma-1}} \cdot e^{2\frac{s-s_1}{R}}\left(\frac{\dot{m}}{A}\right)^2 + h, \tag{6.6}$$

which is a relation between the entropy and enthalpy. Equation 6.6 can not be solved for h directly. A plot however shows, that it has a maximum of entropy and an upper and a lower branch starting at the maximum, see Fig. 6.4. As the entropy can only increase, the state of the fluid in the tube can only move to the right on the curve and not move past the maximum. The top branch is for subsonic flows as the enthalpy decreases with rising entropy, and the lower branch is supersonic as it shows the opposite behavior. To determine the speed of the fluid at the entropy maximum the second law is used again with the condition $ds = 0$

$$Tds = dh - \frac{1}{\rho}dp = 0. \tag{6.7}$$

dh can be calculated from Eq. 6.2 by deriving the right hand side

$$dh = d\rho\left(\frac{\dot{m}}{A}\right)^2\frac{1}{\rho^3}, \tag{6.8}$$

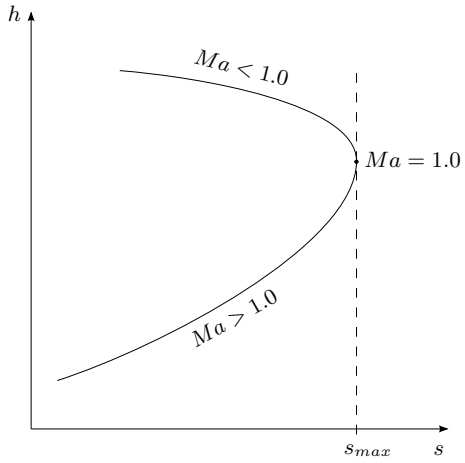

Figure 6.4: Qualitative Fanno line in the enthalpy - entropy diagram.

which then can be inserted in Eq. 6.7

$$d\rho \left(\frac{\dot{m}}{A}\right)^2 \frac{1}{\rho^3} - \frac{1}{\rho} dp = 0 \tag{6.9}$$

$$\Rightarrow \frac{dp}{d\rho} = (\rho u)^2 \frac{1}{\rho^2},\ with\ \frac{\dot{m}}{A} = \rho u. \tag{6.10}$$

This leads to the definition of the speed of sound,

$$\left.\frac{dp}{d\rho}\right|_{ds=0} = u^2 = c^2, \tag{6.11}$$

which shows that the flow reaches $Ma = 1.0$ from both branches of the curve if the tube is long enough. Assuming this is the case for the injection tubes, it is possible to derive a relation to calculate the total pressure that has to be set for a given mass flow rate. From

$$c_p T_0 = c_p T + \frac{u^2}{2} \tag{6.12}$$

the velocity is

$$u = \sqrt{2 c_p T_0 \left(1 - \frac{T}{T_0}\right)}. \tag{6.13}$$

This relation can be inserted in the massflow definition $\dot{m} = \rho A u$, and together with ideal gas and the isentropic relations leads to

$$\dot{m} = A \sqrt{2 p_0 T_0 \frac{\gamma}{\gamma - 1} \left(\left(\frac{p}{p_0}\right)^{\frac{2}{\gamma}} - \left(\frac{p}{p_0}\right)^{\frac{\gamma+1}{\gamma}}\right)}. \tag{6.14}$$

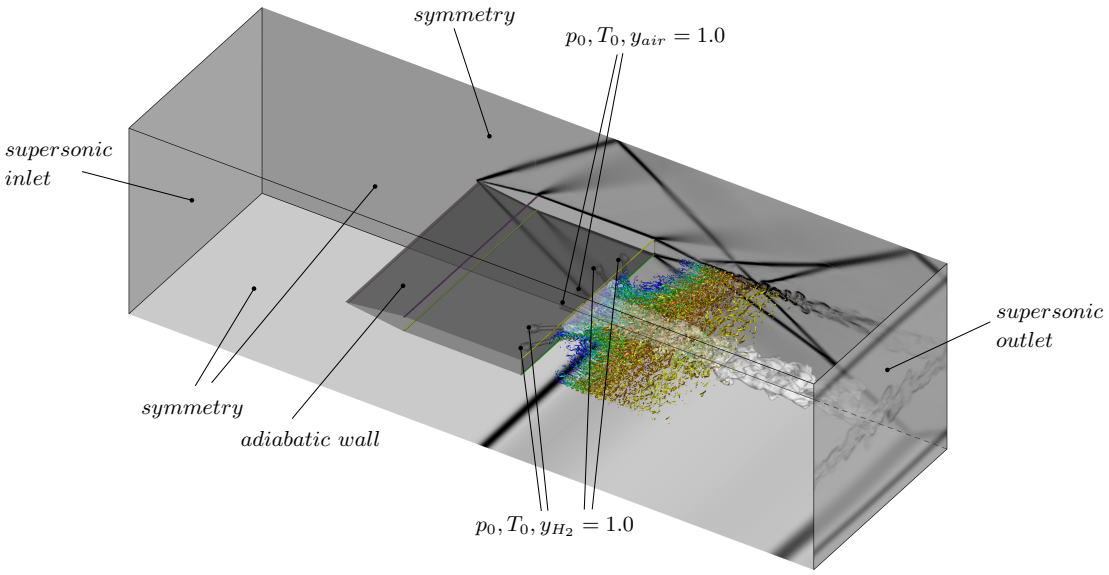

Figure 6.5: Overview of the computational domain (including visualization of the flow) with applied boundary conditions.

For the special condition of the Mach number being exactly one Eq. 6.14 reduces to

$$\dot{m} = A\sqrt{2p_0T_0}\left(\frac{2}{\gamma+1}\right)^{\frac{1}{\gamma-1}} \cdot \sqrt{\frac{\gamma}{\gamma-1}}, \tag{6.15}$$

which allows the calculation of the total pressure for the boundary conditions from known values:

$$p_0 = \frac{\dot{m}}{A} \cdot \left(\left(\frac{2}{\gamma+1}\right)^{\frac{1}{\gamma-1}} \cdot \sqrt{\frac{\gamma}{\gamma-1}}\right)^{-1} \cdot \sqrt{\frac{RT_0}{2}}. \tag{6.16}$$

This relation only depends on the gas, the total temperature of the gas, the mass flow rate and the geometry of the tube.

A summary of all boundary conditions used in this simulation is provided by Fig. 6.5.

The computational grid for this simulation consists of a total of 42 million cells with refinements around the injector wall on the outside and on the inside of the injection tubes. To capture the mixing zone, the wake of the strut is refined as well over a distance of 19*mm* which is almost one injector length. The grid has a homogeneous point distribution in z-direction. A version of the grid with reduced cell count, only on fifth of the cells, is displayed in Fig. 6.6.

6.4 Numerical results

At first, the overall flow field around the strut injector is investigated. Figure 6.7 displays the instantaneous density gradient magnitude on a slice normal to the z-axis at a location

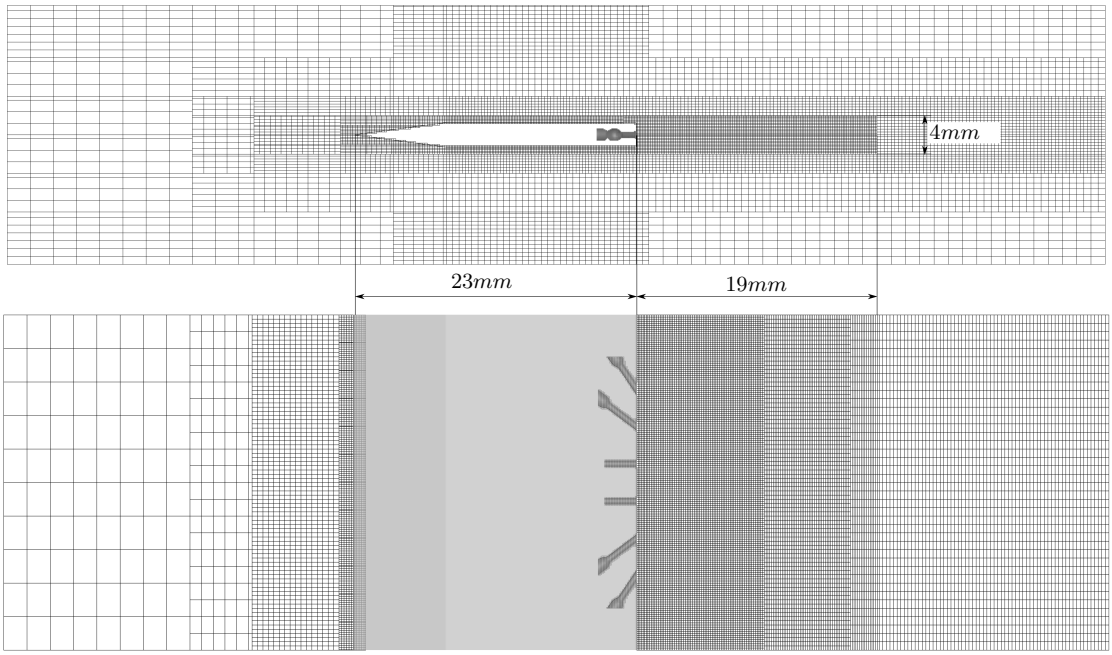

Figure 6.6: Computational grid used for the simulation, displaying every 5th cell on a $z = 0.0$ (top) and a $y = 0.0$ (bottom) plane and an overlay of the immersed boundary.

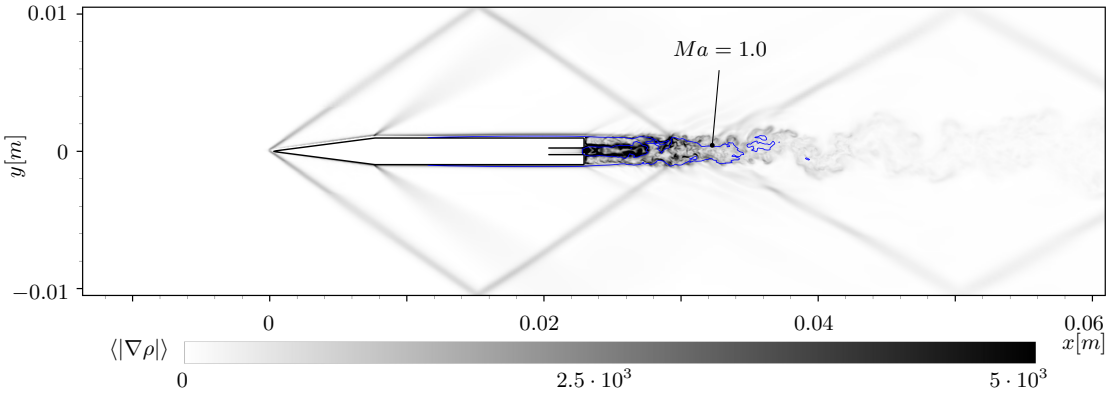

Figure 6.7: Instantaneous density gradient magnitude on a $z = -0.0015m$ slice. This position cuts through one air injection at its center.

$z = -0.0015m$, which is the center of one of the air injections. The primary shocks from the injector leading edge are reflected at the top and bottom symmetries. They enter the recirculation region and increase the size of the subsonic region behind the injector base. From the base the injected supersonic air jet is visible, which enters the recirculation. Following the recirculation re-compression shocks are visible, as well as an unsteady, periodic shedding along the direction of the y-axis. The sonic line is added in Figs. 6.7, 6.8 and 6.9 to visualize the supersonic character of the injection jets and the region where the main flow re-accelerates to supersonic speed. Figure 6.8 displays a slice through the center of the strut at $y = 0$. The figure contains a graphical representation of the strut injector

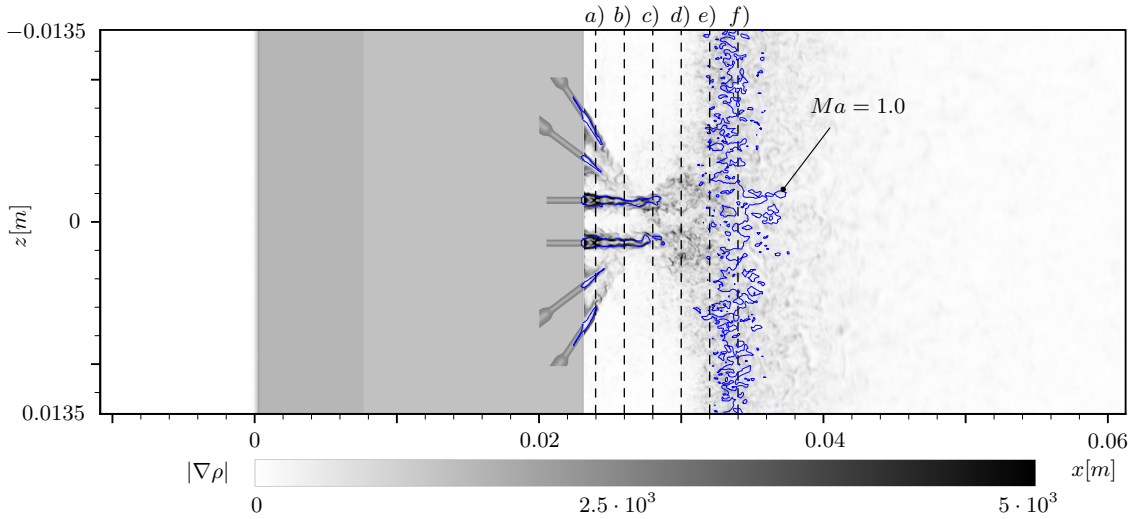

Figure 6.8: Instantaneous density gradient magnitude on a $y = 0m$ slice including a $Ma = 1.0$ line and a geometric representation of the strut. Positions a) through f) mark the positions of slices in Figs. 6.9, 6.15.

walls. Positions $a)$ through $f)$ mark the slice positions plotted in Fig. 6.9. The six injected jets and their supersonic region are clearly visible, with the two outer ones on each side impinging on the central jets. This creates a very efficient mixing region with strong turbulence within the subsonic recirculation behind the strut. The region $x \approx 0.034m$ indicates the re-acceleration to supersonic speed with presence of strong turbulence. The turbulence originates from the borders of the recirculation region, which collapses in this region. The same is visible in the plots of instantaneous density gradient magnitude on the right hand side of Fig. 6.9. Close to the strut the degree of turbulence is low and increases with larger distance. The inner part around the jets is also turbulent near the injector, as they enter the recirculation with high speeds. Turbulence is further enhanced by the interaction of the hydrogen jets with the air jets. In plot $c)$ the incoming shock from the top channel wall is visible and in plot $f)$ the re-compression shock, both as a horizontal dark bar. The air jets have the longest supersonic core in the center, as they become subsonic only shortly before the main flow re-accelerates to supersonic speed. As the injected mass has to be accelerated in addition to the main flow, the subsonic region behind the air jets has the largest extend in x-direction as can be seen in the bottom left plot of Fig. 6.9. This figure also shows that due to the added mass the recirculation region in the wake becomes thicker in y-direction in the center of the flow.

The highest Mach number in the entire flow field is reached in the core of the air jets. Even thought, the absolute velocity in the hydrogen is higher due to the high speed of sound of hydrogen, the Mach number there is lower than in the air jets. The maximum Mach number in the air jets is around 2.65 and 1.4 in the hydrogen jets, as can be seen in Fig. 6.10. The sonic line in the same figure also stretches downstream in x-direction following the air jets confirming the previous observation.

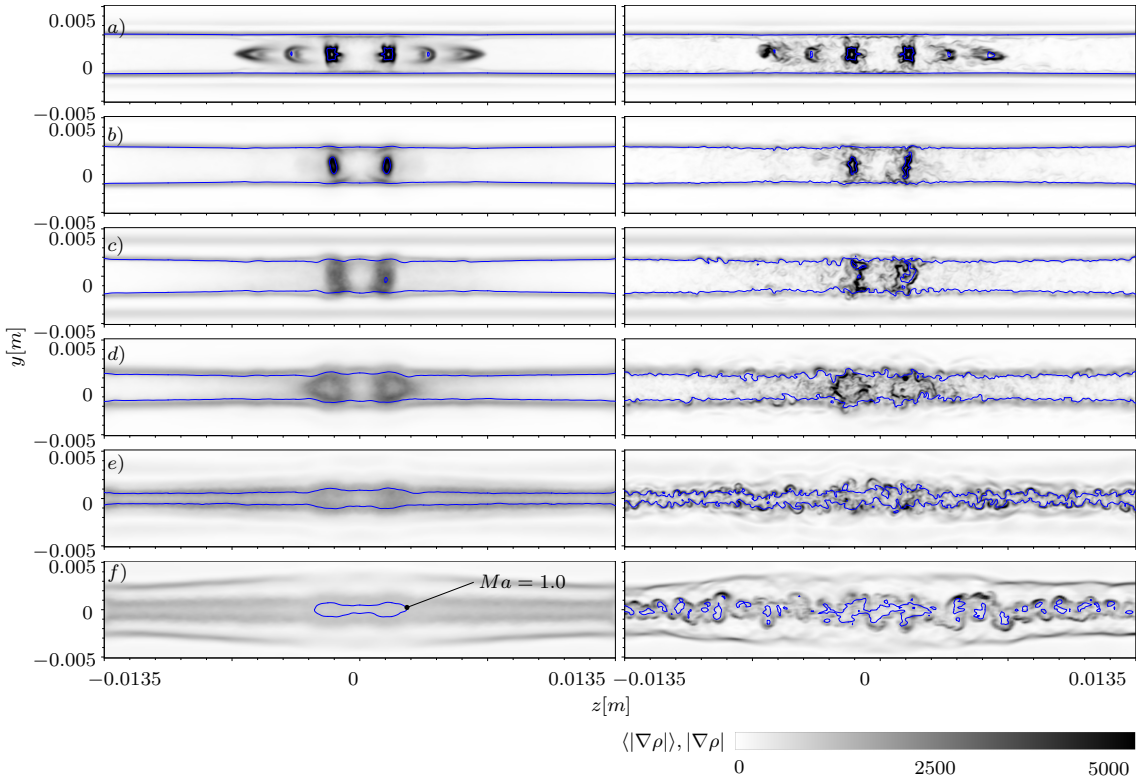

Figure 6.9: Time averaged (left) and instantaneous (right) plots of the density gradient magnitude on slices with constant x-coordinate including a $Ma = 1.0$ line. The locations of the individual slices are marked in Fig. 6.8.

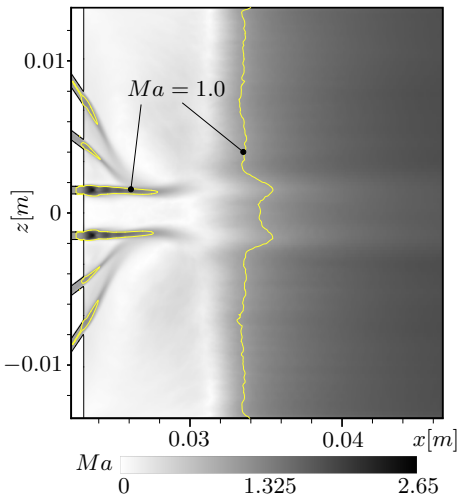

Figure 6.10: Mach number on a $y = 0m$ slice in the wake of the strut including a $Ma = 1.0$ line.

To analyze the mixing behavior of the injector, first the velocity variance in the three directions, see Fig. 6.11, and turbulence kinetic energy, see Fig. 6.12, are analyzed. They are displayed in the figures on a slice at $y = 0m$. These quantities show the edges of the injected jets to be the most turbulent part in the close wake of the injector. The air jets have the strongest variance in u due to the x-axis parallel injection, see Fig. 6.11 a). Accord-

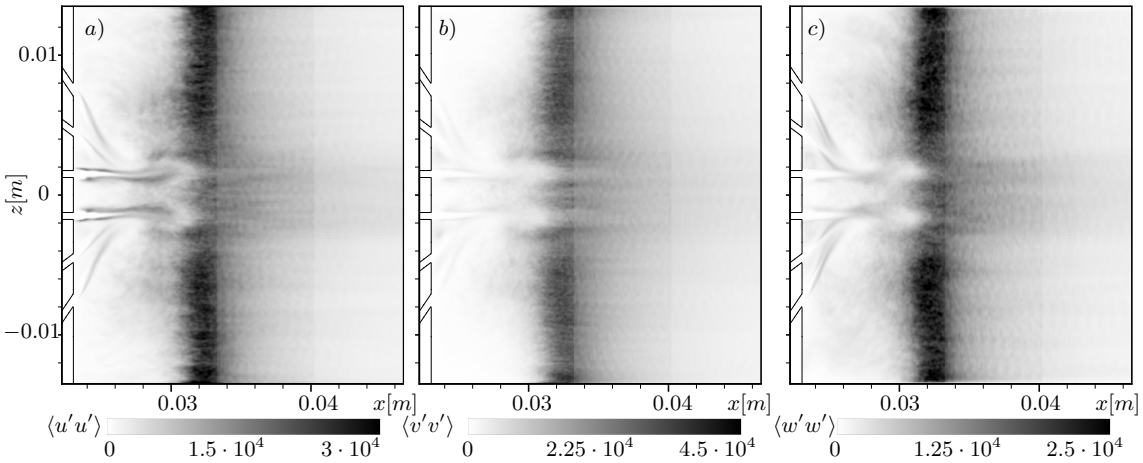

Figure 6.11: Variance of the velocity fluctuations a) $\langle u'u' \rangle$, b) $\langle v'v' \rangle$ and c) $\langle w'w' \rangle$ in all three directions on a $y = 0m$ slice.

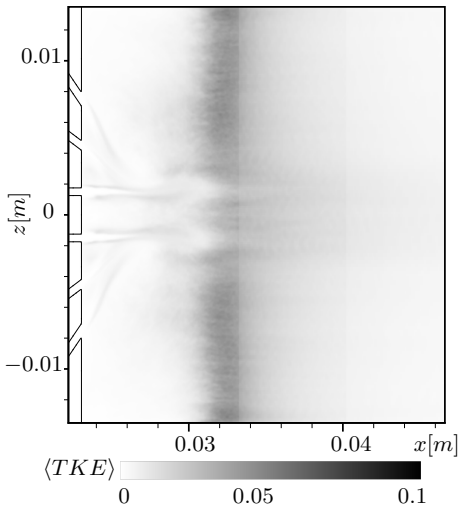

Figure 6.12: Turbulence kinetic energy on a $y = 0m$ slice.

ingly the outer hydrogen jets create the largest fluctuations in w due to their large angle, see Fig. 6.11 a). The largest turbulence intensity on the slice, however, is visible a short distance downstream, where the flow re-accelerates to supersonic speed. This is again the region where the turbulence from the upper and lower border of the recirculation merge in the center of the flow. The shockwaves from the channel walls hit the recirculation upstream of the maximum of turbulence an its trace can not be seen on the center slice.

The last of the turbulence statistic quantities considered here is the turbulent mass transport in the three directions, Fig. 6.13. It visualizes the mass transported by turbulence independent of the massfractions of the mixing species. Again, the largest values of turbulent transport are visible in the x-direction a) and z-direction c). As expected, the vertical transport is the smallest on the symmetry plane. In contrast to the variances discussed earlier, the region of highest turbulence is less pronounced in the turbulent transport. The regions with the strongest transport are the borders of the air jets, and the outer borders of

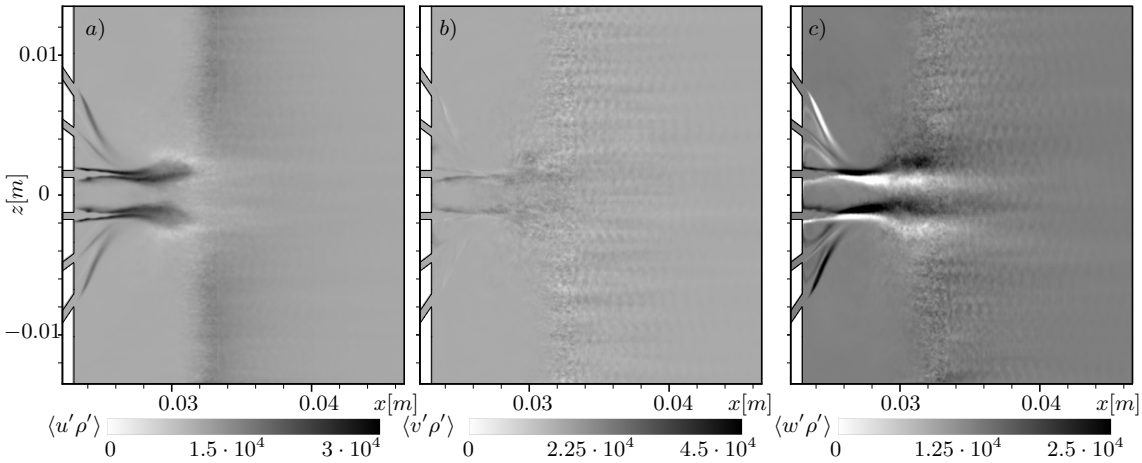

Figure 6.13: Turbulence transport in all three directions on a $y = 0m$ slice.

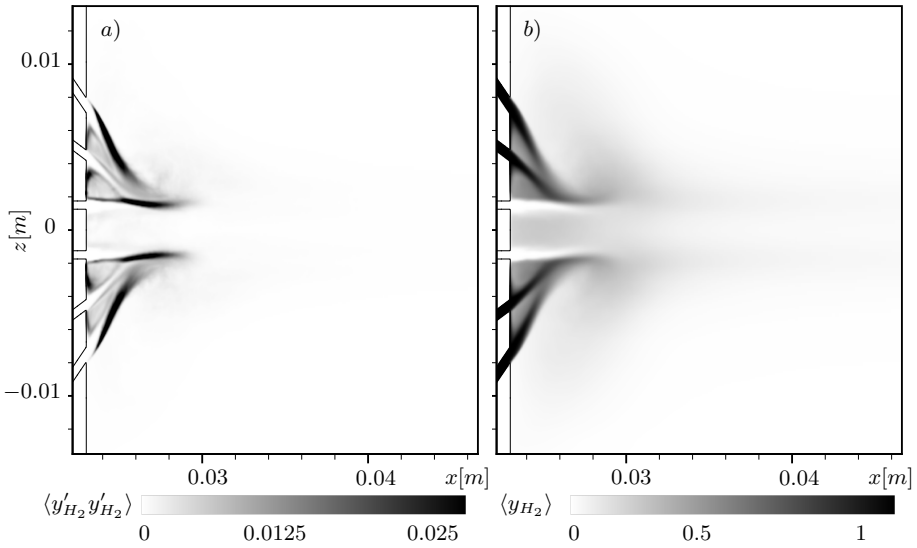

Figure 6.14: Variance of the hydrogen massfraction and hydrogen mean massfraction on a $y = 0m$ slice.

the hydrogen jets.

The variance of the hydrogen massfraction, Fig. 6.14 a), shows maxima at the air jet boundaries where the hydrogen impinges, as well as on the outer boundary of the hydrogen jets. This is consistent with the result of the velocity fluctuations. Furthermore, the figure shows that the six injection holes create two mixing zones, one on each side, with the most mixing on the outer boundary of the respective air jet. The massfraction vanishes quickly because of the hydrogen's low density, and so there is no visible rise in massfraction variance in the region of high turbulence following the mixing. The massfraction is plotted in Fig. 6.14 b) where the four jets are clearly visible and a region where the massfraction spreads in z-direction at $x \approx 0.03m$. This is caused by the horizontal recirculation. Following the region at $x \approx 0.032m$ the massfraction is barely visible as it mixes with the air. A similar observation is made in Fig. 6.14. The plot shows the mean

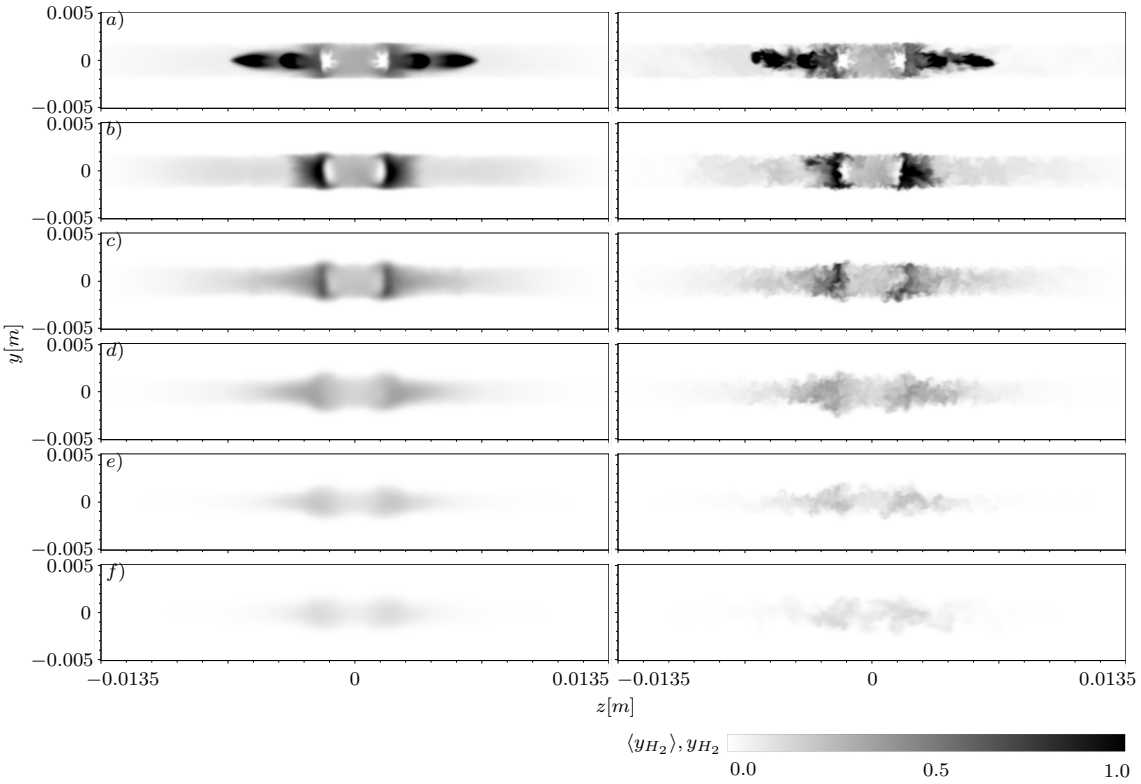

Figure 6.15: Time averaged and instantaneous plots of the hydrogen massfraction on slices with constant x-coordinate. The locations of the individual slices are marked in Fig. 6.8.

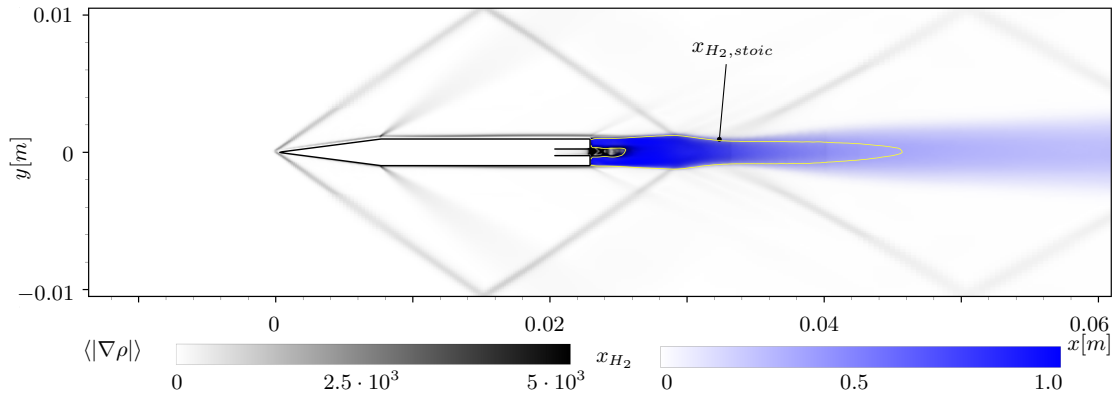

Figure 6.16: Time averaged density gradient magnitude (grey) and hydrogen volume fraction (blue) on a $z = -0.0015m$ slice. Yellow line displays the stoichiometric line for hydrogen - air combustion.

(left) and instantaneous (right) hydrogen massfraction on $x = const.$ slices at the locations a) through f) as indicated in Fig. 6.8. The main regions of high massfraction are located left and right of the air jets, which are clearly visible as white regions in the slices close to the injector. Further downstream the distribution becomes more homogeneous as the gases mix and the value of the hydrogen massfraction rapidly drops.

For hydrogen mixing the volume fraction gives additional information on the distribu-

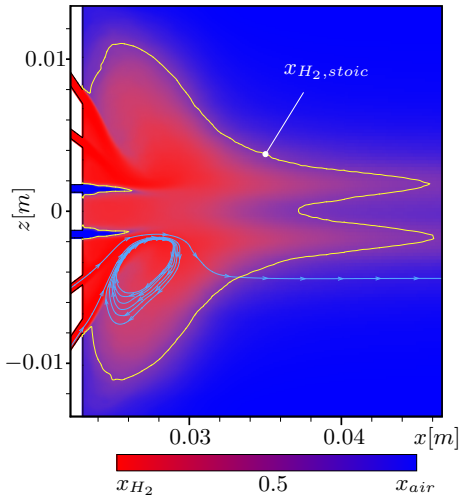

Figure 6.17: Pure hydrogen volume fraction (red) to pure air volume fraction (blue) on a $y = 0m$ slice. Yellow line displays the stoichiometric line for hydrogen - air combustion.

tion and does not decay as quickly as the massfraction. This can be seen in Figs. 6.16 and 6.17, where the mean volume fraction is shown. The first figure shows the density gradient magnitude in white to black contours and the volume fraction in white to blue at a position $z = -0.0015m$. The volume fraction is visible over the entire length of the domain following the injection and is spreading in spanwise direction further downstream. The region where the shocks from the channel walls hit the recirculation shows a thickening of the mixing region due to the imposed upstream pressure gradient on the subsonic recirculation. Figure 6.17 displays the volume fraction distribution ranging from pure hydrogen on the one side of the color scale to pure air on the other side of the scale. Streamlines show the horizontal recirculation, which enhances the mixing and is created by the hydrogen jets.

Another advantage of the volume fraction is the straight forward detection of the stoichiometric mixture. This is advantageous since one of the goals of this study is to evaluate the mixture with respect to possible combustion. A generic reaction equation for hydrocarbon fuel combustion with air is

$$C_xH_y + a\left(O_2 + \frac{79}{21}N_2\right) \longrightarrow xCO_2 + \frac{y}{2}H_2O + \frac{79}{21}aN_2 \tag{6.17}$$

with $a = x + y/4$. For hydrogen combustion x will become 0 as there is no carbon and y is set to 2 for the bi-atomic molecule H_2. These filled into Eq. 6.17 leads to

$$2H_2 + O_2 + \frac{79}{21}N_2 \longrightarrow 2H_2O + \frac{79}{21}N_2 \tag{6.18}$$

from which the stoichiometric volume fraction can be calculated as:

$$x_{H_2,stoich} = \frac{2}{2+1+\frac{79}{21}} = 0.295775. \tag{6.19}$$

This line has been added to Figs. 6.16 and 6.17 to give a rough estimate of where the main reaction zone will be. The large volume of the stoichiometric iso-surface makes this a good solution for combustion. In a first coarse approximation the location of the flame would be at the stoichiometric line. Additionally, the subsonic region will have a higher temperature than the surrounding supersonic flow and the impinging shock improves this even further. While the temperature is still to low for autoignition, this is of no concern since this configuration was built to be ignited by a laser.

7 Summary

In order to perform LES of supersonic mixing processes the existing simulation code INCA was extended with capabilities for multispecies mixing. The new functionality enhances the code to calculate correct mixing properties for ideal gases based on Chapman Enskog relations. For validation of the added routines, a two-dimensional heavy gas bubble with a shockwave passing through it was simulated. Comparison with available data showed good agreement and proved the correct implementation of the thermodynamic laws.

In addition to enhancing the LES code a separate novel tool has been created for mesh generation. It greatly enhances the possibilities while manually generating an modifying simulation grids by employing a graphical user interface. This allowed for the creation of the grids necessary for this thesis, which would not have been possible using the automatic routines built in INCA.

As a starting point for mixing simulations, a validation of physical and numerical models for large-eddy simulations of supersonic injection was conducted. The main flow features, e.g., strong shockwaves and turbulence of different length and time scales could be reproduced. Our results have excellent agreement with numerical data from literature. Comparison to experimental data showed some deviations, which where further investigated with a variation of selected parameters. The penetration depth of the experiment could not be reproduced for the given jet to crossflow momentum ratio. Other features of the flow could be substantially influenced by some parameters. The jet inflow velocity profile turned out to have the strongest effect on the overall flow field. Less pronounced effects resulting from a Reynolds number parameter study are mainly seen inside the jet for the maximum reached Mach number in front of the Mach disk. The turbulent mixing intensity as well as the wall normal and horizontal extend of the mixing zone were mainly influenced through changing the velocity profile of the jet entering the crossflow.

Subsequently, a part of a recent experiment featuring a scramjet strut injector was simulated. This has been conducted in two stages. In the first simulation the main injection mechanism was investigated and in a second simulation the pilot injection. Both were simulated with only their respective injection method to isolate their effect.

For the main injection experiment and simulation, carbon dioxide served as a substitute for the fuel. The simulation showed small deviations from the experiment. These were attributed to uncertainties in the boundary layer at the chamber wall, as there was no pos-

sibility to take measurements in the boundary layer. Switching off the injection, however, produced a similar trend in the results for both, experiment and simulation. Furthermore it was concluded that the presence of more than one injection is beneficial to the overall mixing as the shocks produced by neighboring injections amplify the turbulent mixing in the wake of the jets.

For the pilot injection, the fuel was not substituted, instead hydrogen was used in the experiment and simulation. INCA was able to accurately model the complex geometry with the immersed boundary method. Due to the prescribed pressures of the injections, the gases are injected at supersonic speed. The high injection speed causes very fast and efficient mixing in the current configuration for the pilot injection. However the mixing zone is divided into two disconnected regions caused by the angles of the injection bores. The shocks have a small influence on the pilot injection as only two shocks pass through the mixing zone at a single location. Only slight turbulence intensity increase and thickening of the mixing zone was observed. The line of stoichiometric mixture gave an estimate of where the main reaction zone of the pilot flame is located.

The mixing studies showed very low penetration depth of injections perpendicular to the main flow. This reassured the necessity of strut injectors for large combustion chambers. The simulations of this thesis furthermore provided detailed information on the mixing process of recent experiments. A parameter study of flow parameters was presented which discussed the effects of varying fluid properties. It was shown how a configuration of several injections increases turbulent mixing and the spanwise mixing area. Furthermore the simulations provided details of the pilot injection flow which were not possible to measure in the experiment. By that the simulations of this thesis enhanced the understanding of the flows which where observed in the experiments.

Bibliography

[1] NRLMSISE-00 atmosphere model. http://ccmc.gsfc.nasa.gov/modelweb/models/, Nov 2014.

[2] X. Chai and K. Mahesh. Simulations of high speed turbulent jets in crossflows. *AIAA 2011-650*, 2011.

[3] C. E. Jr. Cockrell, A. H. Auslender, R. W. Guy, C. R. McClinton, and S. S. Welch. Technology roadmap for dual-mode scramjet propulsion to support space-access vision vehicle development. *AIAA*, 2002-5188, 2002.

[4] A. Cook. Enthalpy diffusion in multicomponent flows. *Physics of Fluids*, 21:055109, 2009.

[5] P. Dupont, C. Haddad, and J. F. Debiève. Space and time organization in a shock-induced separated boundary layer. *Journal of Fluid Mechanics*, 559:255–277, 2006.

[6] D. E. Everett, M. A. Woodmansee, J. C. Dutton, and M. J. Morris. Wall pressure measurements for a sonic jet injected transversely into a supersonic crossflow. *Journal of Propulsion and Power*, 14:861–868, 1998.

[7] F. H. Falempin. Scramjet development in France. *Progress in Astronautics and Aeronautics, Scramjet Propulsion (AIAA)*, 189:47–117, 2000.

[8] S. Fuhrmann, A. Hupfer, and H.-P. Kau. Investigations on multi-stage supersonic combustion in a model combustor. *AIAA 2011-2332*, 2011.

[9] S. Gottlieb and C.-W. Shu. Total variation diminishing Runge-Kutta schemes. *Mathematics of Computation*, Volume 67, Number 221:73–85, 1998.

[10] Khronos Group. Opengl - the industry standard for high performance graphics. https://www.opengl.org/, Oct 2014.

[11] W. H. Heiser, D. T. Pratt, D. H. Daley, and U. B. Mehta. *Hypersonic Airbreathing Propulsion*. AIAA education series, 1994.

[12] S. Hickel, N.A. Adams, and J.A. Domaradzki. An adaptive local deconvolution method for implicit LES. *Journal of Computational Physics*, Volume 213, Issue 1:413–436, 2006.

[13] S. Hickel, C.P. Egerer, and J. Larsson. Subgrid-scale modeling for implicit large eddy simulation of compressible flows and shock-turbulence interaction. *Physics of Fluids*, 26:106101, 2014.

[14] S. Kawai and S. K. Lele. Large-eddy simulation of jet mixing in supersonic cross-flows. *AIAA Journal*, Vol. 48, No. 9:2063–2083, 2010.

[15] S. H. Kim, P. Donde, V. Raman, K. Lin, and C. Carter. Large eddy simulation based studies of reacting and non-reacting transverse jets in supersonic crossflow. *50th AIAA Aerospace Sciences Meeting*, pages 2012–0482, 2012.

[16] M. Klein, A. Sadiki, and J. Janicka. A digital filter based generation of inflow data for spatially developing direct numerical or large eddy simulations. *Journal of Computational Physics*, Volume 186, Issue 2:652–665, 2003.

[17] C. Lafleur. Spacecraft encyclopedia. http://claudelafleur.qc.ca/Spacecrafts-index.html, Oct 2014.

[18] A. Leonard. Energy cascade in large eddy simulations of turbulent fluid flows. *Advanced Geophysics*, 18A:237–248, 1974.

[19] Hersch M., L. Povinelli, and F. Povinelli. A schlieren technique for measuring jet penetration into a supersonic stream. *Journal of Spacecraft and Rockets*, 7:755–756, 1970.

[20] K. Makowka, M. Gurtner, and D. Paukner. Numerical and experimental investigation of a central strut injector with perpendicular injection for scramjet applications. *European conference for aeronautics and space sciences*, 2013.

[21] E. Meshkov. Instability of the interface of two gases accelerated by a shock wave. *Izvestiya Akademii Nauk SSSR, Mekhanika Zhidkosti i Gaza*, 4:151, 1969.

[22] M. Meyer, A. Devesa, S. Hickel, X.Y. Hu, and N.A. Adams. A conservative immersed interface method for large-eddy simulation of incompressible flows. *J. Comp. Phys.*, 229:6300–6317, 2010.

[23] M. Meyer, S. Hickel, and N.A. Adams. Assessment of implicit large-eddy simulation with a conservative immersed interface method for turbulent cylinder flow. *International Journal of Heat and Fluid Flow*, 31:368–377, 2010.

[24] P. D. Neufeld, A. R. Janzen, and R. A. Aziz. Empirical equations to calculate 16 of the transport collision integrals $\omega^{(l,s)}$ for the lennard-jones (12-6) potetntial. *Journal of Chemical Physics*, 57(3):1100, 1972.

[25] F. Örley, V. Pasquariello, S. Hickel, and N.A. Adams. Cut-element based immersed boundary method for moving geometries in compressible liquid flows with cavitation. *Journal of Computational Physics*, 283:1–22, 2015.

[26] C. Pantano and S. Sarkar. A study of compressibility effects in the high-speed turbulent shear layer using direct simulation. *Journal of Fluid Mechanics*, 451:329–371, 2002.

[27] O. Petrache, S. Hickel, and N. A. Adams. Large eddy simulations of turbulent enhancement due to forced shock motion in shock-boundary layer interaction. *AIAA 2011-2216*, 2011.

[28] S. Pirozzoli and M. Bernardini. Turbulence in supersonic boundary layers at moderate Reynolds number. *Journal of Fluid Mechanics*, 688:120–168, 2011.

[29] B. Poling. *The Properties of Gases and Liquids, 5th Edition*. McGraw-Hill, 2001.

[30] R. Portz and C. Segal. Mixing in high-speed flows with thick boundary layers. *40TH AIAA/ASME/SAE/ASEE joint propulsion conference and exhibit, AIAA 2004–3655*, 2004.

[31] Qt Project. Qt project. https://qt-project.org/, Oct 2014.

[32] J. D. Ramshaw. Self-consistent effective binary diffusion in multicomponent gas mixtures. *Journal of Non-Equilibrium Thermodynamics*, Volume 15, Issue 3:295–300, 1990.

[33] Z. A. Rana, D. Drikakis, and B. J. Thornber. Investigation of sonic jet mixing in a stream of supersonic cross-flow usning large eddy simulations. *27th International Congress of the Aeronautical Sciences*, 2010.

[34] R. D. Richtmyer. Taylor instability in shock acceleration of compressible fluids. *Communications on Pure and Applied Mathematics*, 8:297, 1960.

[35] Aerojet Rocketdyne. RS-25 Engine. https://www.rocket.com/rs-25-engine, Oct 2014.

[36] J. G. Santiago and J. C. Dutton. Velocity measurements of a jet injected into a supersonic crossflow. *Journal of Propulsion and Power*, 13:264–273, 1997.

[37] C. Segal. *The scramjet engine, processes and characteristics*. Cambridge University Press, 2009.

[38] S. K. Shankar, S. Kawai, and S. K. Lele. Two-dimensional viscous flow simulation of a shock accelerated heavy gas cylinder. *Physics of Fluids*, 23:024102, 2011.

[39] Open Source. Git. https://git-scm.com/, Oct 2014.

[40] J. Steelant. Lapcat: High-speed propulsion technology. *ESA-ESTEC, Midterm Report*, 2012.

[41] C. Tomkins, S. Kumar, G. Orlicz, and K. Prestridge. An experimental investigation of mixing mechanisms in shock-accelerated flow. *Journal of Fluid Mechanics*, pages 131–150, 2008.

[42] V. K. Tritschler, A. Avdonin, and N. A. Adams S. Hickel, X. Y. Hu. Quantification of initial-data uncertainty on a shock-accelerated gas cylinder. *Physics of Fluids*, 26:026101, 2014.

[43] W. M. VanLerberghe, J.G. Santiago, J. C. Dutton, and R. P. Lucht. Mixing of a sonic transverse jet injected into a supersonic flow. *AIAA Journal*, 38:470–479, 2000.

[44] U. Walter. *Astronautics*. Wiley-VCH, 2008.

[45] J. Watanabe, T. Kouchi, K. Takita, and G. Masuya. Large-eddy simulation of jet in supersonic crossflow with different injectant species. *AIAA Journal*, 50, No. 12:2765–2778, 2012.

[46] D. M. Van Wie, S. M. D'Alessio, and M. E. White. Hypersonic airbreathing propulsion. *Johns Hopkins APL Technical Digest*, 2005.

[47] C. R. Wilke. A viscosity equation for gas mixtures. *Journal of Chemical Physics*, 18(4):517, 1950.

[48] F. A. Williams. *Combustion Theory, 2nd Edition*. Perseus Books, 1985.

[49] J. Yang, T. Kubota, and E. E. Zukoski. Applications of shock-induced mixing to supersonic combustion. *AIAA Journal*, 31, No. 5, 1993.